



저작자표시-비영리-변경금지 2.0 대한민국

이용자는 아래의 조건을 따르는 경우에 한하여 자유롭게

- 이 저작물을 복제, 배포, 전송, 전시, 공연 및 방송할 수 있습니다.

다음과 같은 조건을 따라야 합니다:



저작자표시. 귀하는 원저작자를 표시하여야 합니다.



비영리. 귀하는 이 저작물을 영리 목적으로 이용할 수 없습니다.



변경금지. 귀하는 이 저작물을 개작, 변형 또는 가공할 수 없습니다.

- 귀하는, 이 저작물의 재이용이나 배포의 경우, 이 저작물에 적용된 이용허락조건을 명확하게 나타내어야 합니다.
- 저작권자로부터 별도의 허가를 받으면 이러한 조건들은 적용되지 않습니다.

저작권법에 따른 이용자의 권리는 위의 내용에 의하여 영향을 받지 않습니다.

이것은 [이용허락규약\(Legal Code\)](#)을 이해하기 쉽게 요약한 것입니다.

[Disclaimer](#)

공학박사학위논문

**A Study on the Microstructure and
Mechanical Behavior of High-Mn
Low-density Steels**

고망간 경량철강 소재의 미세조직과 기계적 거동에
대한 연구

2017년 2월

서울대학교 대학원
재료공학부
이근호

**A Study on the Microstructure and
Mechanical Behavior of High-Mn
Low-density Steels**

고망간 경량철강 소재의 미세조직과 기계적 거동에
대한 연구


지도교수 한 홍 남

이 논문을 공학박사학위논문으로 제출함
2017년 1월

서울대학교 대학원
재료공학부
이 근 호

이근호의 박사학위논문을 인준함
2017년 1월

위	원	장	_____	오	규	환	(인)
부	위	원	_____	한	홍	남	(인)
위		원	_____	박	은	수	(인)
위		원	_____	박	성	준	(인)
위		원	_____	Phaniraj	Madakashira		(인)



Phaniraj Madakashira (인)

ABSTRACT

In recent years, decreasing greenhouse gas emissions and improving fuel efficiency have been growing issues in the automotive and defense sectors. To achieve this goal, the development of advanced high-strength steels (AHSSs), such as dual-phase (DP) and transformation-induced plasticity (TRIP) steels has been long pursued for automotive applications. However, as the strength of steel increases, it gets more difficult to reduce the thickness due to the deterioration of structural stiffness, causing poor crashworthiness. In that sense, alternative concept of designing AHSS has been proposed mainly by lowering the density of steel while maintaining its high specific strength. Based on this concept, “low-density steels” have been developed containing light substitutional elements such as aluminum and/or silicon, which provide a density reduction effect by means of substitution and lattice expansion.

Low-density steels can be categorized into ferrite-based and austenite-based (including multiphase-based) alloys, depending on their constituent phases. Among them, the austenite-based low-density steels show superior mechanical properties and weight reduction rates. After these steels are aged at adequate temperature and time periods, many kinds of micro/nano-scale precipitates or intermetallic compounds are formed, such as κ -carbide, ordered

bcc phases, and β -Mn. These precipitates have a profound effect on the mechanical properties of the low-density steels. However, there is still a paucity of characterization research on the β -Mn phase in terms of the formation behavior, microstructural evolution, and its effects on mechanical and fracture properties of austenite-based high-Mn low-density steels. Therefore, this research investigates the microstructure and mechanical behavior of high-Mn low-density steels after processing treatments, by using complementary microstructural and mechanical characterization.

Firstly, the microstructure and the intrinsic mechanical behavior of an austenite-based low-density steel containing 11.4 wt.% Al under aging heat treatment were investigated with respect to β -Mn precipitation. Lattice expansion of austenite and κ -carbide after β -Mn precipitation was observed by X-ray diffractometry (XRD) peak shift and electron probe micro-analyzer (EPMA). The Vickers hardness increased dramatically after an aging time of 1,000 minutes. The singular aging behavior also proceeded from precipitation of the β -Mn phase. The intrinsic mechanical property of austenite phase, which was obtained by nanoindentation, was correlated with the increase and inhomogeneous distribution of carbon in the austenite matrix.

Secondly, the β -Mn formation behavior of high-Mn low-density steels was investigated in terms of the morphological characteristics and alloying element distribution after aging treatments. A dramatic difference in the formation

kinetics and morphology of β -Mn was observed depending on the addition of Al, which may increase the driving force for β -Mn formation. In addition, the effects of the aging process on the fracture behavior were examined in uniaxial tensile tests combined with microstructural observations. A severe loss of ductility resulted from the β -Mn formation and ordering of ferrite into the DO_3 phase, which was transformed before the β -Mn formation process.

Thirdly, the aging behavior and orientation relationships among constitutional phases and precipitates in Fe–31.4Mn–11.4Al–0.89C low-density steel were studied. The misorientation-angle distribution, Rodrigues–Frank vector space, and orientation relationship stereogram (OR stereogram) are used to elucidate the orientation relationships across γ -matrix/ β -Mn and β -Mn/ α -precipitate interphase boundaries. The orientation relationships obtained from the OR stereograms were clarified by checking the deviation angle distributions of interface segments from the ideal orientation relationships, as well as the TEM diffraction patterns at the interface boundaries. In addition, from both orientation relationships for γ -matrix/ β -Mn and β -Mn/ α -precipitate interfaces, the interface character between γ -matrix and α -precipitate is examined and compared to conventional fcc/bcc orientation relationships.

Lastly, the deformation behavior of duplex low-density steel was analyzed by correlation between macro-scale uniaxial tension and nano-scale indentation. A dramatic difference in the tensile behavior was observed between two

specimens obtained under specific heat-treatment conditions, despite the same chemical composition and similar microstructures. In order to understand this difference, the intrinsic mechanical properties of each phase were analyzed based on nano-indentation results considering Hall-Petch relationship. In addition, the mechanical stability of retained austenite was investigated by *in-situ* electron backscattered diffraction.

From this study, the β -Mn phase in austenite-based high-Mn low-density steels was described well, in terms of the formation behavior, microstructural evolution, orientation relationships, and its effects on mechanical and fracture properties. In addition, the dramatic differences of the macroscopic tensile behavior regarding the yield strength, yield point phenomenon, and strain hardening in the two duplex low-density steels was successfully explained.

Keywords: Metals and alloys, Low-density steel, Aging, Beta-manganese, Vickers hardness, XRD, EPMA, EBSD, TEM, Morphological characteristics, Uniaxial tensile test, Fracture, Orientation relationship, Orientation relationship stereogram (OR stereogram), Nano-indentation, Hall-Petch relationship, Austenite

Student number: 2011-20655

Contents

Abstract	I
Table of Contents	V
List of Tables	X
List of Figures	XI

Chapter 1

Introduction

1.1 Low-density steels.....	1
1.2 Classification of the low-density steels	4
1.3 Motivations of the thesis	6
1.4 References	9

Chapter 2

Effect of aging treatment on microstructure and intrinsic

mechanical behavior of Fe–31.4Mn–11.4Al–0.89C low-density steel

2.1 Introduction.....	11
2.2 Experimental procedure	14
2.3 Microstructural analysis.....	17
2.4 Intrinsic mechanical properties: Nanoindentation analysis ...	29
2.5 Conclusion: Effect of aging treatment on microstructure and intrinsic mechanical behavior	35
2.6 References	36

Chapter 3

β -Mn formation and aging effect on the fracture behavior of high-Mn low-density steels

3.1 Introduction.....	39
3.2 Experimental procedure	41

3.3 Influence of alloying elements on the formation behavior of the κ-carbide and β-Mn	44
3.4 Tensile and fracture behavior	50
3.5 Conclusion: β-Mn formation and aging effect on the fracture behavior	57
3.6 References	59

Chapter 4

Investigation of the aging behavior and orientation relationships in Fe–31.4Mn–11.4Al–0.89C low-density steel

4.1 Introduction.....	61
4.2 Materials and methods	65
4.2.1 Microstructure observation and interface characterization	65
4.2.2 Calculation of the deviation angle from the ideal orientation	

relationship	68
4.3 Microstructural evolution and aging behavior.....	71
4.4 Orientation relationship between γ-matrix and β-Mn	81
4.5 Orientation relationship between β-Mn and α-precipitate... 	90
4.6 Interface character distribution of γ-matrix/α-precipitate phase boundaries	98
4.7 Conclusion: Investigation of the aging behavior and orientation relationships	105
4.8 References	107

Chapter 5

Dual-scale correlation of mechanical behavior in duplex low-density steel

5.1 Introduction.....	110
5.2 Experimental procedure	112

5.3 Macroscopic tensile behavior and initial microstructure	114
5.4 Correlation between macro-scale uniaxial tension and nano-scale indentation	119
5.5 Deformation-induced martensitic transformation	126
5.6 Conclusion: Dual-scale correlation of mechanical behavior ...	129
5.7 References	130

Chapter 6

Total conclusions	133
--------------------------------	------------

LIST OF TABLES

Table 1.1 The representative low-density steels with nominal chemical composition and mechanical properties.

Table 2.1 Grain size and volume fraction of each phase in the specimens obtained from EBSD.

Table 2.2 Nano-hardness calculated from the load–displacement curves (numbers in parenthesis are the standard deviation).

Table 3.1 Chemical composition of the investigated alloys. (wt.%)

Table 4.1 The principal axis length and aspect ratios of the 94 β -Mn grains from 3D RVE.

Table 5.1 Grain size of each phase and austenite fraction of the alloys obtained from EBSD.

LIST OF FIGURES

Figure 1.1 Density as function of the aluminium concentration under Fe-Al-Mn-C alloy system with varying manganese contents (14 to 28 wt.%).

Figure 2.1 EBSD phase map of the: (a) ST; (b) A300; (c) A1000, and; (d) A10000 specimens (red : FCC; yellow : BCC; green : β -Mn). The horizontal direction is a normal direction of the specimen. The inserted EBSD phase map with magnification in (d) represents microscopic bcc ordered phases (B2 or $D0_3$) precipitated in the A10000 specimen.

Figure 2.2 TEM micrographs and diffraction patterns of the A1000 specimen. (a) Bright-field image including β -Mn grains. (b) Selected area diffraction pattern showing [001] zone of the β -Mn phase. (c) Bright-field image of matrix region. (d) Selected area diffraction pattern showing [011] zone of the austenite and κ -carbide.

Figure 2.3 X-ray diffraction diagrams of the overall specimens. Red arrows

indicate the peak shift of austenite and κ -carbide.

Figure 2.4 (a) Sequential changes in magnified γ (220) peak in Fig. 2.3 on aging heat treatment. Red arrows indicate the peak shift of austenite and κ -carbide.

(b) Lattice parameters of austenite and κ -carbide of the overall specimens calculated from X-ray diffraction diagrams as a function of aging time.

Figure 2.5 (a) EBSD phase map of the A1000 specimen (red : FCC; yellow : BCC; green : β -Mn) before EPMA analysis. EPMA elemental mapping in the same area where the EBSD scan occurred: (b) carbon; (c) aluminum; (d) manganese, and; (e) iron map. (f) Carbon content profile of the sky-blue line in (a).

Figure 2.6 (a) EBSD phase map of the A1000 specimen (red : FCC; yellow : BCC; green : β -Mn) after indentation. SPM image of the indents in the same area marked with triangles shown in (a): (b) ferrite grain; (c) β -Mn grain, and;

(d) austenite grain. Nanoindentation load-displacement curves of all constituent phases in the (e) ST and (f) A1000 specimens.

Figure 2.7 Vickers hardness of the overall specimens and nano-hardness of each constituent phase in the ST and A1000 specimens obtained from nanoindentation as a function of aging time.

Figure 3.1 Vickers hardness of the 9Al, 9Al-1Si, and 11Al alloys as a function of the aging time at 550 °C. TEM micrograph and selected-area diffraction pattern showing the [001] zone of the κ -carbide in the austenite matrix of the 9Al specimen aged for 1000 min are inserted.

Figure 3.2 Figure 3.2 Optical micrographs of (a) 9Al ST, (b) 9Al-1Si ST, (c) 11Al ST, (d) 9Al aged for 10000 min, (e) 9Al-1Si aged for 10000 min, and (f) 11Al aged for 1000 min. γ and α represent austenite and ferrite, respectively.

Figure 3.3 (a) SEM micrograph and (b) EBSD phase map (red : FCC; yellow : BCC; green : β -Mn) of the 9Al-1Si aged for 10000 min. (c) EDS elemental profiles of the sky-blue line in (a).

Figure 3.4 (a) Yield strength and total elongation of the 9Al, 9Al-1Si, and 11Al alloys as a function of aging time at 550 °C. (b) Engineering stress-strain curves of the 11Al specimens.

Figure 3.5 SEM fractographs after the tensile test of the 11Al specimens aged at 550 °C for (a) 0 min (ST), (b) 100 min, (c) 300 min, and (d) 1000 min.

Figure 3.6 SEM micrographs and EBSD phase maps (red : FCC; yellow : BCC; green : β -Mn) near the fracture surface after the tensile test of the 11Al specimens aged at 550 °C for (a) 0 min (ST), (b,c) 100 min, and (d,e) 300 min. γ and α represent the austenite and ferrite, respectively. (f) TEM micrograph and selected-area diffraction pattern showing the [011] zone of the $D0_3$ phase in the ferrite of the specimen aged for 300 min.

Figure 4.1 The equilibrium phase fractions as a function of temperature of Fe–30Mn–12Al–0.9C alloy, calculated with CALPHAD method.

Figure 4.2 EBSD phase maps: (a) as solution treated; after aging at 550 °C for (b) 1,000 mins.; (c, d) 10,000 mins., and; (e) 100,000 mins. (red : FCC; yellow : BCC; green : β -Mn). The horizontal direction is a rolling direction of the specimen. (d, e) are the locally magnified phase maps representing the precipitation of microscopic ordered bcc phases inside the β -Mn grains. (f) Vickers hardness of as a function of aging time.

Figure 4.3 3D-reconstructed EBSD microstructure after aging at 550 °C for 1,000 mins: (a) Phase map (red : FCC; yellow : BCC; green : β -Mn), (b) Austenite orientation (TD) map, (c) β -Mn orientation (TD) map.

Figure 4.4 (a) Distribution of β -Mn plate lengths from 3D EBSD RVE in Fig. 4.3, assuming the β -Mn morphology as an ellipsoid. Plots of (b) width against length, and (c) thickness against length of β -Mn plates.

Figure 4.5 TEM micrographs and diffraction patterns after aging at 550 °C for 30,000 mins. (a) Bright-field image and (b) selected area diffraction pattern showing [011] zone of the γ -austenite and κ -carbide. (c) Bright-field image and (d) selected area diffraction pattern showing [011] zone of the α -precipitate including partial $D0_3$ order.

Figure 4.6 Microstructure after aging at 550 °C for 1,000 mins.: (a) EBSD phase map (red : FCC; yellow : BCC; green : β -Mn), (b) Orientation (TD) map, (c) IQ map highlighting misorientation angles for γ -matrix/ β -Mn interphase boundaries in the range $17^\circ < \text{red} < 21^\circ$, which corresponds to the dominant orientation relationship (see next figure). The horizontal direction is a normal direction of the specimen.

Figure 4.7 (a) Misorientation-angle distribution and (b) Rodrigues–Frank vector space $\mathbf{R}(R_1, R_2, R_3)$ for γ -matrix/ β -Mn interphase boundaries from EBSD measurements in Fig. 4.6. The black curve in (a) indicates the MacKenzie

distribution.

Figure 4.8 Overlaid pole figures showing the orientation relationship for (a) region 1, (b) region 2, (c) region 3, (d) region 4, and (e) region 5 in Fig. 4.6(a) (γ -matrix poles in red, β -Mn poles in blue); the common interface normal is identified as well as the common direction located in the zone of the normal (dashed great circle) i.e. the trace of the interface plane. (f) Distributions of the deviation angle of γ -matrix/ β -Mn phase boundary segments from ideal γ -matrix/ β -Mn relationship. The black line in (f) indicates the distribution of deviation angles based on randomly oriented pairs of points in γ -matrix and β -Mn.

Figure 4.9 TEM micrographs and diffraction patterns at the γ -matrix/ β -Mn interphase boundaries after aging at 550 °C for 30,000 mins. (a) Bright-field image and (b) selected area diffraction pattern showing [011] zone of the γ -austenite and κ -carbide and [012] zone of the β -Mn phase, showing overlapped

111 γ -matrix and 221 β -Mn poles.

Figure 4.10 Crystallographic atom arrays at the interface between {111} plane of the γ -matrix and {221} plane of the β -Mn phase.

Figure 4.11 Microstructure after aging at 550 °C for 30,000 mins.: (a) EBSD phase map (red : FCC; yellow : BCC; green : β -Mn), (b) Orientation (TD) map, (c) IQ map highlighting misorientation angles for β -Mn/ α -precipitate interphase boundaries in the range $24^\circ < \text{red} < 28^\circ$, which corresponds to the dominant orientation relationship (see next figure). The horizontal direction is a normal direction of the specimen.

Figure 4.12 (a) Misorientation-angle distribution and (b) Rodrigues–Frank vector space $\mathbf{R}(R_1, R_2, R_3)$ for β -Mn/ α -precipitate interphase boundaries from EBSD measurements in Fig. 4.11. The black curve in (a) indicates the MacKenzie distribution.

Figure 4.13 Overlaid pole figures showing the orientation relationship for (a)

region 1, (b) region 2, (c) region 3, (d) region 4, and (e) region 5 in Fig. 4.11(a) β -Mn poles in red, α -precipitate poles in blue); the common interface normal is identified as well as the common direction located in the zone of the normal (dashed great circle) i.e. the trace of the interface plane. (f) Distributions of the deviation angle of β -Mn/ α -precipitate phase boundary segments from ideal β -Mn/ α -precipitate relationship. The black line in (f) indicates the distribution of deviation angles based on randomly oriented pairs of points in β -Mn and α -precipitate.

Figure 4.14 TEM micrographs and diffraction patterns at the β -Mn/ α -precipitate interphase boundaries after aging at 550 °C for 30,000 mins. (a) Bright-field image and (b) selected area diffraction pattern showing [012] zone of the β -Mn phase and [001] zone of the α -precipitate phase including partial $D0_3$ order, showing overlapped 021 β -Mn and 221 $\alpha+D0_3$ poles.

Figure 4.15 Schematic diagram of all the variants of γ -matrix/ α -precipitate

relationship through β -Mn transformation in the investigated alloy around one Bain variant on a $\{100\}_{\text{BCC}}$ pole figure, indicated by red stars. The KS, NW and Pitsch relationships are shown together with the different symbols and colors.

Figure 4.16 (a) Misorientation-angle distribution and (b) Rodrigues–Frank vector space $\mathbf{R}(R_1, R_2, R_3)$ for γ -matrix/ α -precipitate interphase boundaries from EBSD measurements in Fig. 4.11. The black curve in (a) indicates the MacKenzie distribution.

Figure 4.17 Distributions of deviation angle of γ -matrix/ α -precipitate phase boundary segments from ideal (a) Bain, (b) KS, (c) NW, and (d) Pitsch relationships. The black curves indicate the distribution of deviation angles based on randomly oriented pairs of points in γ -matrix and α -precipitate.

Figure 5.1 (a) Engineering stress-strain curves and (b) true stress-strain curves with corresponding strain hardening rate as a function of true strain for T800 and T900 specimens.

Figure 5.2 EBSD phase map of cold-rolled and annealed specimens: (a) T800; (b) T900 (red : FCC; yellow : BCC).

Figure 5.3 Nano-indentation load-displacement curves of T800 (a) δ -ferrite, (c) α -ferrite, (e) austenite and T900 (b) δ -ferrite, (d) α -ferrite, (f) austenite. Blue dashed lines indicate the theoretical Hertzian elastic solution.

Figure 5.4 Maximum shear stress underneath indenter for each phase: (a) T800; (b) T900 (■ the intrinsic value; ▨ the value considered grain size effect).

Figure 5.5 EBSD phase maps of T800 at true strains of (a) 0%, (b) 5.5%, (c) 12.4% and T900 at true strains of (d) 0%, (e) 3.9% and (f) 10.5%. (red : FCC; yellow : BCC; — misorientation angle $> 5^\circ$; — misorientation angle $2\sim 5^\circ$)
Blue arrows indicate martensite transformed from retained austenite.

Chapter 1

Introduction

1.1 Low-density steels

In recent years, decreasing greenhouse gas emissions and improving fuel efficiency have been growing issues in the automotive and defense sectors. To achieve this goal, the development of advanced high-strength steels (AHSSs), such as dual-phase (DP) and transformation-induced plasticity (TRIP) steels has been long pursued for automotive applications [1-3]. However, as the strength of steel increases, it gets more difficult to reduce the thickness due to the deterioration of structural stiffness, causing poor crashworthiness [4, 5]. In that sense, alternative concept of designing AHSS has been proposed mainly by lowering the density of steel while maintaining its high specific strength. Based on this concept, “low-density steels” have been developed containing light substitutional elements such as aluminum and/or silicon, which provide a density reduction effect by means of substitution and lattice expansion. Quantitative density reductions according to aluminum concentration under Fe-Al-Mn-C alloy system are shown in Fig. 1.1 [6].

Indeed, several studies of alloying a considerable amount of aluminium in the Fe-Mn-C-base alloy were conducted for various applications, such as

cryogenic alloys, oxidation resistance alloys at high temperature, and corrosion resistance alloys [7-11]. Especially in the corrosion resistance application, many researchers studied the Fe-Al-Mn-C alloy system in order to replace more expensive Fe-Cr-Ni-C stainless steels up to 1980's [12-14]. Since the early 2000's, interests in the low-density steels with high strength and toughness are activated again for structural, automotive, and military applications.

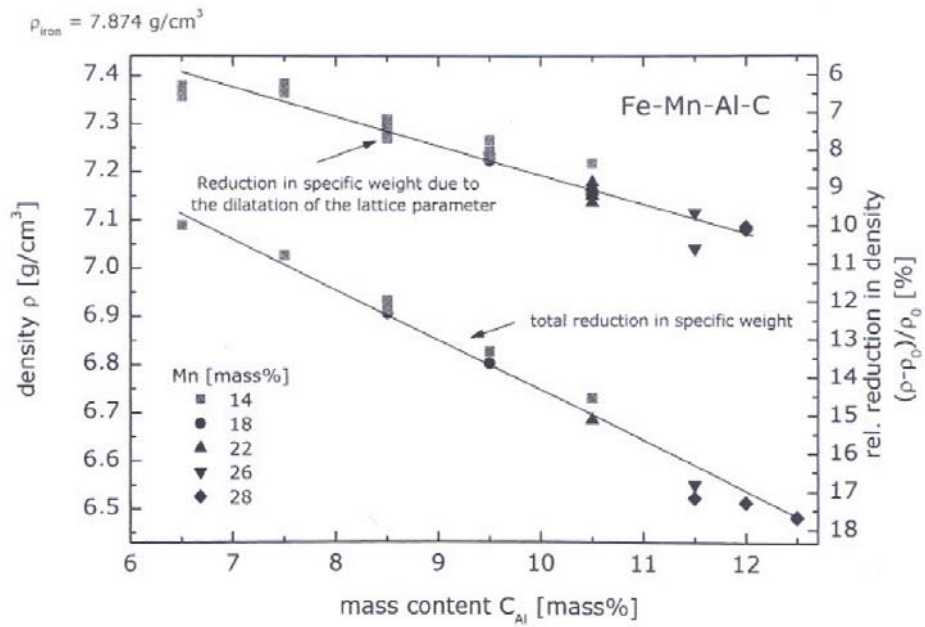


Figure 1.1 Density as function of the aluminium concentration under Fe-Al-Mn-C alloy system with varying manganese contents (14 to 28 wt.%) [6].

1.2 Classification of the low-density steels

Low-density steels can be categorized into ferrite-based and austenite-based (including multiphase-based) alloys, depending on their constituent phases. Ferrite-based Fe–Al alloys containing Al contents up to ~10 wt.% and some microalloying elements such as Ti, Nb and V show a good strength-ductility balance with density reduction to $\sim 7.0 \text{ g cm}^{-3}$ [15, 16]. However, aluminum addition in ferrite-based Fe–Al alloys was reported to increase the ductile-to-brittle transition temperature, and induced the cleavage fracture in ferrite matrix even at the room temperature with Al contents of approximately 7 wt. % [17]. Austenite-based alloys, which contain manganese contents at rates normally exceeding 15 wt.% as well as added aluminum up to ~12 wt.%, exhibit outstanding mechanical properties (tensile strength: 0.8–1.5 GPa, elongation: 30–80 %) as well as density reduction to $\sim 6.7 \text{ g cm}^{-3}$ [2, 6, 18-23]. Compared to the ferrite-based Fe–Al alloys, the austenite-based low-density steels show superior mechanical properties and weight reduction rates. Several representative low-density steels, which were developed until a recent date, are summarized in Table 1.1 exhibiting nominal chemical composition and mechanical properties.

Table 1.1 The representative low-density steels with nominal chemical composition and mechanical properties.

Matrix Phase	C (wt.%)	Mn (wt.%)	Al (wt.%)	Other (wt.%)	UTS (MPa)	EI (%)	Ref.
Ferritic	< 0.03	0.03~0.2	5~9	-	300~500	20~30	[15]
	< 0.2	< 3.5	2.5~10	-	400~600	20~30	-
	0.02~0.04	15~25	3	Si 3	600~1100	60~90	[2]
Austenitic & Multi-phase	0.5~2.0	18~35	8~12	(Si 3~6)	600~1100	25~70	[6]
	0.3~0.4	3~4	5~6	-	700~800	27~34	[18]
	0.15~0.5	6~12	5~6	Si 0.05~0.5	700~1000	35~60	[19, 20]
Austenitic & Multi-phase	0.8~0.9	15~17	8~10	Ni 4.9	1300~1500	20~35	[21]
	0.7~1.1	28~32	9~12	(Si 1.0)	800~1100	30~70	[22, 23]

1.3 Motivations of the thesis

After austenite-based high-Mn low-density steels are aged at adequate temperature and time periods, many kinds of micro/nano-scale precipitates or intermetallic compounds are formed, such as κ -carbide ((Fe,Mn)₃AlC_x) [6, 18, 24], ordered bcc phases (B2 or D0₃) [21, 25], and β -Mn [22, 23, 26, 27] inside austenite matrix or ferrite grains. These precipitates have a profound effect on the mechanical properties of the low-density steels. Therefore, many studies especially in κ -carbide and B2 have performed in order to investigate their precipitation phenomena and its correlation with the mechanical properties [6, 21, 24, 25]. With regard to β -Mn, some reports showed that the β -Mn phase significantly deteriorates the mechanical properties of high-Mn alloys, causing brittle fractures and decreasing impact energy [24, 28]. However, there is still a paucity of characterization research on the β -Mn phase in terms of the formation behavior, microstructural evolution, and its effects on mechanical and fracture properties of austenite-based high-Mn low-density steels. Therefore, this research investigates the microstructure and mechanical behavior of high-Mn low-density steels after processing treatments, by using complementary microstructural and mechanical characterization such as X-ray diffractometry (XRD), scanning electron microscopy (SEM), electron-back scattered diffraction (EBSD), transmission electron microscopy (TEM), uniaxial tensile test, and nanoindentation. The detailed research results are

structured in the thesis as follows.

Firstly in Chapter 2, the microstructure and intrinsic mechanical behavior of constitutional phases of an austenite-based low-density steel containing 11.4 wt.% Al were investigated with respect to β -Mn precipitation by aging heat treatment for various periods of time. Lattice expansion of austenite and κ -carbide induced by carbon diffusion due to β -Mn precipitation was examined by combined experimental techniques using XRD and an electron probe micro-analyzer (EPMA). The intrinsic mechanical properties of microstructural constituents including β -Mn were obtained by nanoindentation.

Secondly, in Chapter 3, β -Mn formation behavior of high-Mn low-density steels after aging treatments were investigated with samples containing different contents of Al and Si. The morphological characteristics and alloying element distribution of the β -Mn phase are systematically analyzed depending on the chemical composition of the steels. In addition, the effects of aging process on the fracture behavior are examined in uniaxial tensile tests combined with microstructural observations.

In Chapter 4, the aging behavior and orientation relationships among constitutional phases and precipitates in Fe-31.4Mn-11.4Al-0.89C low-density steel were studied. The misorientation-angle distribution, Rodrigues-Frank vector space, and orientation relationship stereogram (OR stereogram) are used to elucidate the orientation relationships across γ -matrix/ β -Mn and β -

Mn/ α -precipitate interphase boundaries. In addition, from both orientation relationships for γ -matrix/ β -Mn and β -Mn/ α -precipitate interfaces, the interface character between γ -matrix and α -precipitate is examined and compared to conventional fcc/bcc orientation relationships.

In Chapter 5, a dramatic difference in the macroscopic tensile behavior regarding yield strength, yield point, and strain hardening was introduced to two specimens of duplex low-density steel with the same nominal chemical composition, obtained under specific heat-treatment conditions. In order to understand the difference in the macro-scale mechanical behavior despite the similar microstructures, the intrinsic mechanical properties of each phase were measured by nano-indentation and analyzed by a combination with Hall-Petch relationship. In addition, the mechanical stability of retained austenite was investigated by *in-situ* EBSD and energy-dispersive X-ray spectroscopy (EDX) in TEM.

Lastly, total conclusion is addressed in Chapter 6.

1.4 References

- [1] B.C. De Cooman, *Curr Opin Solid St M*, 8 (2004) 285-303.
- [2] G. Frommeyer, U. Brux, P. Neumann, *ISIJ Int*, 43 (2003) 438-446.
- [3] H.N. Han, C.G. Lee, D.W. Suh, S.J. Kim, *Mat Sci Eng a-Struct*, 485 (2008) 224-233.
- [4] D.W. Suh, N.J. Kim, *Scripta Mater.*, 68 (2013) 337-338.
- [5] S.J. Park, Y.U. Heo, Y.H. Choi, K. Lee, H.N. Han, D.W. Suh, *JOM-US.*, 66 (2014) 1837-1844.
- [6] G. Frommeyer, U. Brux, *Steel Res. Int.*, 77 (2006) 627-633.
- [7] V.K. Saxena, M.S.G. Krishna, P.S. Chhaunker, V.M. Radhakrishnan, *Int J Pres Ves Pip*, 60 (1994) 151-157.
- [8] X.M. Zhu, Y.S. Zhang, *Corrosion*, 54 (1998) 3-12.
- [9] J. Herrmann, G. Inden, G. Sauthoff, *Acta Mater*, 51 (2003) 2847-2857.
- [10] A.S. Hamada, L.P. Karjalainen, *Can Metall Quart*, 45 (2006) 41-48.
- [11] H. Kim, D.W. Suh, N.J. Kim, *Sci Technol Adv Mat*, 14 (2013).
- [12] P.J. James, *J Iron Steel I*, 207 (1969) 54-&.
- [13] H.J. Lai, C.M. Wan, *J Mater Sci*, 24 (1989) 2449-2453.
- [14] F.C. Chen, P. Li, S.L. Chu, C.P. Chou, *Scripta Metall Mater*, 25 (1991) 585-590.
- [15] U. Brux, G. Frommeyer, J. Jimenez, *Steel Res*, 73 (2002) 543-548.
- [16] H.L. Yi, P. Chen, Z.Y. Hou, N. Hong, H.L. Cai, Y.B. Xu, D. Wu, G.D.

- Wang, *Scripta Mater.*, 68 (2013) 370-374.
- [17] J. Herrmann, G. Inden, G. Sauthoff, *Acta Mater.*, 51 (2003) 3233-3242.
- [18] K.G. Chin, H.J. Lee, J.H. Kwak, J.Y. Kang, B.J. Lee, *J. Alloy Compd.*, 505 (2010) 217-223.
- [19] S.J. Park, B. Hwang, K.H. Lee, T.H. Lee, D.W. Suh, H.N. Han, *Scripta Mater.*, 68 (2013) 365-369.
- [20] K. Lee, S.J. Park, Y.S. Choi, S.J. Kim, T.H. Lee, K.H. Oh, H.N. Han, *Scripta Mater.*, 69 (2013) 618-621.
- [21] S.H. Kim, H. Kim, N.J. Kim, *Nature*, 518 (2015) 77-79.
- [22] K. Lee, S.J. Park, J. Lee, J. Moon, J.Y. Kang, D.I. Kim, J.Y. Suh, H.N. Han, *J Alloy Compd.*, 656 (2016) 805-811.
- [23] K. Lee, S.J. Park, J. Moon, J.Y. Kang, T.H. Lee, H.N. Han, *Scripta Mater.*, 124 (2016) 193-197.
- [24] R.A. Howell, D.C. Van Aken, *Iron Steel Technol.*, 6 (2009) 193-212.
- [25] M.C. Ha, J.M. Koo, J.K. Lee, S.W. Hwang, K.T. Park, *Mat Sci Eng a-Struct.*, 586 (2013) 276-283.
- [26] K.H. Han, W.K. Choo, *Metall. Trans. A*, 20 (1989) 205-214.
- [27] I.S. Kalashnikov, O. Ayselrad, A. Shalkevich, L.D. Chumakova, L.C. Pereira, *J. Mater. Process Tech.*, 136 (2003) 72-79.
- [28] S.C. Tjong, *Mater. Charact.*, 24 (1990) 275-292.

Chapter 2

Effect of aging treatment on microstructure and intrinsic mechanical behavior of Fe–31.4Mn–11.4Al–0.89C low-density steel

2.1 Introduction

The demand for reduced weight in transportation systems has been growing in the automotive and defense sectors, to reduce greenhouse gas emissions and improve energy efficiency. Much research within the steel industry has been focused on lowering the density of steel while maintaining its high strength for automotive applications; hence, many kinds of low-density steels having excellent specific strength and ductility have been developed [1-17]. Low-density steels can be categorized into ferrite-based and austenite-based steels, depending on their constituent phases. Among them, austenite-based low-density steels based on the Fe-Al-Mn-C system, which have higher Mn and Al additions than ferrite-based steels, show superior mechanical properties and weight reduction rates [1, 8-17].

After these steels are aged at adequate temperature and time periods, micro/nano-scale precipitates or intermetallic compounds are formed, such as

κ -carbide ((Fe,Mn)₃AlC_x) [8-12], B2 (FeAl) [13-15], and β -Mn [16-18]. These precipitates have a profound effect on the mechanical properties of low-density steel. Therefore, many studies on κ -carbide and B2 have already been conducted in order to investigate their effect on macroscopic deformation behavior [8, 10, 12, 14, 15]. With regard to β -Mn, some reports showed the precipitation of α -ferrite and β -Mn with a lamellar-type structure along austenite grain boundaries in austenitic alloys containing about 9 wt.% Al [16-18]. However, there is still a paucity of characterization research on the microstructural evolution and intrinsic behavior of constitutional phases including β -Mn, especially in low-density steel with a high Al content above 11 wt.%.

In the present study, the microstructure and intrinsic mechanical behavior of constitutional phases of an austenite-based low-density steel containing 11.4 wt.% Al were investigated with respect to β -Mn precipitation by aging heat treatment for various periods of time. Lattice expansion of austenite and κ -carbide induced by carbon (C) diffusion due to β -Mn precipitation was examined by combined experimental techniques using X-ray diffractometry (XRD) and an electron probe micro-analyzer (EPMA). The intrinsic mechanical properties of microstructural constituents including β -Mn were obtained by nanoindentation. In addition, nanoindentation results were correlated with age hardening and C diffusion of the low-density steel with

consideration for β -Mn precipitation.

2.2 Experimental procedure

Steel with a chemical composition of Fe–31.4Mn–11.4Al–0.89C (wt.%) was fabricated by vacuum induction melting using electrolytic iron (>99.9 % Fe), electrolytic manganese (>99.9 % Mn), aluminum (>99.5 % Al) and graphite (>99.9 % C). The alloy also contains 0.014 wt.% Si, 0.010 wt.% S and 0.003 wt.% P which were originated from the materials used for melting. The ingot was soaked at 1,200 °C for two hours and hot-rolled to an 8 mm thickness, with a final rolling temperature above 900 °C. The total reduction in thickness by hot-rolling process was 90%. After hot rolling, the plate was cooled to room temperature by water spraying. The plate was solution-treated at 1,050 °C for two hours and quenched by water. Test coupons cut from the solution-treated plate were aged at 550 °C for various periods of time including 300, 1,000 and 10,000 minutes. For convenience here, the specimen which was solution-treated at 1,050 °C is referred to as ST, and the specimens aged at 550 °C for 300 minutes, 1,000 minutes, and 10,000 minutes are referred to as A300, A1000 and A10000, respectively.

The samples for microstructural observation and nanoindentation tests were prepared by mechanical grinding followed by electropolishing with a solution of 20% perchloric acid, 10% ethylene glycol monobutyl ether and 70% ethanol. The microstructure was observed on the longitudinal section, including the rolling and normal directions of a specimen, by utilizing an electron

backscatter diffraction (EBSD) system equipped with a field emission scanning electron microscope. A critical misorientation angle of 15° was taken for grain identification. Constitutional phases in the microstructure of the specimens were identified by XRD using Cu $K\alpha$ radiation with a graphite monochromator. The lattice parameter of the austenite phase was measured using Cohen's method [19]. In the case of κ -carbide, most reflections overlap with those of austenite, and therefore its lattice parameter was determined simply by averaging the lattice parameter values obtained from the positions of $(100)_\kappa$ and $(110)_\kappa$ reflections which do not overlap with reflections of other phases. The specimens for transmission electron microscopy (TEM) were prepared in a twin-jet electrolytic polishing apparatus using a solution of 10% perchloric acid and 90% methanol at -25°C . Partitioning of alloying elements in a region including β -Mn and austenite phase in the A1000 specimen was analyzed using EPMA. The EBSD scanned area of $33.15 \times 33.15 \mu\text{m}$ was analyzed with a spacing of $0.13 \mu\text{m}$ between each point. Quantitative line scanning was also conducted across the interphase boundaries between β -Mn and austenite matrix.

Vickers microhardness measurements were performed under a load of 1 kgf maintained for 10 seconds. Nanoindentation tests were carried out in load control mode, applied at a constant loading rate of 1 mNs^{-1} to a maximum of 5 mN. A Berkovich-type diamond tip with a centreline-to-face angle of 65.3° was used. To investigate the change of intrinsic mechanical property of each phase

during heat treatment, 100 indentations were made in a 10×10 rectangular array at intervals of $10 \mu\text{m}$ between each indentation for the ST and A1000 specimens. To exclude any grain boundary effect on the indentation results, only those indentations located inside the grains sufficiently far away from the grain boundaries were selected for analysis, guided by a scanning probe microscope (SPM). This made it possible to evaluate grain morphologies and precisely identify the areas where the indentation was performed [5, 20-23]. Statistical information about nano-hardness of constitutional phases was obtained using indentation data of at least 11 points for each phase.

2.3 Microstructural analysis

Figures 2.1(a-d) show EBSD phase maps of the ST, A300, A1000 and A10000 specimens, respectively. The ST specimen is mostly composed of an austenite phase with some ferrite, whose volume fraction measured by EBSD is 16.4%. The β -Mn phase indicated in green nucleates at both ferrite/austenite phase boundaries and austenite/austenite grain boundaries as shown in Figure 2.1(b). This means that both boundaries may be suitable for the nucleation site of the β -Mn phase. Figures 2.1(c, d) present that β -Mn grains grow extensively into the austenite matrix with lath-type morphology during further heat treatment. The microstructural morphology of the β -Mn phase is clearly different from those in alloys having similar chemical composition except for a lower Al content of about 9 wt.%, which showed a lamellar-type co-precipitation of the β -Mn phase with α -ferrite [16, 17]. The distinction of the precipitation behavior might originate from the Al content being higher than 9 wt.%, which renders the austenite phase less stable and then the driving force for β -Mn precipitation bigger. This precipitation behavior especially in terms of morphological characteristics is quite similar to that of Widmanstätten ferrite, which nucleates and grows at a lower transformation temperature and with a relatively higher driving force than polygonal ferrite [24].

The grain size and volume fraction of each phase in the specimens measured by EBSD are listed in Table 2.1. As the β -Mn phase grows

exclusively into the austenite matrix during aging treatment, the volume fraction of austenite decreases clearly, whereas the ferrite fraction is almost maintained without significant change. The average grain size of the ferrite phase in A10000 specimen is dramatically reduced, which can be attributed to precipitation of microscopic body-centered cubic (bcc), as shown in the magnified phase map inserted in Figure 2.1(d). The fine bcc phase might be an ordered structure such as B2 or D03, which are hardly distinguishable from a disordered bcc (A2) phase by EBSD pattern.

TEM observations were carried out on the A1000 specimen. Figure 2.2(a) shows a bright-field image of a region including β -Mn grains. The β -Mn grains present a lath-type shape which has a narrow and sharp end of growth front. This morphology has an advantage for fast growth because alloying elements can diffuse for partitioning in all directions at the tip of the phase boundary during phase transformation. A selected area diffraction pattern of a β -Mn grain is shown in Figure 2.2(b). The lattice parameter of the β -Mn phase measured from the diffraction pattern is 6.293 Å, which is close to a published value of 6.315 Å [25]. Figure 2.2(c) shows a bright-field image of the matrix region. Nano-sized κ -carbides are formed within the austenite matrix. Formation of fine coherent κ -carbides within austenite grains during aging or cooling from high temperature is typical of austenitic alloys having high C and Al contents [8, 10-12, 16-18]. The selected area diffraction pattern of the matrix region

presented in Figure 2.2(d) exhibits superlattice reflections such as $\{100\}$ and $\{110\}$ spots due to the ordered characteristic of $E2_1$ perovskite crystal structure of κ -carbide.

XRD profiles of the specimens which were solution-treated and aged are shown in Figure 2.3. The XRD profile of the ST specimen reveals that the bcc ordered phase (B2 or D03) indicated by $(100)_{B2}$ or $(200)_{D03}$ reflection coexists with the austenite and ferrite phase before aging treatment. It might be attributed to partial ordering in ferrite solid solution due to high Al content [8]. The diffraction peaks of κ -carbide appear after aging for 30 minutes. After aging for 300 minutes, (310) reflection of β -Mn start to show up and the intensity of the diffraction peaks of β -Mn increases with further aging, which corresponds with the microstructural observation by EBSD as shown in Figure 2.1. Notably, the diffraction peaks of austenite and κ -carbide show a shift to a lower diffraction angle as indicated by the red arrows in Figure 2.3 after aging for 300 minutes, when β -Mn starts to precipitate at austenite grain boundaries. Figure 2.4(a) presents sequential changes in $(220)_\gamma$ reflection located at around 72° of 2θ angle, which clearly shows the peak shift of the austenite phase. The lattice parameters of austenite and κ -carbide simultaneously increase after aging for 300 minutes, as shown in Figure 2.4(b). The increase of lattice parameters implies that partitioning of alloying elements occurs due to the formation of β -Mn.

To investigate the partitioning of alloying elements, EPMA analysis on the A1000 specimen was conducted with respect to the phase boundaries between β -Mn and austenite phases. Figure 2.5(a) shows the EBSD phase map of the region where EPMA analysis was carried out. Figures 2.5(b-e) present quantitative EPMA elemental maps of C, Al, Mn and Fe, respectively. It is clearly seen that Al is partitioned in the ferrite grains on the right side of the quantitative map, while Mn is concentrated in the austenite and β -Mn phases. These partitioning might occur during the solution heat treatment prior to aging treatment [14]. The region of the austenite phase presents a higher C content than the β -Mn and ferrite phases. Furthermore, the C content becomes higher at the region closer to the phase boundaries between austenite and β -Mn. On the contrary, the other substitutional elements such as Al, Mn and Fe show little partitioning between the β -Mn and austenite phases.

For quantitative analysis of the difference in C composition, EPMA line scanning including the interphase boundaries was performed. The C content profile along the sky-blue line shown in Figure 2.5(a) is displayed in Figure 2.5(f). It can be confirmed that a significant gradient of C concentration exists inside the austenite grain. The maximum and minimum values of the C content of the austenite grain are 1.519 wt.% and 0.660 wt.%, which are located near the phase boundary and the center region, respectively. It is known that the C solubility of β -Mn in the binary Mn-C system is lower than 0.002 wt.%, which

is the equilibrium C solubility at 1,095 K [26]. Thus, it is conceivable that C atoms are expelled from β -Mn, and diffuse into austenite including the fine coherent κ -carbides during formation of β -Mn. Because of the C diffusion, the austenite region adjacent to β -Mn shows enriched C contents compared to the center region of the austenite grain.

As solute C atoms make expansion of austenite lattice [22, 25], the inhomogeneous C distribution can affect inhomogeneity in lattice parameter of austenite phase, which cause broadening of XRD peak profile. The measured full width at half maximum (FWHM) value of $(220)_\gamma$ reflection shows remarkable increase from 0.680° (A300) to 1.324° (A1000), which can be attributed to the inhomogeneous C distribution evolved in austenite due to formation of β -Mn. Prolonged aging over 1000 min reduced the FWHM value of $(220)_\gamma$ reflection to 0.369° (A10000). It is conceivable that C distribution becomes more homogeneous in austenite after aging over 1000 min, which is probably due to reduced grain size of austenite and reduced rate of β -Mn volume increase (Table 1).

The amount of C enrichment in the austenite phase can be estimated from the increase of lattice parameter measured by XRD, using an empirical equation for the lattice parameter of austenite [27]:

$$a(\text{\AA}) = 3.578 + 0.033[\text{wt.\% C}] + 0.00095[\text{wt.\% Mn}] + 0.0056[\text{wt.\% Al}] \quad (1)$$

where a is the lattice parameter of austenite. As there is no significant partitioning of Mn and Al during β -Mn formation, as shown in Figure 2.5, it is assumed that only the C enrichment contributes to the expansion of the lattice parameter of austenite. The lattice parameter of austenite phase increases from 3.706 \AA (ST) to 3.761 \AA (A10000). The estimated difference of C content between the ST and A10000 specimens is about 1.67 wt.%. The C content in austenite in the ST specimen might be higher than the nominal C content of 0.89 wt.%, due to the presence of ferrite; then the C content in austenite in the A10000 specimen might be higher than 2.56 wt.%. This is a very high value compared with the maximum C solubility of 2.11 wt.% in austenite of the Fe-C system [28]. The estimated high C content in austenite of the A10000 specimen can be attributed to the existence of κ -carbide in austenite and the expanded lattice due to the high Al content. The C enrichment stabilizes the austenite phase; therefore, it probably slows down further β -Mn transformation. In addition, the high C content may facilitate further formation of κ -carbide within austenite grains or at grain boundaries.

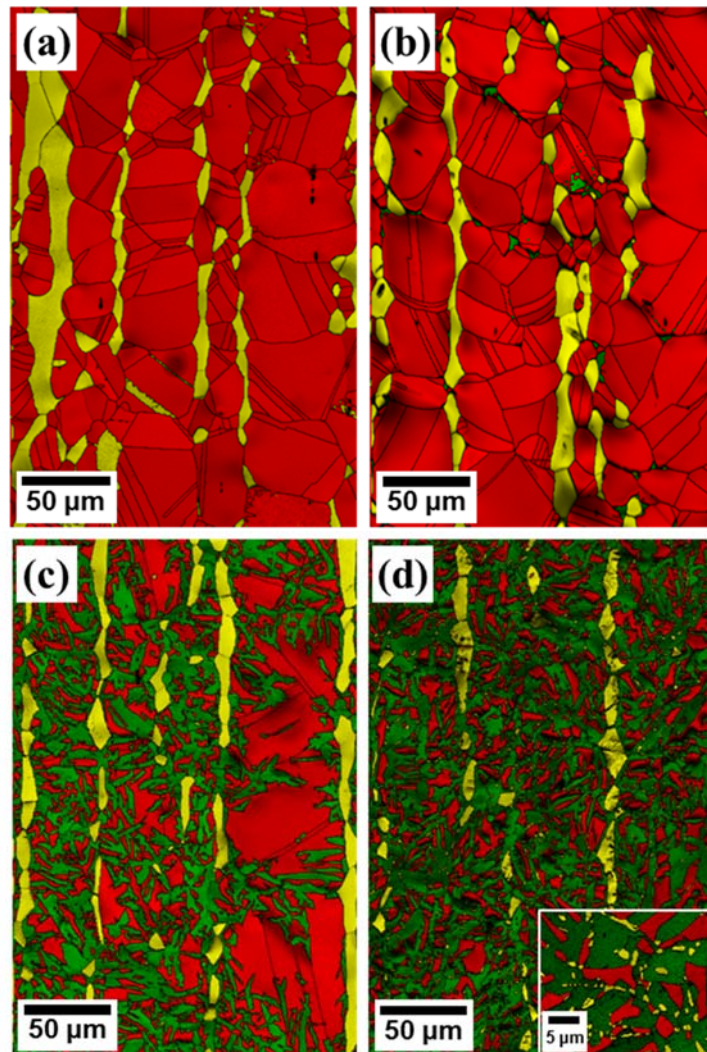


Figure 2.1 EBSD phase map of the: (a) ST; (b) A300; (c) A1000, and; (d) A10000 specimens (■ FCC; ■ BCC; ■ β -Mn). The horizontal direction is a normal direction of the specimen. The inserted EBSD phase map with magnification in (d) represents microscopic bcc ordered phases (B2 or D03) precipitated in the A10000 specimen.

Table 2.1 Grain size and volume fraction of each phase in the specimens obtained from EBSD.

Sample	Grain size (μm)			Volume fraction (%)		
	Austenite	Ferrite	β -Mn	Austenite	Ferrite	β -Mn
ST	27.5	28.6	-	83.6	16.4	-
A300	26.0	19.0	4.3	85.7	13.2	1.1
A1000	22.0	25.0	15.7	44.3	12.4	43.3
A10000	9.1	9.4	14.8	30.6	13.2	56.2

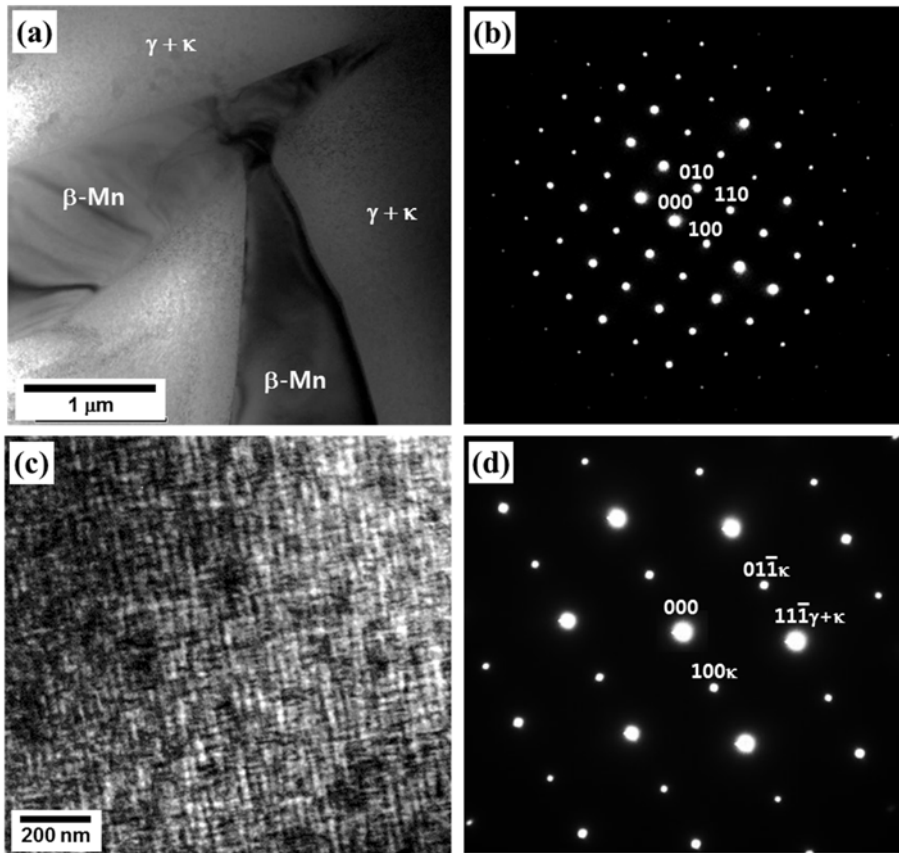


Figure 2.2 TEM micrographs and diffraction patterns of the A1000 specimen. (a) Bright-field image including $\beta\text{-Mn}$ grains. (b) Selected area diffraction pattern showing $[001]$ zone of the $\beta\text{-Mn}$ phase. (c) Bright-field image of matrix region. (d) Selected area diffraction pattern showing $[011]$ zone of the austenite and κ -carbide.

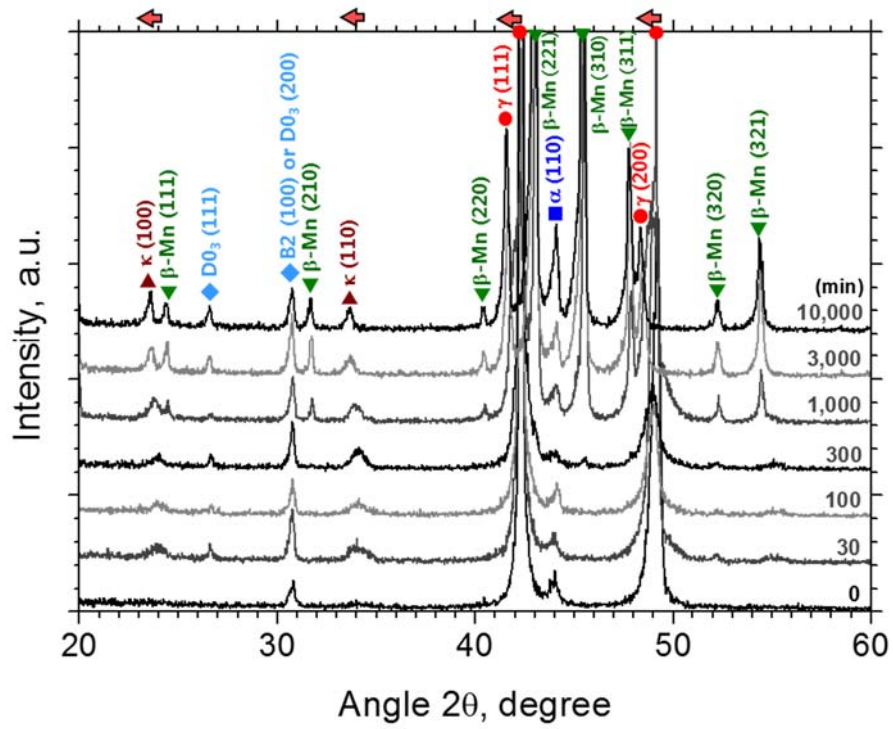


Figure 2.3 X-ray diffraction diagrams of the overall specimens. Red arrows indicate the peak shift of austenite and κ -carbide.

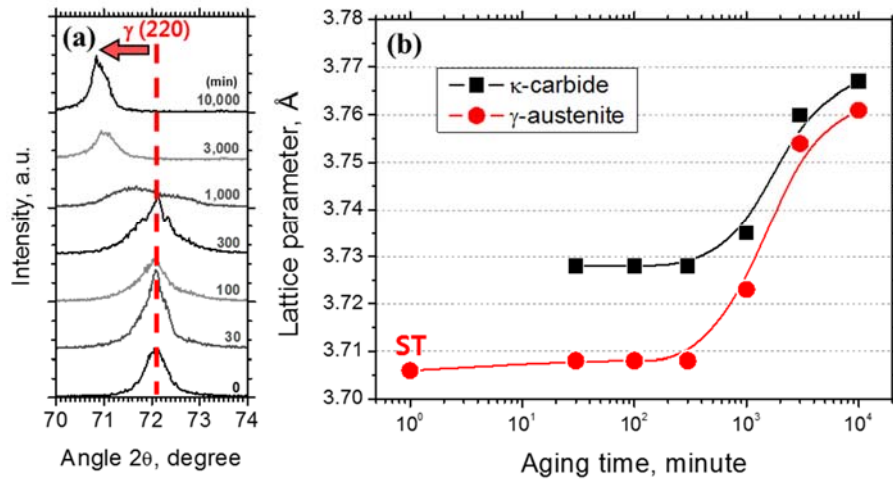


Figure 2.4 (a) Sequential changes in magnified γ (220) peak in Fig. 2.3 on aging heat treatment. Red arrows indicate the peak shift of austenite and κ -carbide. (b) Lattice parameters of austenite and κ -carbide of the overall specimens calculated from X-ray diffraction diagrams as a function of aging time.

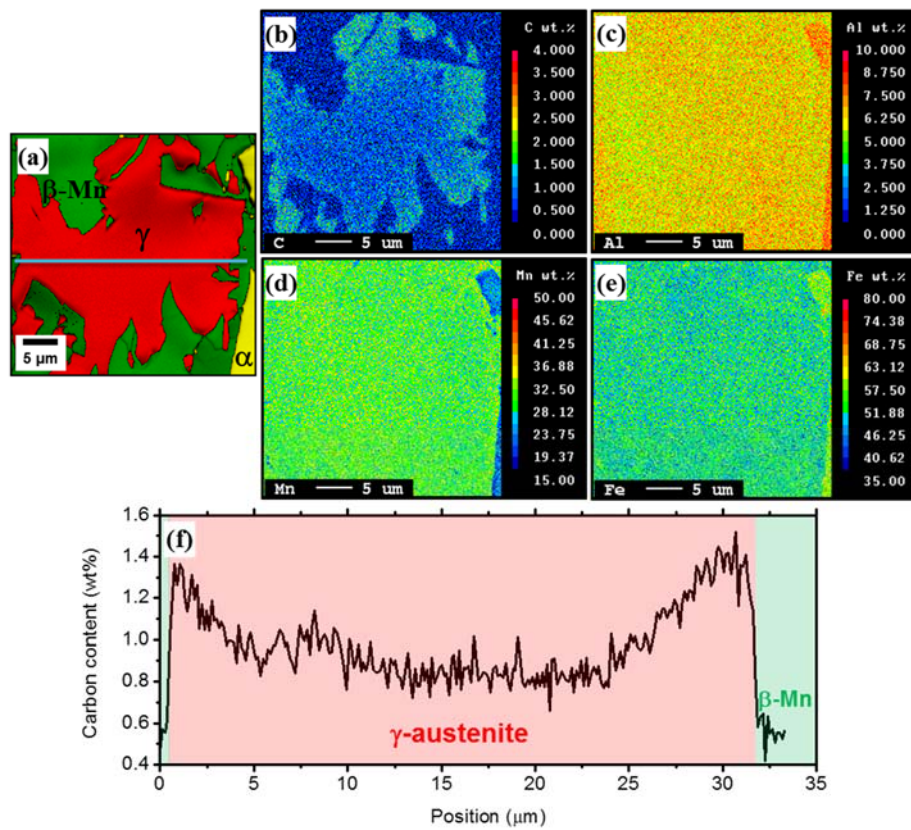


Figure 2.5 (a) EBSD phase map of the A1000 specimen (■ FCC; ■ BCC; ■ β-Mn) before EPMA analysis. EPMA elemental mapping in the same area where the EBSD scan occurred: (b) carbon; (c) aluminum; (d) manganese, and; (e) iron map. (f) Carbon content profile of the sky-blue line in (a).

2.4 Intrinsic mechanical properties: Nanoindentation analysis

To obtain the intrinsic mechanical properties of microstructural constituents, nanoindentation tests were carried out on the ST and A1000 specimens. Figure 2.6(a) shows an EBSD phase map of some indented areas in the A1000 specimen after nanoindentation tests. Based on the EBSD phase map, indentation results are classified according to each constituent phase. Figures 2.6(b-d) present SPM images with an indentation mark of each phase in the same area indicated by triangles in Figure 2.6(a). Figures 2.6(e, f) give load–displacement curves obtained by nanoindentation of all constituent phases in the ST and A1000 specimens. Notably, the load–displacement curves of the A1000 specimen show that the β -Mn phase is quite mechanically hard from shallow indentation depths despite the same maximum load in comparison with the other constituent phases. Nano-hardness is calculated from the load–displacement curve, and it is given as follows:

$$H = \frac{P_{\max}}{A} \quad (2)$$

where P_{\max} is the maximum load and A is the projected contact area, which is a function of the contact depth with the sample, h_c . The nano-hardness of each phase in the ST and A1000 specimens is shown in Table 2.2. The nano-hardness

of β -Mn in the A1000 specimen is 13.28 ± 0.16 GPa. The hardness of the austenite phase and its standard deviation remarkably increase with heat treatment. On the contrary, the ferrite hardness is maintained without any appreciable change during aging treatment.

In order to examine precisely the correlation between the age hardening behavior and the intrinsic mechanical properties of each phase, the Vickers hardness of the overall specimens is shown together with the nano-hardness as a function of aging time in Figure 2.7. Until the aging treatment for 300 minutes, the Vickers hardness increases gradually above 300 HV, which stems from the effect of mixture of austenite and κ -carbide formed by spinodal decomposition [12]. After an aging time of 1,000 minutes, the specimens show dramatic secondary hardening, with hardness higher than 700 HV. In consideration of both the microstructural analysis and nano-hardness results of the A1000 specimen, the dramatic increase of the Vickers hardness is certainly due to β -Mn precipitation.

The average value of the nano-hardness of the austenite phase increases from 4.93 GPa (ST) to 7.67 GPa (A1000). The increase of nano-hardness originates from the increase of C content inside austenite grains caused by β -Mn precipitation during aging treatment. The standard deviation of nano-hardness in the austenite phase increases from 0.19 GPa (ST) to 1.30 GPa (A1000). To investigate the increase in the standard deviation, the nano-

hardness results of the austenite phase in the A1000 specimen are classified as boundary and center region, based on a distance of 7 μm between a nanoindentation spot and grain boundary. The nano-hardnesses of the boundary region and the center region are 8.11 ± 0.28 GPa and 5.53 ± 0.09 GPa, respectively. Therefore, the increase of the standard deviation is attributed to an inhomogeneous distribution of C content in the austenite phase, as shown in Figure 2.5(f). Consequently, the β -Mn precipitation affects not only the age hardening of low-density steel in itself but also the intrinsic properties of the austenite matrix due to C diffusion.

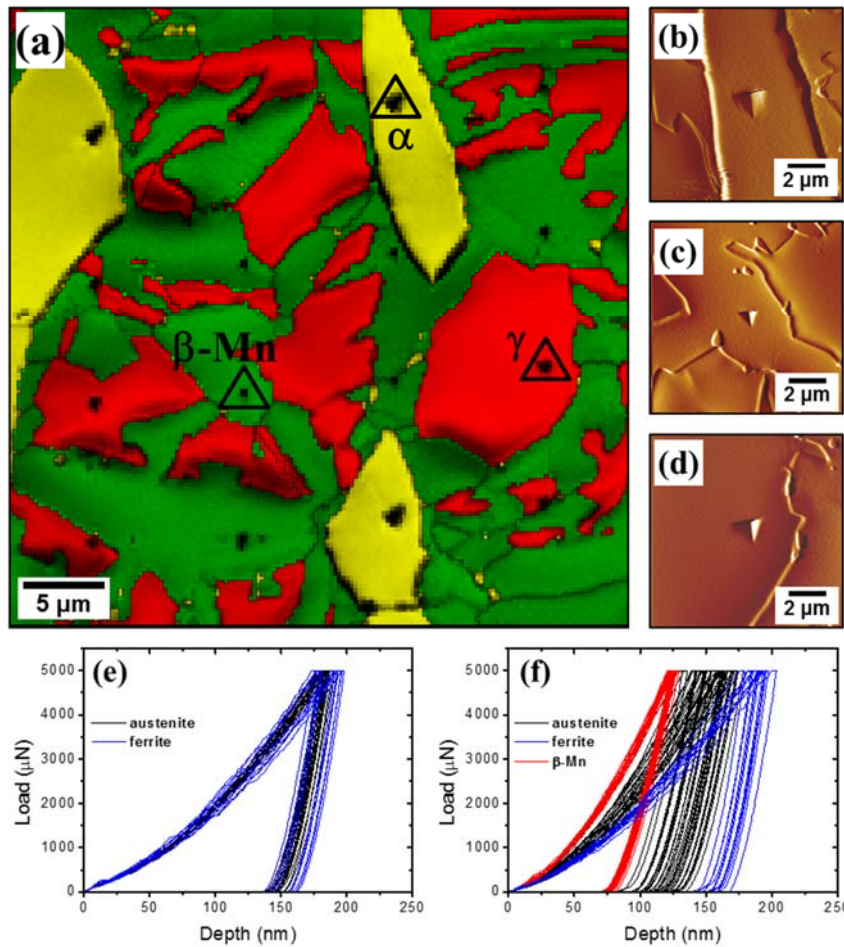


Figure 2.6 (a) EBSD phase map of the A1000 specimen (■ FCC; ■ BCC; ■ β -Mn) after indentation. SPM image of the indents in the same area marked with triangles shown in (a): (b) ferrite grain; (c) β -Mn grain, and; (d) austenite grain. Nanoindentation load-displacement curves of all constituent phases in the (e) ST and (f) A1000 specimens.

Table 2.2 Nano-hardness calculated from the load–displacement curves (numbers in parenthesis are the standard deviation).

Sample	Austenite (GPa)	Ferrite (GPa)	β -Mn (GPa)
ST	4.93 (0.19)	4.67 (0.41)	-
A1000	7.67 (1.30)	4.73 (0.31)	13.28 (0.43)

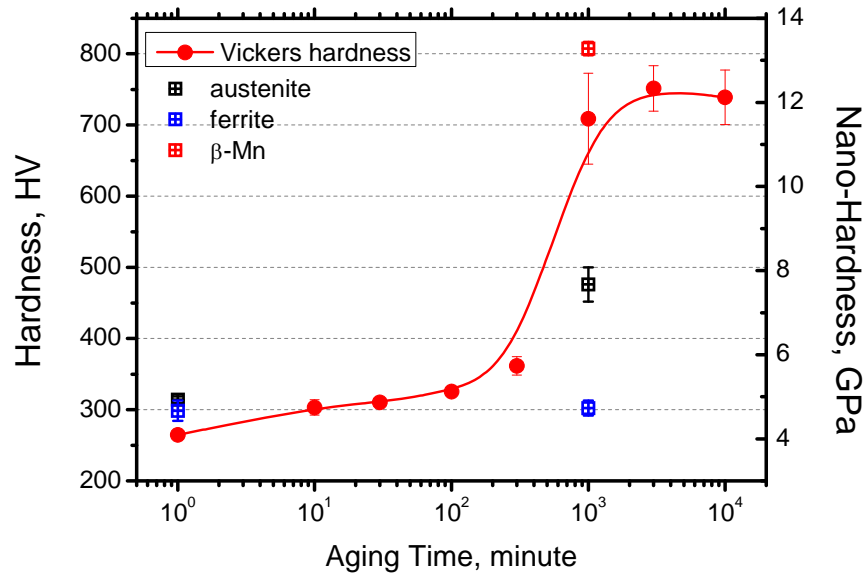


Figure 2.7 Vickers hardness of the overall specimens and nano-hardness of each constituent phase in the ST and A1000 specimens obtained from nanoindentation as a function of aging time.

2.5 Conclusion: Effect of aging treatment on microstructure and intrinsic mechanical behavior

In this study, the change of the microstructure and intrinsic mechanical properties of Fe–31.4Mn–11.4Al–0.89C low-density steel under aging heat treatment was studied by nanoindentation combined with complementary microstructural characterization using XRD, EBSD, TEM, and EPMA. From the microstructural evolution, the β -Mn phase nucleated at both ferrite/austenite phase boundaries and austenite/austenite grain boundaries after aging for 300 minutes at 550 °C, and grew deeply into the austenite matrix by further aging treatment. The XRD analysis indicated the lattice expansion of austenite and κ -carbide from the peak shift. This result was instantiated with C diffusion to the austenite matrix due to β -Mn precipitation, which was examined by EPMA analysis. The Vickers hardness increased dramatically, to more than 700 HV after an aging time of 1,000 minutes. The secondary aging behavior originated from the precipitation of the β -Mn phase whose nano-hardness was measured as 13.28 ± 0.16 GPa. In addition, the average value and standard deviation of the nano-hardness of the austenite phase increased after 1,000 minutes of aging from the solution-treated state. It arose from the increase and inhomogeneous distribution of C content caused by β -Mn precipitation, which corresponded to the results of microstructural characterization.

2.5 References

- [1] G. Frommeyer, U. Brux, P. Neumann, *ISIJ Inter.* 43 (2003) 438-446.
- [2] S.S. Sohn, B.J. Lee, S. Lee, J.H. Kwak, *Met. Mater. Int.* 21 (2015) 43-53.
- [3] R. Rana, C. Liu, R.K. Ray, *Acta Mater.* 75 (2014) 227-245.
- [4] S.J. Park, B. Hwang, K.H. Lee, T.H. Lee, D.W. Suh, H.N. Han, *Scripta Mater.* 68 (2013) 365-369.
- [5] K. Lee, S.J. Park, Y.S. Choi, S.J. Kim, T.H. Lee, K.H. Oh, H.N. Han, *Scripta Mater.* 69 (2013) 618-621.
- [6] S.J. Park, Y.U. Heo, Y.H. Choi, K. Lee, H.N. Han, D.W. Suh, *JOM-US.* 66 (2014) 1837-1844.
- [7] J.B. Seol, D. Raabe, P. Choi, H.S. Park, J.H. Kwak, C.G. Park, *Scripta Mater.* 68 (2013) 348-353.
- [8] G. Frommeyer, U. Brux, *Steel Res. Int.* 77 (2006) 627-633.
- [9] K.G. Chin, H.J. Lee, J.H. Kwak, J.Y. Kang, B.J. Lee, *J. Alloy Compd.* 505 (2010) 217-223.
- [10] R.A. Howell, D.C. Van Aken, *Iron Steel Technol.* 6 (2009) 193-212.
- [11] J. Jeong, C.Y. Lee, I.J. Park, Y.K. Lee, *J. Alloy Compd.* 574 (2013) 299-304.
- [12] L.N. Bartlett, D.C. Van Aken, J. Medvedeva, D. Isheim, N.I. Medvedeva, K. Song, *Metall. Trans. A* 45A (2014) 2421-2435.
- [13] M.S. Chen, H.C. Cheng, C.F. Huang, C.Y. Chao, K.L. Ou, C.H. Yu, *Mater.*

- Charact. 61 (2010) 206-211.
- [14] M.C. Ha, J.M. Koo, J.K. Lee, S.W. Hwang, K.T. Park, *Mat. Sci. Eng. A Struct. Mater.* 586 (2013) 276-283.
- [15] S.H. Kim, H. Kim, N.J. Kim, *Nature* 518 (2015) 77-79.
- [16] K.H. Han, W.K. Choo, *Metall. Trans. A* 20 (1989) 205-214.
- [17] K. Sato, K. Tagawa, Y. Inoue, *Metall. Trans. A* 21 (1990) 5-11.
- [18] I.S. Kalashnikov, O. Acselrad, A. Shalkevich, L.D. Chumakova, L.C. Pereira, *J. Mater. Process Tech.* 136 (2003) 72-79.
- [19] M.U. Cohen, *Rev. Sci. Instrum.* 6 (1935) 68-74.
- [20] T.H. Ahn, K.K. Um, J.K. Choi, D.H. Kim, K.H. Oh, M. Kim, H.N. Han, *Mat. Sci. Eng. A Struct. Mater.* 523 (2009) 173-177.
- [21] T.H. Ahn, C.S. Oh, D.H. Kim, K.H. Oh, H. Bei, E.P. George, H.N. Han, *Scripta Mater.* 63 (2010) 540-543.
- [22] J.Y. Kang, D.H. Kim, S.I. Baik, T.H. Ahn, Y.W. Kim, H.N. Han, K.H. Oh, H.C. Lee, S.H. Han, *ISIJ Inter.* 51 (2011) 130-136.
- [23] D.D. Zhu, D. Dong, C.Y. Ni, D.F. Zhang, Z.Z. Zhou, H.W. Wang, Z.J. Wei, *Mater. Charact.* 99 (2015) 243-247.
- [24] H.K.D.H. Bhadeshia, R.W.K. Honeycombe, *Steels : microstructure and properties*, 3rd ed., Elsevier, Butterworth-Heinemann, Amsterdam ; Boston, 2006.
- [25] W.B. Pearson, *A handbook of lattice spacings and structures of metals and alloys*, Pergamon Press, New York, 1958.

- [26] D. Djurovic, B. Hallstedt, J. von Appen, R. Dronskowski, *Calphad* 34 (2010) 279-285.
- [27] D.J. Dyson, B. Holmes, *J. Iron Steel Inst.* 208 (1970) 469-474.
- [28] G. Krauss, *Steels : heat treatment and processing principles*, ASM International, Materials Park, Ohio, 1989.

Chapter 3

β -Mn formation and aging effect on the fracture behavior of high-Mn low-density steels

3.1 Introduction

Low-density steels have drawn increasing amounts of attention in recent years due to their promising mechanical strength, crash-worthiness, and extensive ductility, together with a reduced specific density [1-14]. The excellent properties of these steels can enable applications in lightweight automotive vehicles and military armor. The low-density steels usually contain aluminum as a substitutional light element, which provides a density reduction effect by means of substitution and lattice expansion. There are many types of the low-density steels based on constitutional phases, such as ferrite-based and austenite-based (including multiphase-based) alloys. Among them, austenite-based alloys, which contain manganese contents at rates normally exceeding 15 wt.% as well as added aluminum up to ~12 wt.%, exhibit outstanding mechanical properties (tensile strength: 0.8–1.5 GPa, elongation: 30–80 %) as well as density reduction to ~6.7 g cm⁻³ [8-14]. These alloys can have κ -carbide and β -Mn phases in their microstructure depending on the chemical

composition and heat-treatment condition. After κ -carbides are precipitated within the austenite matrix at the early stage of isothermal aging, the β -Mn formation occurs by overaging treatment [9, 14-19]. In respect of the β -Mn, it is known that the β -Mn phase significantly deteriorates the mechanical properties of high-Mn alloys, causing brittle fractures and decreasing impact energy [9, 15, 16].

To verify the mechanical reliability and durability of austenite-based high-Mn low-density steels, it is necessary to examine the formation and growth behavior of the β -Mn phase. Several microstructural studies for the β -Mn formation process in high-Mn alloys were conducted some time ago [17-19]. However, these studies did not examine the influence of additions of alloying elements such as aluminum and silicon on the formation behavior of the β -Mn, as they were limited to a specific alloy system. In contrast, this research investigates the β -Mn formation behavior of high-Mn low-density steels after aging treatments with samples containing different contents of Al and Si. The morphological characteristics and alloying element distribution of the β -Mn phase are systematically analyzed depending on the chemical composition of the steels. In addition, the effects of aging process on the fracture behavior are examined in uniaxial tensile tests combined with microstructural observations using scanning electron microscopy (SEM), electron-back scattered diffraction (EBSD) and transmission electron microscopy (TEM).

3.2 Experimental procedure

Three alloys were cast in a vacuum induction furnace. Their chemical compositions are presented in Table 3.1. The 9Al-1Si alloy has additional silicon content of 1 wt.% based on the composition of the 9Al alloy. The 11Al alloy has a higher content of aluminum than the others. The contents of carbon and manganese in the three alloys are nearly identical. The ingots were soaked at 1200 °C for two hours and hot-rolled to a thickness of 8 mm (~90% reduction) at a final temperature exceeding 900 °C. The hot-rolled plates were then cooled to room temperature by water spraying. After cooling, they were solution-treated at 1050 °C for two hours and subsequently quenched in water. The test specimens cut from the solution-treated plates were aged at 550 °C for various periods of time, including the maximum aging time of 10000 min. Vickers hardness measurements were carried out at 7~10 points for each specimen by applying a load of 1 kgf for 10 s. Using the measured hardness data, arithmetic average value and 95% confidence interval were calculated for each specimen. The microstructure was observed on the plane containing rolling and normal directions by means of optical microscopy and SEM equipped with EBSD and energy dispersive X-ray spectroscopy (EDS) systems. The specimens for the microstructural observations were prepared by mechanical polishing, followed by chemical etching with a 10% nital solution. For the EBSD measurements, the specimens were polished with a colloidal silica suspension at the final

polishing stage. TEM characterization was performed to analyze the ordered phase with a specimen prepared by a focused ion beam (FIB) system. Tensile tests were conducted with sub-sized specimens based on ASTM E8M at a crosshead speed of 2 mm/min. The fracture surface and the microstructure of the cross-sectional area adjacent to the fracture surface after the tensile test were observed using SEM and EBSD to investigate the occurrence of cracks and the crack propagation behavior.

Table 3.1 Chemical composition of the investigated alloys. (wt.%)

Alloy	C	Mn	Al	Si	Fe
9Al	0.80	31.52	8.73	0.01	bal.
9Al-1Si	0.89	31.62	8.74	1.01	bal.
11Al	0.89	31.35	11.39	0.01	bal.

3.3 Influence of alloying elements on the formation behavior of the κ -carbide and β -Mn

Figure 3.1 shows the Vickers hardness results of the 9Al, 9Al-1Si, and 11Al alloys as a function of the aging time at 550 °C. The microstructures of solution-treated (ST) specimens of the investigated alloys are shown in Figures 3.2(a-c), respectively. The ST specimens of the 9Al and 9Al-1Si alloys show the microstructure of the austenite single phase, while the ST specimen of the 11Al alloy shows a microstructure composed of an austenite matrix and a number of ferrite grains aligned along the rolling direction. The formation of a two-phase structure stems from the higher contents of aluminum, which acts as a ferrite stabilizer [6, 8, 9]. At the beginning of the aging treatment (< 30 min), the Vickers hardness of the 9Al-1Si and 11Al alloys increases more rapidly than that of the 9Al alloy. This primary age hardening response indicated by blue arrows in Figure 3.1 originates from the formation of nano-sized κ -carbides within the austenite matrix, as shown by TEM micrograph and selected-area diffraction pattern in the 9Al specimen aged for 1000 min inserted in Figure 3.1. The κ -carbide formation during aging treatment can be found readily in austenitic alloys having high C and Al contents [8-11, 17, 18], including the aged 11Al alloy [14]. Given that the addition of Al or Si leads to an increase of the chemical driving force for κ -carbide precipitation [10, 18], the primary hardening was accelerated in the 9Al-1Si and 11Al alloys.

After aging for 300 min, dramatic secondary hardening occurs in the 11Al alloy with the hardness exceeding 700 HV, while the 9Al and 9Al-1Si alloys show an additional shallow increase of the Vickers hardness after aging up to 10000 min. The microstructures of the aged specimens at which the secondary hardening indicated by red arrows in Figure 3.1 starts are shown in Figures 3.2(d-f). The 9Al and 9Al-1Si specimens aged for 10000 min show colonies of α -ferrite and β -Mn phases formed at the austenite grain boundaries. It had been reported that the similar types of colonies was observed by using SEM and XRD in Fe-31.7Mn-8.9Al-0.74C and Fe-31.6Mn-8.9Al-0.98C alloys aged at 550 °C [17]. The size and number of the colonies are greater in the 9Al-1Si alloy (Figure 3.2(e)) compared to those in the 9Al alloy (Figure 3.2(d)). Meanwhile, in the 11Al specimen aged for 1000 min which is shorter than the 9Al and 9Al-1Si alloys, the β -Mn phase nucleates and grows extensively into the austenite phase with a lath-shaped morphology (Figure 3.2(f)) as shown in a previous study by the current authors [14]. Considering the faster formation kinetics of the β -Mn phase and its lath-type morphology in the 11Al alloy, it is conceivable that the addition of Al increases the driving force for β -Mn formation. Thermodynamic calculation using the commercial software MatCalc with mc_fe2.045 database predicts that the driving force for β -Mn formation, the difference between the free energy of austenite and β -Mn phases, will increase with increasing nominal Al content. Taking the hardness change

and microstructure evolution into account, the secondary hardening behavior of the 11Al alloys can be attributed to formation of the β -Mn phase.

To investigate the redistribution of the alloying elements during the β -Mn formation process, EBSD and EDS measurements were performed for a colony in the 9Al-1Si specimen aged for 10000 min. Figures 3.3(a, b) correspondingly show an SEM micrograph and EBSD phase map of a colony composed of ferrite and β -Mn phases. The microstructure indicates that ferrite has formed along the austenite grain boundary and that the β -Mn phase surrounds the ferrite. Thus, it is conceivable that ferrite nucleates at the austenite boundaries initially, and then β -Mn forms at ferrite/austenite phase boundaries. The EDS elemental profiles along the sky-blue line in Figure 3.3(a) are displayed in Figure 3.3(c). The ferrite grain has relatively high levels of Fe, Al and Si than the other phases, while the Mn content is lower in ferrite. It is conceivable that the ferrite/austenite phase boundaries become more favorable for β -Mn formation due to the higher content of Mn that has migrated from the ferrite region during the ferrite nucleation process. Comparing the austenite and β -Mn, it is clearly observable that the C content in austenite is higher than that in β -Mn, while there is little partitioning of other elements. This partitioning tendency of alloying elements between austenite and β -Mn is identical to that in the 11Al specimen aged for 1000 min, as confirmed by the EPMA analysis in a previous study by the present authors [14].

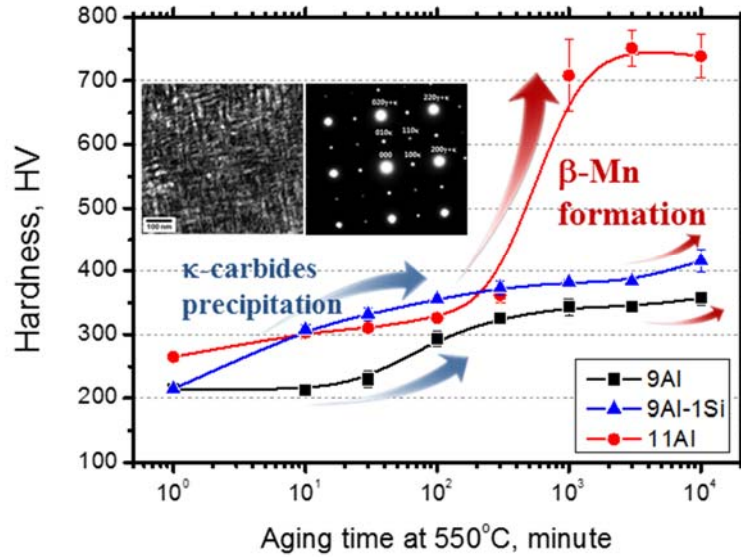


Figure 3.1 Vickers hardness of the 9Al, 9Al-1Si, and 11Al alloys as a function of the aging time at 550 °C. TEM micrograph and selected-area diffraction pattern showing the [001] zone of the κ -carbide in the austenite matrix of the 9Al specimen aged for 1000 min are inserted.

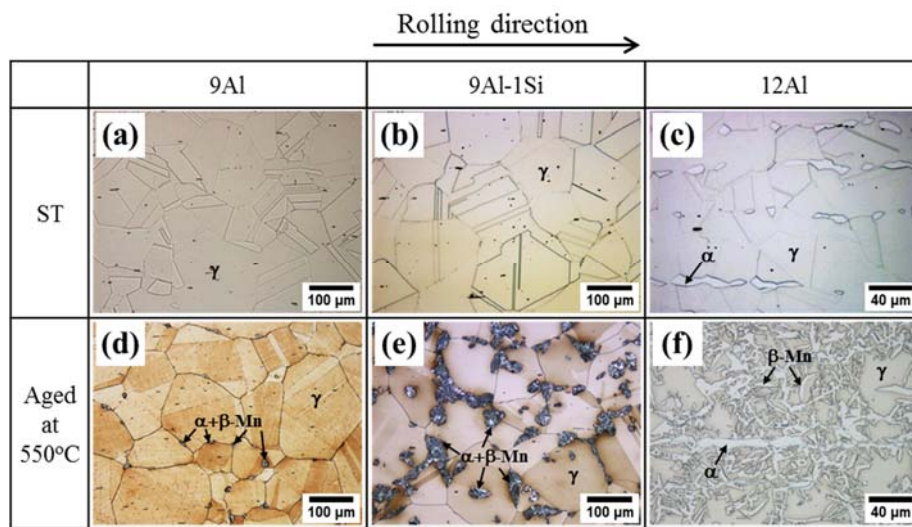


Figure 3.2 Optical micrographs of (a) 9Al ST, (b) 9Al-1Si ST, (c) 11Al ST, (d) 9Al aged for 10000 min, (e) 9Al-1Si aged for 10000 min, and (f) 11Al aged for 1000 min. γ and α represent austenite and ferrite, respectively.

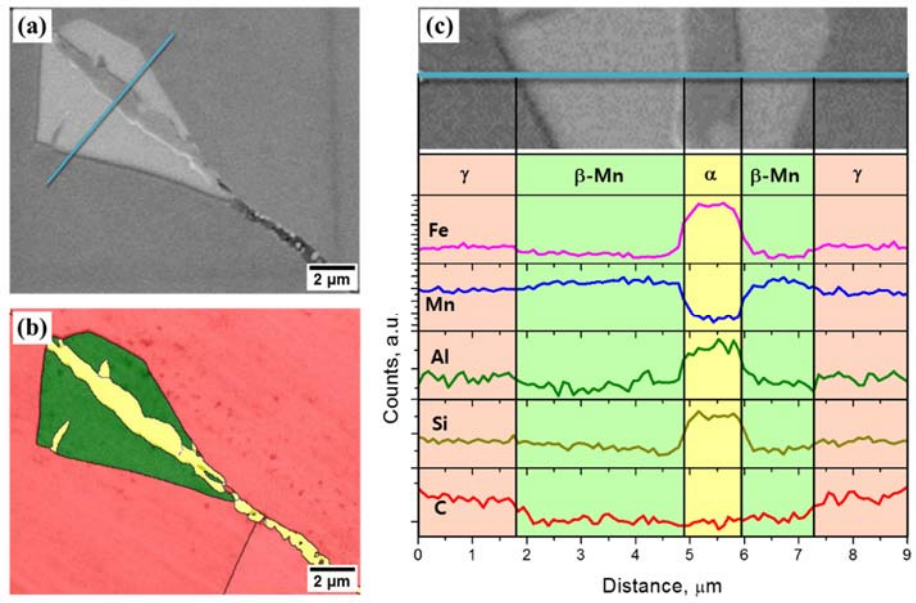


Figure 3.3 (a) SEM micrograph and (b) EBSD phase map (■ FCC; ■ BCC; ■ β-Mn) of the 9Al-1Si aged for 10000 min. (c) EDS elemental profiles of the sky-blue line in (a).

3.4 Tensile and fracture behavior

Yield strength and total elongation of the 9Al, 9Al-1Si, and 11Al alloys obtained from tensile tests are shown in Figure 3.4(a) as a function of aging time at 550 °C. It can be observed that the yield strength of three alloys increases with the increase of aging time due to the formation of κ -carbide. The 9Al-1Si and 11Al alloys show more rapid increase of yield strength than the 9Al alloy. Although the total elongation decreases with increasing aging time, the 9Al and 9Al-1Si alloys have appropriate total elongation over 20% before β -Mn formation occurs at aging time of 10000 min. On the other hand, the total elongation of the 11Al alloy decreases remarkably even before aging time of 300 min at which the β -Mn formation starts, indicated by the red arrow in Figure 3.4(a).

For a detailed analysis of the tensile behavior of the 11Al alloy, Figure 3.4(b) displays the engineering stress-strain curves of the 11Al specimens aged at 550 °C. The ST specimen and aged specimens for 30 and 100 min show yielding and plastic elongation, whereas the specimens aged for 300 and 1000 min show the occurrence of fractures even before the yield point. The ST specimen and aged specimen for 30 min have excellent mechanical properties with tensile strength levels of 876 and 970 MPa and total elongation of 63.4 and 36.4 %, respectively. The specimen aged for 100 min shows a remarkable reduction in its total elongation compared with the specimen aged for 30 min,

while it shows slight increase in the yield and tensile strength. Considering β -Mn phase has not formed at this point, this degradation of the ductility may originate from other factors, except for the β -Mn phase.

To clarify the fracture modes of the 11Al specimens aged at 550 °C correlated with their tensile properties, the fracture surfaces after the tensile test are observed by SEM, with fractographs shown in Figure 3.5. The ST specimen with considerable ductility exhibits dimples on the fracture surface, indicating that the formation and coalescence of micro-voids are the main mechanisms causing the fracture (Figure 3.5(a)). The specimen aged for 100 min shows both a dimpled structure as indicated by the white circles and a smooth surface region that may be former grain or phase boundaries (Figure 3.5(b)). For the specimen aged for 300 min, the fracture surface is composed of smooth surfaces, very similar to typical intergranular fractographs (Figure 3.5(c)). The specimen aged for 1000 min shows smooth surfaces with several fragments on the fracture surface. Considering the fractographs, the fracture of the 11Al alloy changes from the ductile mode to the intergranular or interphase mode according to aging treatment, which may be related to the formation of the β -Mn phase.

Figure 3.6 shows the microstructures of the cross-sectional area near the fracture surface after the tensile test of the 11Al specimens aged at 550 °C. The ST specimen, as shown in Figure 3.6(a), indicates that both austenite and ferrite

grains are uniformly elongated along the loading direction. However, for the specimen aged for 300 min, crack propagation along the austenite grain boundaries and ferrite/austenite phase boundaries can be observed (Figure 3.6(d)). The crack propagation along the boundaries explains the intergranular fracture mode, which can be attributed to the formation of a brittle β -Mn phase at the boundaries, as shown in Figure 3.6(e). For the specimen aged for 100 min, several cracks are observed inside the ferrite band (Figure 3.6(b)) or at the ferrite/austenite phase boundaries (Figure 3.6(c)), as indicated by the white circles. In this specimen, the β -Mn phase has not formed at this point at the boundaries according to the EBSD measurement (Figure 3.6(c)). Note that crack propagation in the ferrite band is arrested at the ferrite/austenite phase boundaries and that some cracks show blunt tips (Figure 3.6(b)). These findings indicate that the austenite can be plastically deformed; however, the ferrite has lost its ductility. A possible explanation for this observation is the ordering of the ferrite phase during the aging treatment. Figure 3.6(f) presents a TEM micrograph and a selected-area diffraction pattern of a ferrite region in the specimen aged for 300 min. The diffraction pattern shows the presence of a $D0_3$ phase with an ordered structure. The $D0_3$ phase is a common ordered phase in Fe-Al- and Fe-Si-based alloys [7, 19-21], as confirmed also in the aged 11Al alloy by XRD [14]. In a study of precipitate growth in ferrite grains, Wu et al. showed that $D0_3$ particles were observed by TEM at an early stage of isothermal

aging at 550 °C in an Fe–28.6Mn–10.1Al–0.46C alloy [19]. Therefore, it is conceivable that the reduced ductility of ferrite phase originates from partial (or full) ordering into the $D0_3$ phase during the aging treatment. Considering the ductility of each phase and the crack propagation behavior in the specimen aged for 100 min, the smooth surface region in Figure 3.5(b) may be a boundary between austenite or ferrite grains or cleavage surfaces formed inside the ferrite grains. The dimpled structure must have formed in ductile austenite grains.

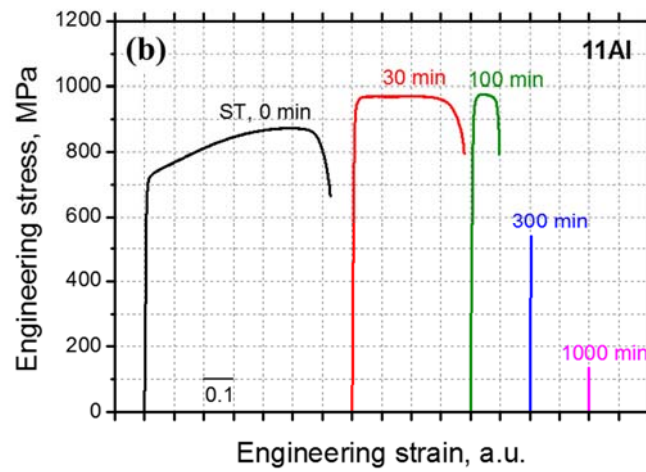
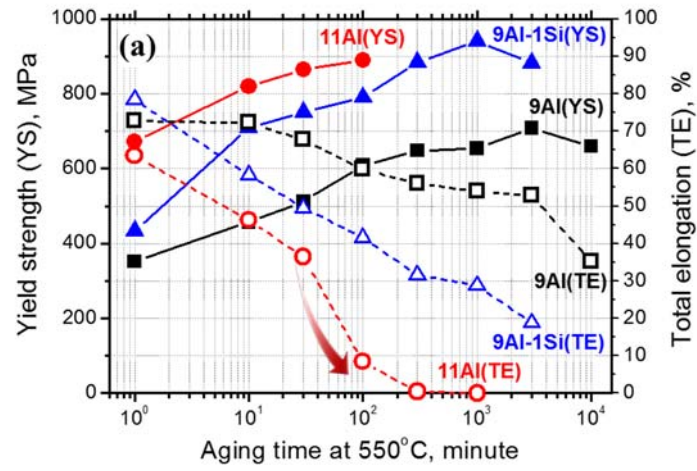


Figure 3.4 (a) Yield strength and total elongation of the 9Al, 9Al-1Si, and 11Al alloys as a function of aging time at 550 °C. (b) Engineering stress-strain curves of the 11Al specimens.

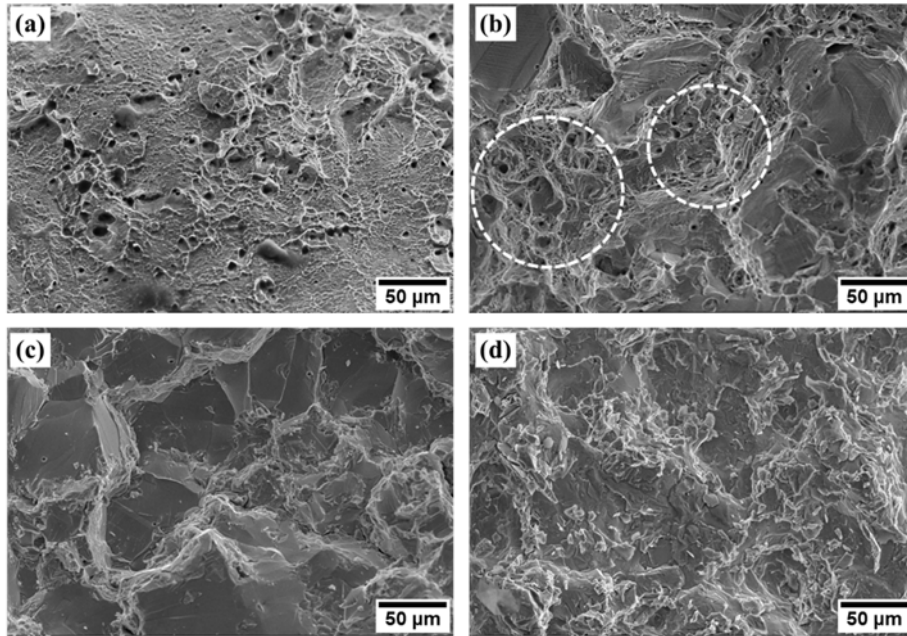


Figure 3.5 SEM fractographs after the tensile test of the 11Al specimens aged at 550 °C for (a) 0 min (ST), (b) 100 min, (c) 300 min, and (d) 1000 min.

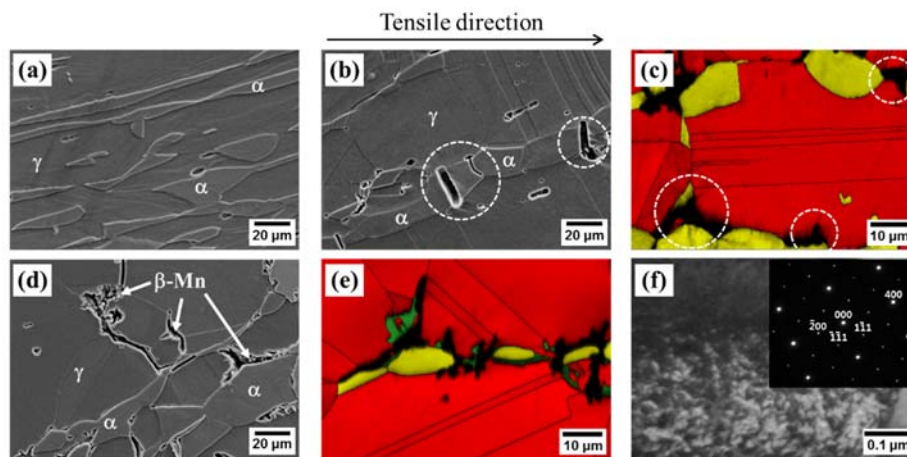


Figure 3.6 SEM micrographs and EBSD phase maps (■ FCC; ■ BCC; ■ β -Mn) near the fracture surface after the tensile test of the 11Al specimens aged at 550 °C for (a) 0 min (ST), (b,c) 100 min, and (d,e) 300 min. γ and α represent the austenite and ferrite, respectively. (f) TEM micrograph and selected-area diffraction pattern showing the [011] zone of the $D0_3$ phase in the ferrite of the specimen aged for 300 min.

3.5 Conclusion: β -Mn formation and aging effect on the fracture behavior

This study investigated the formation behavior of the β -Mn phase in high-Mn low-density steels with different chemical compositions after aging at 550 °C. From the Vickers hardness change and microstructure evolution, the Si and Al additions accelerated the primary hardening induced by κ -carbide precipitation. For 9Al-base alloys, colonies composed of α -ferrite and β -Mn phases were formed along the austenite grain boundaries after aging for 10000 min, and their size and number were greater in the 9Al-1Si alloy than those in the 9Al alloy. For 11Al alloy, the β -Mn phase which led to the dramatic secondary hardening was seen to have a lath-shaped morphology without the co-precipitation of α -ferrite after 1000 min of aging. These morphological and kinetic differences of the β -Mn formation were attributed to the higher Al content, which increased the driving force for β -Mn transformation. In addition, the effects of the aging process on the tensile and fracture behavior were analyzed in the 11Al alloy. A loss of elongation was observed in the specimens aged for 100 min; moreover, they ruptured before the yield point after aging for more than 300 min. The fractography analysis revealed that the β -Mn formation was the main cause of severe ductility loss of the low-density steel. In addition,

the ordering of ferrite into the $D0_3$ phase acted as additional factor of ductility loss especially before the β -Mn formation.

3.6 References

- [1] D.W. Suh, N.J. Kim, *Scripta Materialia*, 68 (2013) 337-338.
- [2] H.K.D.H. Bhadeshia, *Scripta Materialia*, 70 (2014) 12-17.
- [3] S.S. Sohn, B.J. Lee, S. Lee, J.H. Kwak, *Metals and Materials International*, 21 (2015) 43-53.
- [4] S.J. Park, B. Hwang, K.H. Lee, T.H. Lee, D.W. Suh, H.N. Han, *Scripta Materialia*, 68 (2013) 365-369.
- [5] K. Lee, S.J. Park, Y.S. Choi, S.J. Kim, T.H. Lee, K.H. Oh, H.N. Han, *Scripta Materialia*, 69 (2013) 618-621.
- [6] R. Rana, C. Liu, R.K. Ray, *Acta Materialia*, 75 (2014) 227-245.
- [7] Y.U. Heo, Y.Y. Song, S.J. Park, H.K.D.H. Bhadeshia, D.W. Suh, *Metallurgical and Materials Transactions a-Physical Metallurgy and Materials Science*, 43a (2012) 1731-1735.
- [8] G. Frommeyer, U. Brux, *Steel Research International*, 77 (2006) 627-633.
- [9] R.A. Howell, D.C. Van Aken, *Iron Steel Technol*, 6 (2009) 193-212.
- [10] L.N. Bartlett, D.C. Van Aken, J. Medvedeva, D. Isheim, N.I. Medvedeva, K. Song, *Metallurgical and Materials Transactions a-Physical Metallurgy and Materials Science*, 45A (2014) 2421-2435.
- [11] I. Gutierrez-Urrutia, D. Raabe, *Scripta Materialia*, 68 (2013) 343-347.
- [12] K.T. Park, *Scripta Materialia*, 68 (2013) 375-379.
- [13] S.H. Kim, H. Kim, N.J. Kim, *Nature*, 518 (2015) 77-79.

- [14] K. Lee, S.J. Park, J. Lee, J. Moon, J.Y. Kang, D.I. Kim, J.Y. Suh, H.N. Han, *Journal of Alloys and Compounds*, 656 (2016) 805-811.
- [15] S.C. Tjong, *Materials Characterization*, 24 (1990) 275-292.
- [16] C.Y. Chao, C.H. Liu, *Materials Transactions*, 43 (2002) 2635-2642.
- [17] K.H. Han, W.K. Choo, *Metallurgical Transactions a-Physical Metallurgy and Materials Science*, 20 (1989) 205-214.
- [18] K. Sato, K. Tagawa, Y. Inoue, *Metallurgical Transactions a-Physical Metallurgy and Materials Science*, 21 (1990) 5-11.
- [19] C.C. Wu, J.S. Chou, T.F. Liu, *Metallurgical Transactions a-Physical Metallurgy and Materials Science*, 22 (1991) 2265-2276.
- [20] D.G. Morris, S. Gunther, *Acta Materialia*, 44 (1996) 2847-2859.
- [21] D. Ruiz, T.R. Yanez, G.J. Cuello, R.E. Vandenberghe, Y. Houbaert, *Physica B-Condensed Matter*, 385 (2006) 578-580.

Chapter 4

Investigation of the aging behavior and orientation relationships in Fe–31.4Mn–11.4Al–0.89C low-density steel

4.1 Introduction

There are known several crystallographic orientation relationships among constituent phases in steels during phase transformation and precipitation due to thermomechanical processes. Many crystallographic studies on the transformation of steels, where face-centered-cubic (fcc) austenite grains transform to body-centered-cubic (bcc) ferrite, bainite, or martensite phases, have been reported with respect to the Kurdjumov–Sachs (KS) or Nishiyama–Wassermann (NW) relationship [1-6]. In high carbon steels, the Pitsch orientation relationship between cementite precipitate and austenite matrix [7] and the Bagaryatski orientation relationship between cementite precipitate and ferrite matrix [8] were observed at low transformation temperatures. Dyson *et al.* [9] reported the orientation relationship between molybdenum carbide (Mo_2C) precipitate and ferrite matrix, as well as the growth direction of the Mo_2C in tempered molybdenum steels using transmission electron microscopy.

Since these orientation relationships take a crucial part in the microtexture analysis and morphology prediction of the product phases, the study on such crystallographic relationships is necessary to design the microstructure with optimum mechanical properties of advanced high-strength steels.

Recently, low-density steels with outstanding strength and ductility have been developed in which aluminum or silicon is alloyed as a substitutional light element [10-23]. Among those, austenite-based high-Mn steels containing manganese over 15 wt.% and aluminum up to 12 wt.% have attracted increasing attention due to excellent mechanical properties and density reduction rates [14-23]. After aging treatment at appropriate temperature and time, these steels feature micro/nano-scale precipitates, such as κ -carbide [14-18], β -Mn [17, 18, 20-22], and ordered bcc phases (B2 or D0₃) [18, 19, 24] inside austenite matrix or ferrite grains. Because these precipitates have a strong impact on the mechanical behavior of the low-density steels, many studies have been performed in order to investigate their precipitation phenomena and its correlation with the mechanical properties. Especially, the β -Mn phase is known to cause severe ductility loss and brittle fracture in the high-Mn low-density steels, leading to decrease of impact energy [18, 20]. On the formation of the β -Mn during aging treatment of austenite-based high-Mn low-density steels containing 11.4 wt.% Al, K. Lee *et al.* [17] showed that the lath-shaped β -Mn phase were nucleated and extensively grew into austenite matrix. Also

by a TEM study on the aged ferrite-based high-Mn low-density steels, β -Mn grains were formed inside α -ferrite, having a specific crystallographic orientation relationship with α -ferrite matrix [25]. However, it was not reported whether the β -Mn phases have a preferred orientation relationship with the austenite matrix in the high-Mn low-density steels, or not.

In many previous studies where the orientation relationships between two phases were examined, diffraction patterns at interface boundaries from TEM observations were used. Although the TEM analysis offers a closer look on the region of interest at atomic/nano-scale, it lacks statistical verification due to the significant limit of observation area. Meanwhile, as electron backscatter diffraction (EBSD) technique has been improved on both hardware and software systems for nearly two decades, it is now much more reliable in quantitative measurements of local orientations, large numbers of interfaces, and microstructural evolution [26]. With local orientation information from EBSD measurements, local interface orientation relationships between two phases can be analyzed using the orientation relationship stereogram (OR stereogram) [27]. The OR stereogram between two phases is constructed by plotting simultaneously selected low index poles on a stereographic projection using the orientation information across the interfaces between two phases. Then, one can examine the preferred orientation relationship between two phases by analyzing the overlapping set of poles.

In the present research, we investigate the aging behavior and orientation relationships among constitutional phases and precipitates in high Mn low-density steel containing 11.4 wt.% Al. The microstructure evolution and mechanical response during aging treatment are characterized by Vickers hardness measurement combined with microstructural observations from EBSD and TEM. The misorientation-angle distribution, Rodrigues–Frank vector space, and OR stereogram are used to elucidate the orientation relationships across γ -matrix/ β -Mn and β -Mn/ α -precipitate interphase boundaries. The orientation relationships obtained from the OR stereogram analysis are verified by checking the distribution of deviation angle from the predicted ideal orientation relationships, as well as the TEM diffraction patterns at the interface boundaries. In addition, from both orientation relationships for γ -matrix/ β -Mn and β -Mn/ α -precipitate interfaces, the interface character between γ -matrix and α -precipitate is examined and compared to conventional fcc/bcc orientation relationships.

4.2 Materials and methods

4.2.1 Microstructure observation and interface characterization

The specimen solution-treated at 1,050 °C before aging is referred to as ST, and the specimens aged at 550 °C for 1,000 minutes, 10,000 minutes, 30,000 minutes, and 100,000 minutes are referred to as A1K, A10K, A30K, and A100K, respectively [17]. For each specimen, Vickers microhardness was measured on at least 7 points using an 1 kgf load applied for 10 s. Longitudinal plane (i.e, the plane containing rolling and normal directions) of each specimen was prepared for EBSD measurements by mechanical grinding, followed by electropolishing using a solution of 20% perchloric acid, 10% ethylene glycol monobutyl ether, and 70% ethanol.

Before identifying the interphase boundaries from EBSD maps, a grain dilation clean-up process was applied in the TSL-OIM software in order to clean ambiguous or badly-indexed pixel data. Segmentation, smoothing, and extraction of the interphase boundaries from the cleaned EBSD maps were accomplished using 2D boundary segmentation code based on both the marching square algorithm and the feature preserving smoothing algorithm, which was originally developed to analyze the heterophase interface character of Cu-Nb multilayer composites [5]. From the approximated boundary geometry together with neighboring phase and orientation data, the

misorientation-angle distribution, and Rodrigues–Frank vector space [28, 29] were calculated for γ -matrix/ β -Mn, β -Mn/ α -precipitate, and γ -matrix/ α -precipitate interphase boundaries, respectively. To investigate the local interface orientation relationships of γ -matrix/ β -Mn and β -Mn/ α -precipitate boundaries, the OR stereogram was constructed for two phases by plotting low index poles such as 100, 110, 111, 112, 012 and 122 families on a stereographic projection. The sample coordinate system of the EBSD measurements was taken as the reference frame of the OR stereogram [27]. If there are coincident poles of the two phases on the OR stereogram, this means there exists a specific orientation relationship between them. We selected five pairs of two points, which are adjacent across the interphase boundary, having strong peaks in the misorientation-angle distribution and Rodrigues–Frank vector space. Euler angles (φ_1 , Φ , φ_2) at each point of two grains/phases across interphase boundaries were obtained from EBSD maps and then used to draw the OR stereogram.

TEM characterizations were carried out to analyze the ordering of matrix phase and orientation relationships in the A30K specimen. In particular, in order to confirm the orientation relationships obtained from the OR stereogram practice, the FIB milling was conducted on the γ -matrix/ β -Mn and β -Mn/ α -precipitate phase boundary regions to be examined under TEM. For 3D EBSD analysis, mechanical serial sectioning based on repetitive chemical-mechanical

polishing was introduced on the AlK specimen with an automatic polisher. Four microhardness indents were made on the specimen for indicating the region of interest ($\sim 79 \times 79 \mu\text{m}^2$) and measuring the thickness of a removed layer during serial sectioning. The specimen for 3D EBSD analysis was polished with a colloidal silica suspension in every cycle of polish. The removal depth at each step was obtained by means of confocal microscopy measuring surface profiles of the microhardness indents. We collected 70 parallel layers, each separated by $0.34 \pm 0.08 \mu\text{m}$, which is almost same with EBSD step size of $0.3 \mu\text{m}$.

4.2.2 Calculation of the deviation angle from the ideal orientation relationship

In order to verify statistically the orientation relationships obtained from the OR stereograms, the distributions of deviation angle from the ideal orientation relationship were calculated from the interface segmentation data. The deviation angle is calculated as follows. The orientation matrices of the parent and daughter phases (g_p and g_d , respectively) across the interface segments are determined from the Euler angles. Given g_p and g_d , the measured misorientation matrix (M_{meas}) between the parent and daughter phases is calculated as

$$M_{\text{meas}} = g_d \cdot g_p^{-1} \quad (1)$$

Likewise, the ideal misorientation matrix (M_{ideal}) is defined based on theoretical orientation relationship obtained from the OR stereograms. Then, the deviation matrix (D) between the ideal and measured misorientation matrix is derived as:

$$D_{i,j} = M_{\text{ideal}} \cdot O_i \cdot M_{\text{meas}}^{-1} \cdot O_j \quad (2)$$

Here, O_i and O_j are the symmetry operator for cubic crystals, which is taken from the set of 24 elements ($i, j = 1, \dots, 24$). The deviation angle for each deviation matrix is calculated, and the smallest is chosen as the deviation angle from the ideal orientation relationships.

$$\theta = \min \left\{ \cos^{-1} \left[\frac{S(D_{i,j}) - 1}{2} \right] \right\} \quad (3)$$

$$S(D) = D_{11} + D_{22} + D_{33} \quad (4)$$

Then, the distributions of deviation angle were computed from the segmentation data of the interphase boundaries.

In addition, the distributions of deviation angle for randomly oriented pairs were calculated for comparison with the measured interface segments. The randomly oriented pairs were generated by partitioning the Euler space of misorientation matrix into a finite number of elements of equal volume, based on following equation [30, 31]:

$$dg = \frac{1}{8\pi^2} \sin \Phi d\varphi_1 d\Phi d\varphi_2 \quad (5)$$

where dg is the misorientation elements in the Euler space, $\frac{1}{8\pi^2}$ is the

normalization factor, and $\sin\Phi$ is an invariant measure which remains the volume of each element unchanged after an arbitrary transformation. Considering the symmetry of cubic structure, the misorientation parameters represented by the Euler angles range from zero to 90° for φ_1 , Φ , and φ_2 , respectively. With a resolution of 2° , 91,125 random pairs were obtained for calculation.

4.3 Microstructural evolution and aging behavior

To identify equilibrium phases of the investigated alloy as a function of temperature, the equilibrium phase fractions were calculated using phase diagram (CALPHAD) method [32]. The thermodynamic database for high Mn-high Al steels based on Fe–Mn–Al–C quaternary system was used for calculation [33]. Figure 4.1 shows the volume fractions of equilibrium phases in Fe–30Mn–12Al–0.9C alloy. The alloy presents two-phase region consisting of austenite and ferrite at 1,200 °C. As the temperature goes down from about 1,050 °C, the fraction of austenite decreases abruptly, while the amount of ferrite increases rapidly and κ -carbide starts to precipitate. At 800 °C, the β -Mn phase begins to precipitate and its fraction increases monotonically up to about 46.5% at 500 °C, while ferrite phase starts to disappear. Since the aging treatment was conducted at 550 °C, it is estimated from the equilibrium phase diagram that κ -carbide and β -Mn are formed within the matrix phase during aging process.

EBSD phase maps of the ST, A1K, A10K, and A100K specimens are shown in Fig. 4.2(a-e), respectively. The ST specimen consists of a γ -austenite matrix with some α -ferrite grains elongated along the rolling direction. The phase fraction of these α -ferrite bands is 10.0%, measured from EBSD. The amount of the α -ferrite bands from the EBSD measurement is much lower than the calculated fraction (\sim 42.8%) at around 1,050 °C in Fig. 4.1. The β -Mn

phase, colored in green in Fig. 4.2(b-e), has grown extensively into the γ -matrix after aging for 1,000 min. In order to analyze the morphology of the β -Mn, 3D EBSD microstructure from the A1000 specimen was obtained by the mechanical serial sectioning, and it is shown in Fig. 4.3. 3D reconstruction process and morphology analysis were applied in the DREAM.3D software [34]. It is assumed that all grains including 94 β -Mn grains in 3D representative volume elements (RVE) have the morphology as ellipsoid. Under this assumption, the principal axis and their length of “best fit” β -Mn ellipsoids were calculated. Figure 4.4 shows distribution of β -Mn plate lengths, and plots of width against length and thickness against length of β -Mn plates. Also, the principal axis length and aspect ratios of the 94 β -Mn grains are listed in Table 4.1. Considering the aspect ratios, which are 2.3 and 5.2 for Length/Width and Length/Thickness, respectively, the β -Mn grains are formed in the γ -matrix with a lath- or plate-type morphology.

After β -Mn phase forms, a new microscopic bcc phase was precipitated inside and at grain/phase boundaries of the β -Mn phase by further aging treatment, as shown in the magnified EBSD phase maps in Fig. 4.2(d,e). These small-sized precipitates are considered to be the ordered bcc phase (B2 or D0₃) due to high Al content in the investigated alloy [18, 19, 24]. The microstructural evolution and precipitation behavior during the aging treatment of this alloy are different from the austenitic alloys containing about 9 wt.% Al, in which co-

precipitation of β -Mn and α -ferrite forms a lamellar-type morphology along γ -austenite grain boundaries [21, 22]. The kinetics and morphological differences of the β -Mn and α -ferrite precipitation in two alloy systems are due to the difference in Al content, such that higher Al content increases the driving force for the β -Mn formation, as verified by thermodynamic calculation in a previous study by the present authors [18].

Figure 4.2(f) shows the Vickers hardness on all specimens as a function of the aging time at 550 °C. At the incipient stage of the aging treatment within 300 min, the gradual increase of the Vickers hardness is observed, indicating the primary age hardening by the formation of the nano-sized κ -carbide within the γ -matrix, as previously confirmed by TEM observation [17]. After aging for 300 min, a dramatic increase in hardness up to 700 HV is found. This secondary hardening behavior is due to the formation of the β -Mn phase, as clearly noticed from microstructural evolution in Fig. 4.2(b). After aging for 10,000 min, the Vickers hardness is maintained without considerable changes.

In order to confirm the crystal structure and ordering of nano-sized precipitates in matrix phase, TEM characterizations were carried out on the A30K specimen. Figures 4.5(a-b) show a bright-field image and a selected area diffraction pattern along [011] zone of the austenite matrix. As mentioned earlier, fine coherent κ -carbides are formed within γ -austenite grains, indicated by superlattice {100} and {110} reflections. Again, this κ -carbide precipitation

seems to occur at the early stage of the aging treatment as indicated by the age hardening in Fig. 4.2(f). A TEM micrograph and a selected-area diffraction pattern of an α -precipitate region inside the β -Mn grains are presented in Fig 4.5(c-d). The diffraction pattern indicates the presence of partial $D0_3$ order inside the α -precipitate, as usually observed in ferritic alloys having high Al or Si contents [18, 24].

The previous study [17] reported that interstitial carbon atoms merely diffused from β -Mn into γ -matrix during the β -Mn formation, while the other substitutional elements such as Al, Mn and Fe showed little partitioning between the β -Mn and γ -matrix. In contrast, during the formation of the α -precipitate at the β -Mn interior or grain/phase boundary, the redistribution of substitutional elements is required. Therefore, together with the current observations on microstructural evolution, the precipitation sequence in the investigated alloy is γ -matrix \rightarrow β -Mn \rightarrow α -precipitate and can be explained by the redistribution of the alloying elements in addition to the increase of the driving force for the β -Mn formation due to the higher Al content. For convenience, from now on, the austenite matrix containing nano-sized coherent κ -carbides is referred to as “ γ -matrix”, and the bcc precipitate phase including both a disordered bcc (A2) and an ordered $D0_3$ is referred to as “ α -precipitate”.

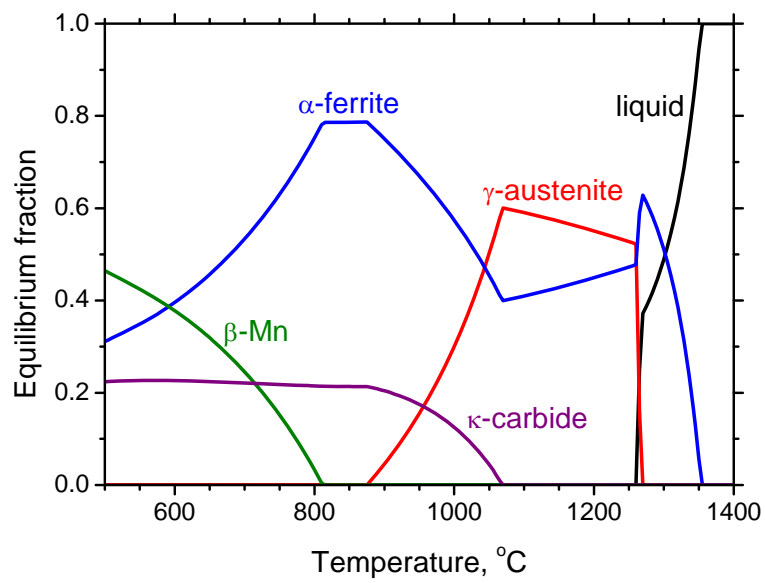


Figure 4.1 The equilibrium phase fractions as a function of temperature of Fe–30Mn–12Al–0.9C alloy, calculated with CALPHAD method.

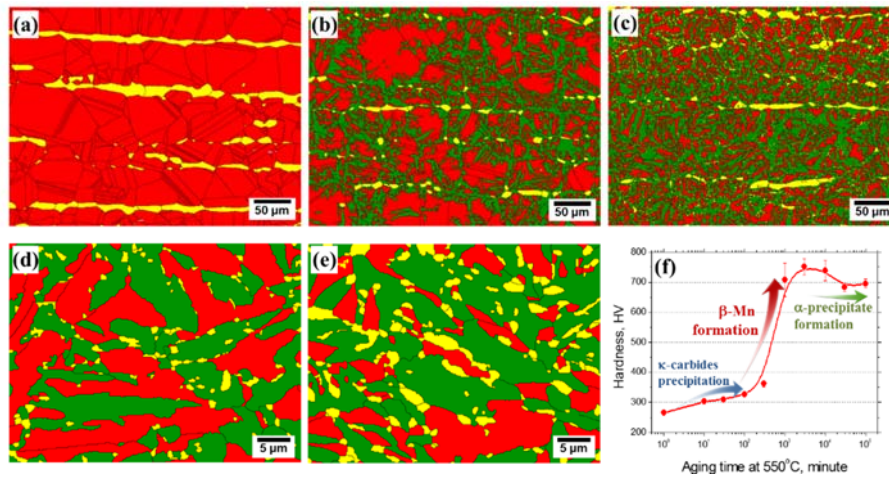


Figure 4.2 EBSD phase maps: (a) as solution treated; after aging at 550 °C for (b) 1,000 mins.; (c, d) 10,000 mins., and; (e) 100,000 mins. (■ FCC; ■ BCC; ■ β-Mn). The horizontal direction is a rolling direction of the specimen. (d, e) are the locally magnified phase maps representing the precipitation of microscopic ordered bcc phases inside the β-Mn grains. (f) Vickers hardness of as a function of aging time.

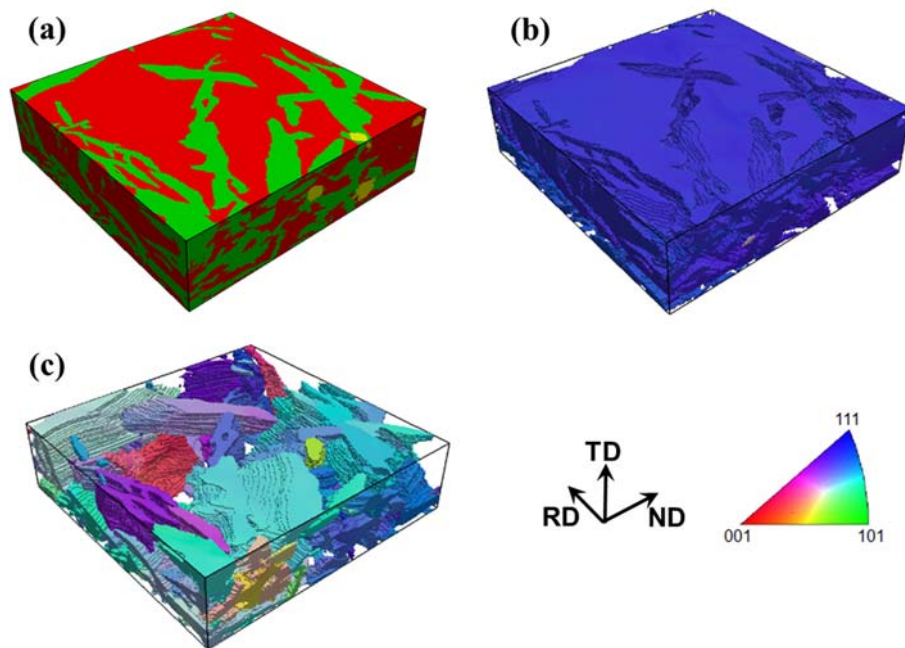


Figure 4.3 3D-reconstructed EBSD microstructure after aging at 550 °C for 1,000 mins: (a) Phase map (■ FCC; ■ BCC; ■ β -Mn), (b) Austenite orientation (TD) map, (c) β -Mn orientation (TD) map.

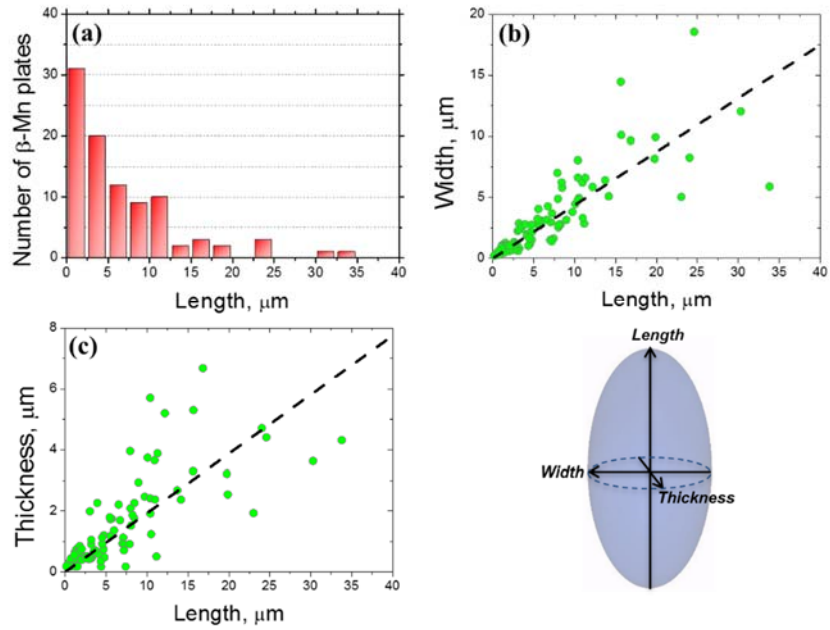


Figure 4.4 (a) Distribution of β -Mn plate lengths from 3D EBSD RVE in Fig. 4.3, assuming the β -Mn morphology as an ellipsoid. Plots of (b) width against length, and (c) thickness against length of β -Mn plates.

Table 4.1 The principal axis length and aspect ratios of the 94 β -Mn grains from 3D RVE.

	Value
Length (μm)	6.7 ± 1.3
Width (μm)	3.1 ± 0.6
Thickness (μm)	1.5 ± 0.3
Length/Width	2.3
Length/ Thickness	5.2

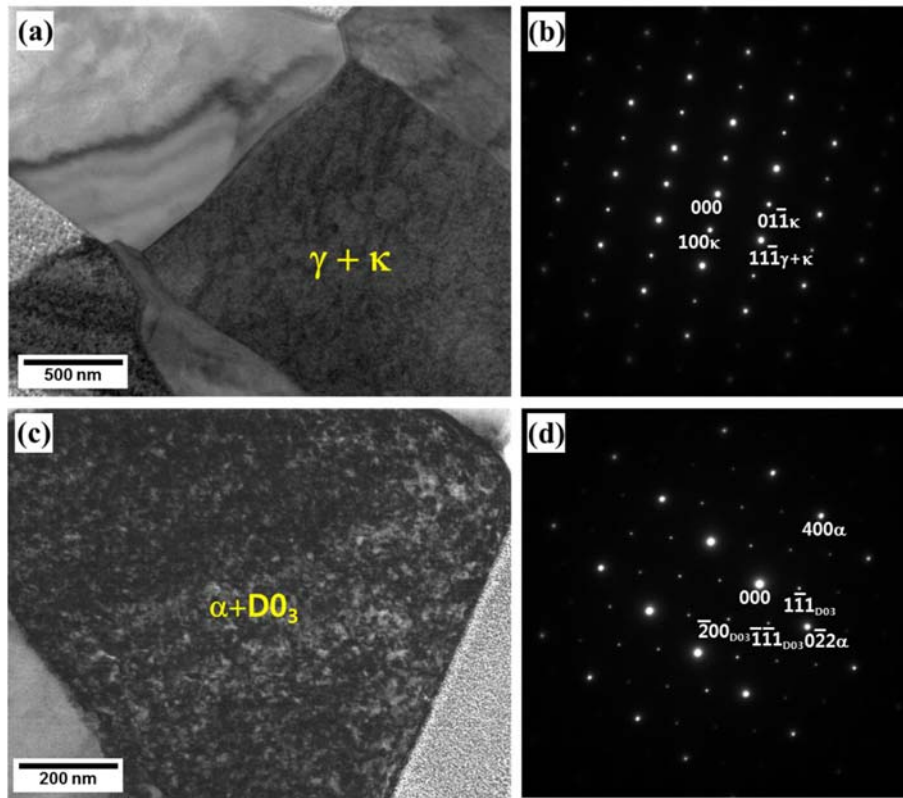


Figure 4.5 TEM micrographs and diffraction patterns after aging at 550 °C for 30,000 mins. (a) Bright-field image and (b) selected area diffraction pattern showing [011] zone of the γ -austenite and κ -carbide. (c) Bright-field image and (d) selected area diffraction pattern showing [011] zone of the α -precipitate including partial $D0_3$ order.

4.4 Orientation relationship between γ -matrix and β -Mn

Figure 4.6 shows the magnified EBSD maps of phase, orientation (transverse direction, TD), and image quality (IQ) of the A1K specimen, in which the β -Mn grows sufficiently into the γ -matrix. Some small-sized α -precipitates, colored in yellow in phase map, are observed in the interior or at the grain/phase boundaries of β -Mn. The misorientation-angle distribution of γ -matrix/ β -Mn interphase boundaries is presented in Fig. 4.7(a) and compared with the Mackenzie distribution [35]. Note that a relatively large fraction of misorientations ranging between 17° and 21° shows up, and the corresponding γ -matrix/ β -Mn interphase boundaries are colored in red in Fig. 4.6(c). Figure 4.7(b) shows the Rodrigues–Frank vector space $\mathbf{R}(R_1, R_2, R_3)$ for γ -matrix/ β -Mn interphase boundaries. The space is represented as a series of $R_1 \times R_2$ sections at different R_3 (from the bottom “section a at $R_3 = 0.000$ ” to the top “section g at $R_3 = 0.315$ ”) of two different phases having cubic crystal structures [29]. It is found that the γ -matrix/ β -Mn interphase boundaries have strong peaks at around $\mathbf{R} = (0.157, 0.033, 0.033)$ and $\mathbf{R} = (0.033, 0.157, 0.033)$, as indicated by white arrows in Fig. 4.7(b). These are equivalent to the strong peaks found in the misorientation-angle distribution, signifying that a stable preferred orientation relationship exists between γ -matrix and β -Mn phase.

To determine the γ -matrix/ β -Mn orientation relationship, five different

regions having misorientation angles from 17° to 21° are selected as marked in Fig. 4.6 and the corresponding OR stereograms are shown in Fig. 4.8(a-e), respectively. It is apparent that coincidence of {111} γ -matrix and {122} β -Mn poles is found for all cases. Perpendicular to this coincident poles, another overlapping pair of coincidence poles is found for all cases indicating consistently {110} γ -matrix // {012} β -Mn. Thus, the γ -matrix/ β -Mn orientation relationship obtained by the OR stereograms is summarized as follows:

$$(111)_{\gamma} // (221)_{\beta\text{-Mn}}, (01\bar{1})_{\gamma} // (01\bar{2})_{\beta\text{-Mn}}, (\bar{2}11)_{\gamma} // (\bar{5}42)_{\beta\text{-Mn}} \quad (6)$$

and the equivalent axis-angle pair of this relationship is calculated to be $\langle 3.12.2 \ 10.6 \rangle / 19.6^{\circ}$, which characterizes the peaks in the misorientation-angle distribution and in the Rodrigues–Frank vector space in Fig. 4.7.

For further quantification of the γ -matrix/ β -Mn interface characteristics, the distributions of deviation angle from the ideal orientation relationship obtained by the OR stereograms were calculated from the segmentation data of the γ -matrix/ β -Mn interphase boundaries in Fig. 4.6, and the results are shown in Fig. 4.8(f). Also, the distribution of deviation angles for randomly oriented pairs of γ -matrix and β -Mn grains is presented in black line in the figure. It is clearly seen that nearly 40% of the interface segments are within 5° of deviation

from the ideal orientation relationship, implying that the majority of the β -Mn grains have the orientation relationship with γ -matrix as predicted by the OR stereograms. In addition, TEM observations were conducted on the A30K specimen with respect to the γ -matrix/ β -Mn phase boundary, in order to clarify the orientation relationship. Figure 4.9 shows a bright-field image and a selected area diffraction pattern of circular area in Fig. 4.9(a). The [011] zone axis of the γ -austenite and κ -carbide matches well with the [012] zone of the β -Mn phase, which shows the same pair of coincident poles in the orientation relationship. Further, the selected area diffraction pattern exhibits a coincidence of $\{111\}_{\gamma+\kappa}$ and $\{221\}_{\beta\text{-Mn}}$ reflections, indicating another predicted pair in the orientation relationship. Therefore, one can confirm that the preferred orientation relationship is found between γ -matrix and β -Mn phases as in equation 6.

The previous study [5] reported that the $\{111\}_{\text{fcc}}$ has the lowest free surface energies for fcc crystal, which was verified by using the nearest neighbor broken bond model. Similarly, assuming that the $\{111\}$ γ -matrix plane has the lowest energies for the γ -matrix in the investigated alloy, $\{111\}_{\gamma} // \{221\}_{\beta\text{-Mn}}$ interface might be a possible habit plane having the preferred orientation relationship. To confirm the coherency of the $\{111\}_{\gamma} // \{221\}_{\beta\text{-Mn}}$ interface, the atom arrays between $\{111\}_{\gamma}$ and $\{221\}_{\beta\text{-Mn}}$ planes are overlaid and presented in Fig. 4.10. The lattice parameters of γ -matrix and β -Mn were 3.761 and 6.310

Å, respectively, based on X-ray diffraction measurements on the A10K specimen [17]. The coherent matching between $\{111\}_\gamma$ and $\{221\}_{\beta\text{-Mn}}$ planes is observed on the region surrounded by blue dashed line. Surprisingly, the coincident area is quite small compared to overall boundaries presented in the figure. However, the fraction of coherent region is known to be increased by introducing crystal defects such as misfit dislocations and ledges around the “real” interface [36]. Thus, it is reasonable to conclude that the γ -matrix/ β -Mn interface with the predicted orientation relationship is dominant in the investigated alloy.

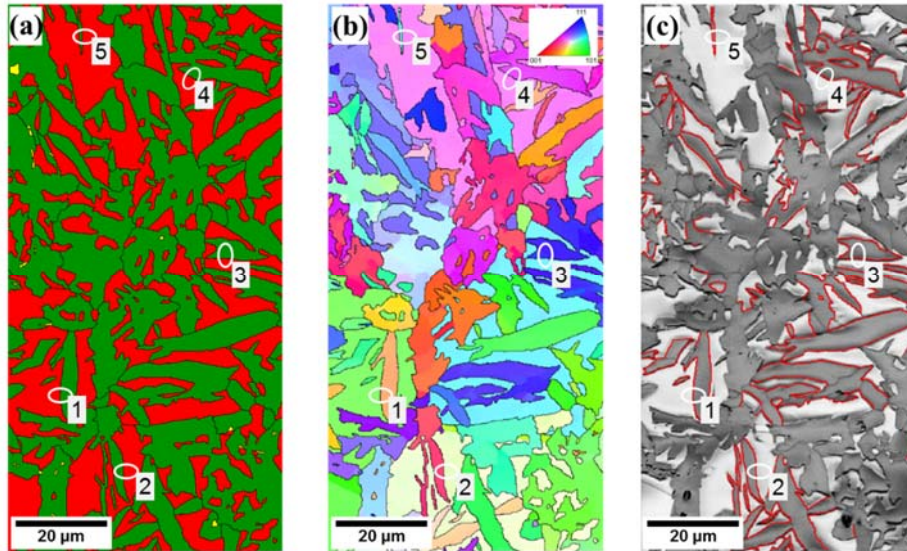


Figure 4.6 Microstructure after aging at 550 °C for 1,000 mins.: (a) EBSD phase map (■ FCC; ■ BCC; ■ β-Mn), (b) Orientation (TD) map, (c) IQ map highlighting misorientation angles for γ -matrix/ β -Mn interphase boundaries in the range $17^\circ < \text{red} < 21^\circ$, which corresponds to the dominant orientation relationship (see next figure). The horizontal direction is a normal direction of the specimen.

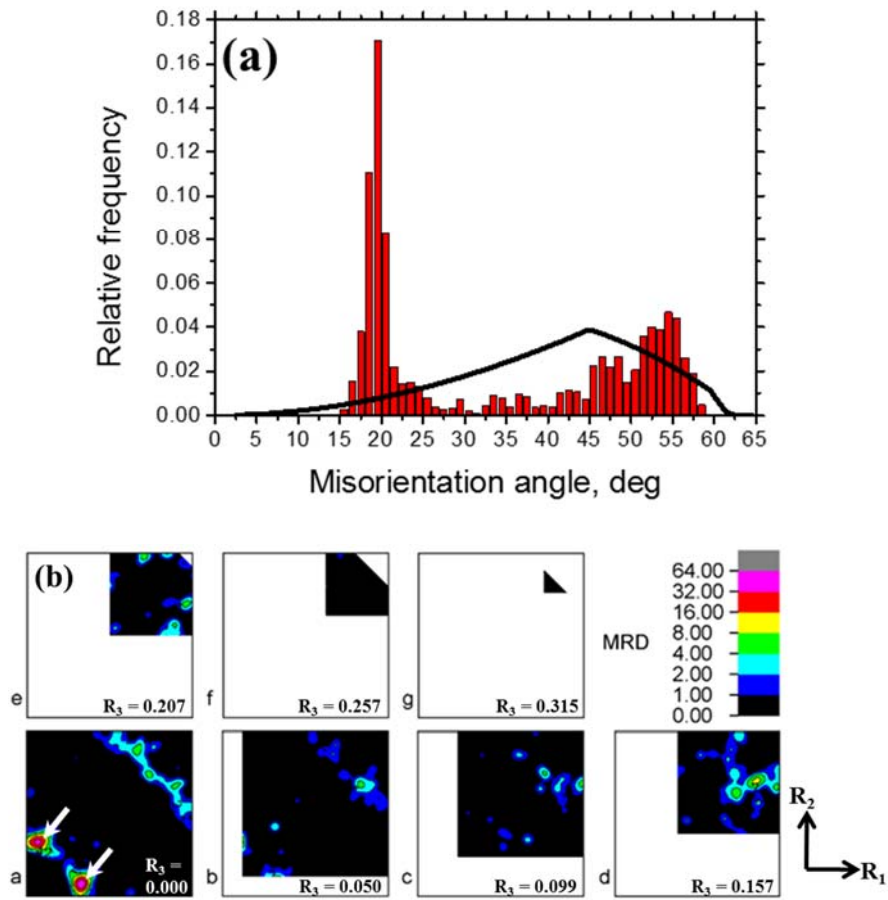


Figure 4.7 (a) Misorientation-angle distribution and (b) Rodrigues–Frank vector space $\mathbf{R}(R_1, R_2, R_3)$ for γ -matrix/ β -Mn interphase boundaries from EBSD measurements in Fig. 4.6. The black curve in (a) indicates the MacKenzie distribution.

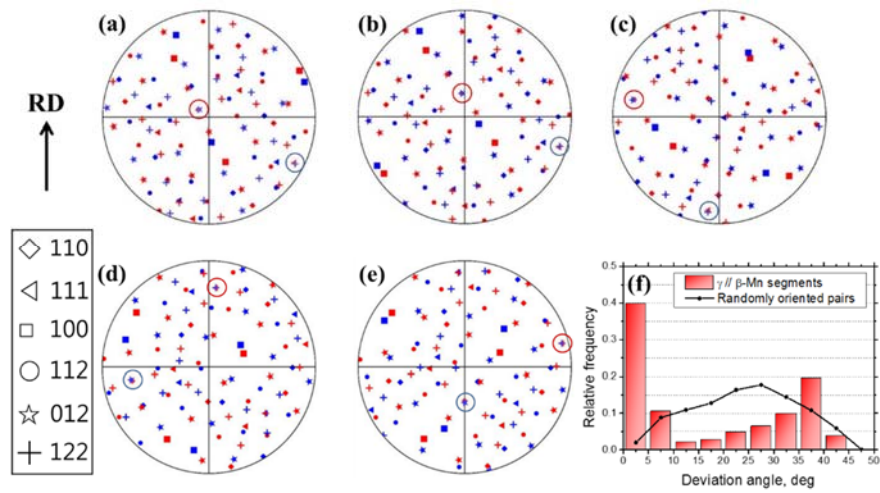


Figure 4.8 Overlaid pole figures showing the orientation relationship for (a) region 1, (b) region 2, (c) region 3, (d) region 4, and (e) region 5 in Fig. 4.6(a) (γ -matrix poles in red, β -Mn poles in blue); the common interface normal is identified as well as the common direction located in the zone of the normal (dashed great circle) i.e. the trace of the interface plane. (f) Distributions of the deviation angle of γ -matrix/ β -Mn phase boundary segments from ideal γ -matrix/ β -Mn relationship. The black line in (f) indicates the distribution of deviation angles based on randomly oriented pairs of points in γ -matrix and β -Mn.

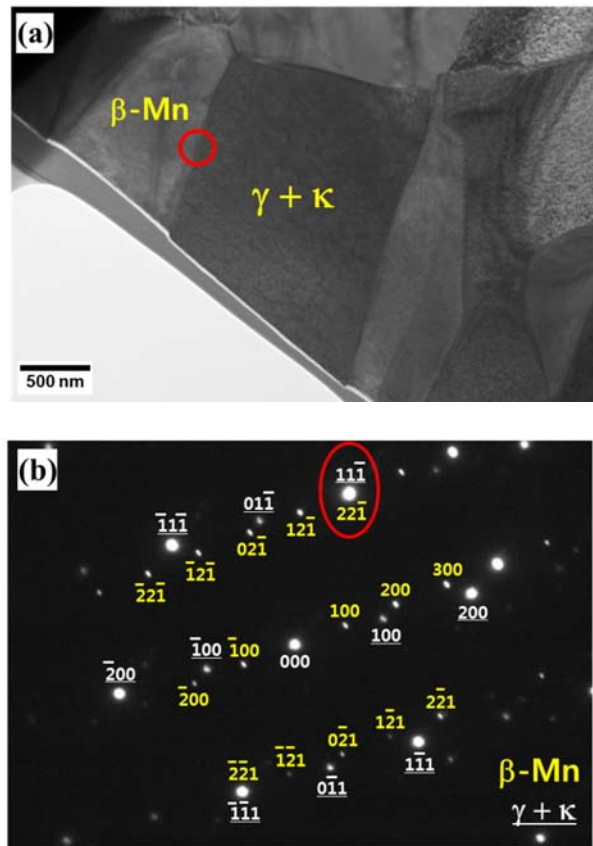


Figure 4.9 TEM micrographs and diffraction patterns at the γ -matrix/ β -Mn interphase boundaries after aging at 550 °C for 30,000 mins. (a) Bright-field image and (b) selected area diffraction pattern showing [011] zone of the γ -austenite and κ -carbide and [012] zone of the β -Mn phase, showing overlapped 111 γ -matrix and 221 β -Mn poles.

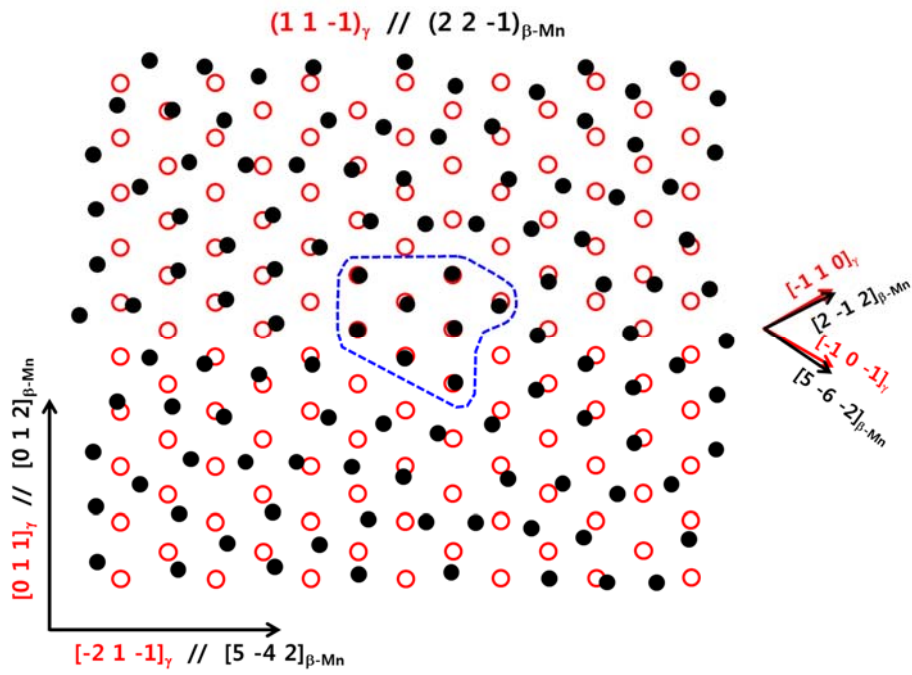


Figure 4.10 Crystallographic atom arrays at the interface between $\{111\}$ plane of the γ -matrix and $\{221\}$ plane of the β -Mn phase.

4.5 Orientation relationship between β -Mn and α -precipitate

On the orientation relationship between α -ferrite matrix and β -Mn precipitate, Liu *et al* [25] showed that the orientation relationship was $(001)_{\alpha\text{-ferrite}} // (012)_{\beta\text{-Mn}}$, $(010)_{\alpha\text{-ferrite}} // (02\bar{1})_{\beta\text{-Mn}}$, $(100)_{\alpha\text{-ferrite}} // (100)_{\beta\text{-Mn}}$ in a Fe–29.9Mn–9.1Al–2.9Cr ferritic alloy by TEM observation. In addition, Baker *et al* [37] reported that the identical orientation relationship was observed between B2 matrix and β -Mn precipitates in a bcc-based, spinodally formed $\text{Fe}_{35}\text{Ni}_{15}\text{Mn}_{25}\text{Al}_{25}$ (in at. %) alloy. While the β -Mn was precipitated within α -ferrite or B2 matrix in the case of both the bcc-based alloys, on the contrary, the α -precipitates were formed at the β -Mn interior or grain/phase boundary in the currently investigated alloy after aging for 10,000 min, as shown in Fig. 4.2. To identify the β -Mn/ α -precipitate orientation relationship, EBSD and TEM measurements were conducted on the A30K specimen, again.

The magnified EBSD maps of phase, TD orientation, and IQ of the A30K specimen are shown in Fig. 4.11. Compared to the A1K specimen exhibited in Fig. 4.6, the α -precipitates grow inside β -Mn grains after further aging treatment. Interestingly, preferred orientation of the α -precipitates was fairly observed depending on each β -Mn parent grain. Figure 4.12(a) shows the misorientation-angle distribution of β -Mn/ α -precipitate interphase boundaries

with the Mackenzie distribution. It is apparently seen that higher frequencies of the interphase boundaries are distributed to the range between 24° and 28° , which are colored in red in Fig. 4.11(c). Figure 4.12(b) exhibits the Rodrigues–Frank vector space $\mathbf{R}(R_1, R_2, R_3)$ for β -Mn/ α -precipitate interphase boundaries. The strong peaks are found at around $\mathbf{R} = (0.232, 0, 0)$ and $\mathbf{R} = (0, 0.232, 0)$, indicated by white arrows in Fig. 4.12(b). It is equivalent to a $\langle 1\ 0\ 0 \rangle / 26.6^\circ$ in the axis–angle pair convention, which corresponds to the axis-angle description of the orientation relationship between bcc matrix and β -Mn precipitate as confirmed by the previous studies [25, 37]. Thus, it seems that the β -Mn grain and α -precipitate in the investigated alloy can have the same orientation relationship as observed in both the bcc-based alloys.

Figures 4.13(a-e) show the OR stereograms for β -Mn/ α -precipitate interphase boundaries in the A30K specimen. Five different regions having the misorientation angles between 24° and 28° are selected as marked in Fig. 4.11. The overlap of $\{012\}$ β -Mn and $\{001\}$ α -precipitate poles appears for all cases. Perpendicular to this coincident poles, another pair of $\{012\}$ β -Mn and $\{001\}$ α -precipitate poles is overlapped, and further, $\{001\}$ pole in β -Mn coincides with $\{001\}$ pole in α -precipitate for all cases. Therefore, the orientation relationship between β -Mn phase and α -precipitate obtained by the OR stereograms is summarized as follows:

$$(012)_{\beta\text{-Mn}} // (001)_{\alpha}, (02\bar{1})_{\beta\text{-Mn}} // (010)_{\alpha}, (100)_{\beta\text{-Mn}} // (100)_{\alpha} \quad (7)$$

and this is identical orientation relationship as observed in ferritic [25] and bcc-based spinodally formed alloy [37].

Figure 4.13(f) presents the distributions of deviation angle from the ideal $\beta\text{-Mn}/\alpha$ -precipitate orientation relationship obtained by the OR stereograms. The deviation angles were calculated from the segmentation data of the $\beta\text{-Mn}/\alpha$ -precipitate interphase boundaries. Compared the distribution of deviation angles for randomly oriented pairs, the low deviation angle section below 5° has a relatively large fraction. Therefore, it is conceivable that the orientation relationship predicted by the OR stereograms is valid for the $\beta\text{-Mn}/\alpha$ -precipitate interphase boundaries from a quantitative aspect. TEM characterizations were also carried out on $\beta\text{-Mn}/\alpha$ -precipitate phase boundary in the A30K specimen. Figure 4.14 shows a TEM micrograph and a selected area diffraction pattern of circular area in Fig. 4.14(a). The α -precipitate [001] zone axis coincides with the $\beta\text{-Mn}$ [012] zone axis. These coincident zone axes correspond to a pair of coincident poles in the orientation relationship. On the selected area diffraction pattern, $\{021\}_{\beta\text{-Mn}}$ reflections are consistent with $\{020\}_{\alpha+\text{D03}}$ reflections. Furthermore, a coincidence of $\{200\}_{\beta\text{-Mn}}$ and $\{200\}_{\alpha+\text{D03}}$ reflections are observed on diffraction pattern. Therefore, it is certainly proved

that the preferred orientation relationship between β -Mn and α -precipitate phases exists in the investigated alloy as in equation 7.

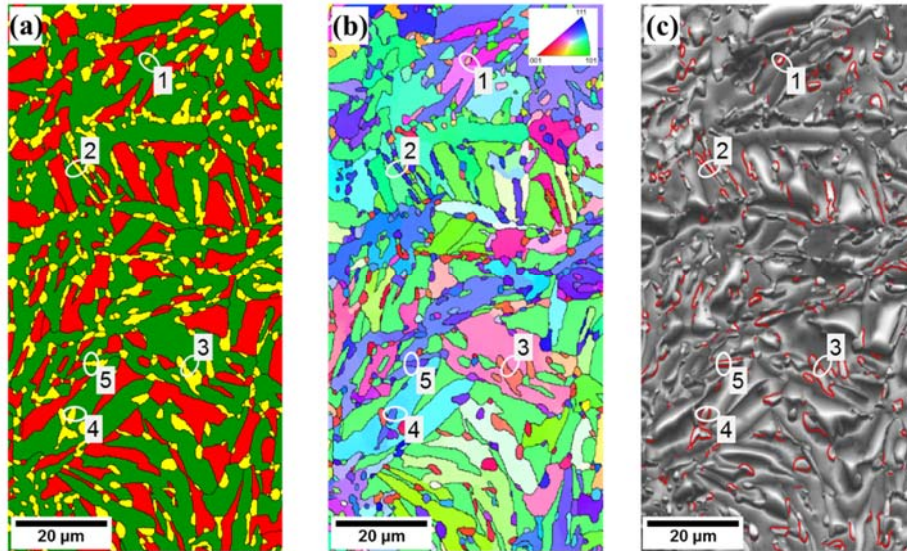


Figure 4.11 Microstructure after aging at 550 °C for 30,000 mins.: (a) EBSD phase map (■ FCC; ■ BCC; ■ β -Mn), (b) Orientation (TD) map, (c) IQ map highlighting misorientation angles for β -Mn/ α -precipitate interphase boundaries in the range $24^\circ < \text{red} < 28^\circ$, which corresponds to the dominant orientation relationship (see next figure). The horizontal direction is a normal direction of the specimen.

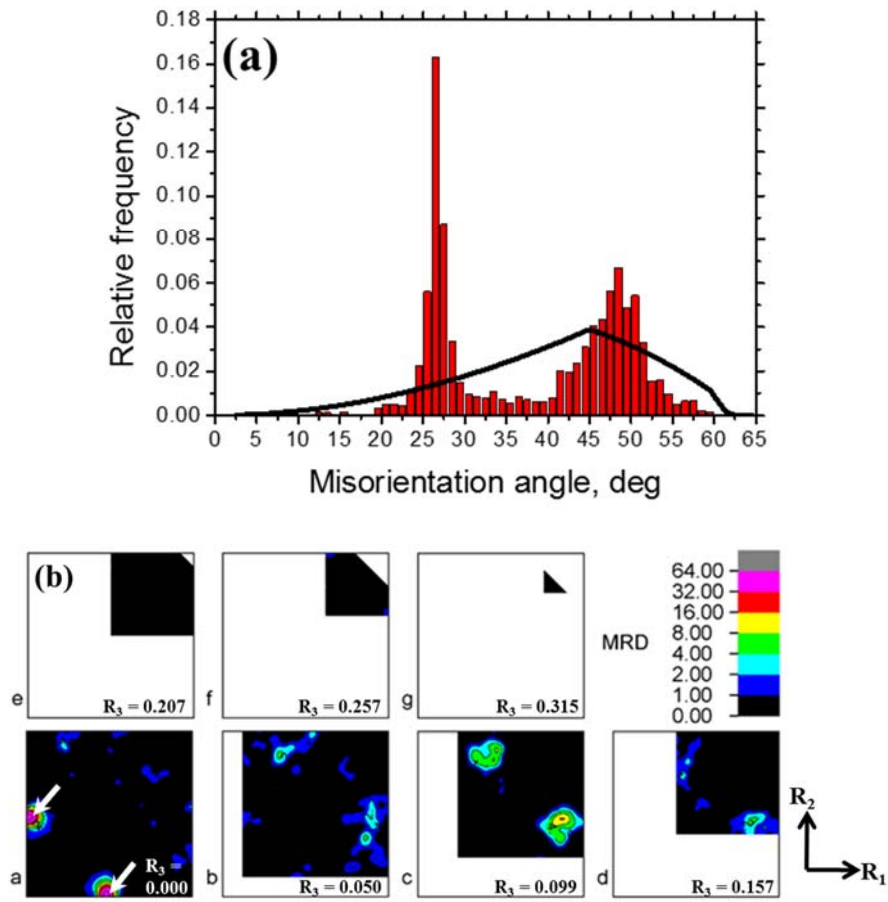


Figure 4.12 (a) Misorientation-angle distribution and (b) Rodrigues–Frank vector space $\mathbf{R}(R_1, R_2, R_3)$ for β -Mn/ α -precipitate interphase boundaries from EBSD measurements in Fig. 4.11. The black curve in (a) indicates the MacKenzie distribution.

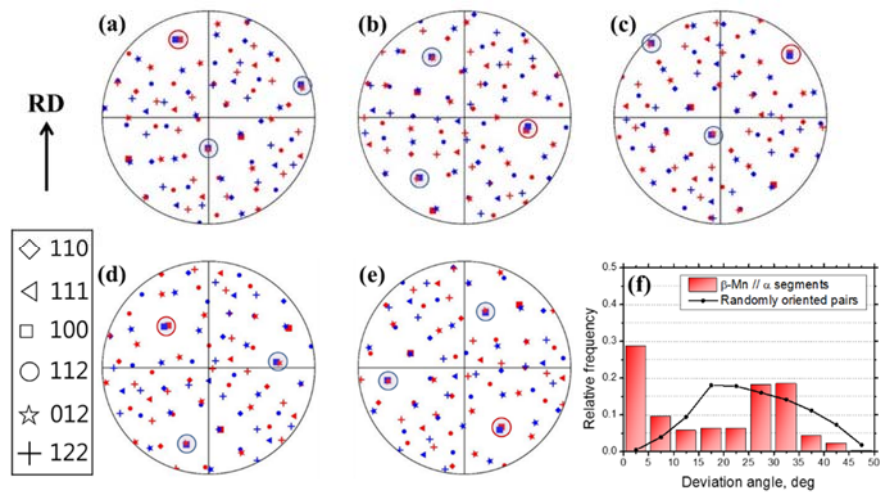


Figure 4.13 Overlaid pole figures showing the orientation relationship for (a) region 1, (b) region 2, (c) region 3, (d) region 4, and (e) region 5 in Fig. 4.11(a) β -Mn poles in red, α -precipitate poles in blue); the common interface normal is identified as well as the common direction located in the zone of the normal (dashed great circle) i.e. the trace of the interface plane. (f) Distributions of the deviation angle of β -Mn/ α -precipitate phase boundary segments from ideal β -Mn/ α -precipitate relationship. The black line in (f) indicates the distribution of deviation angles based on randomly oriented pairs of points in β -Mn and α -precipitate.

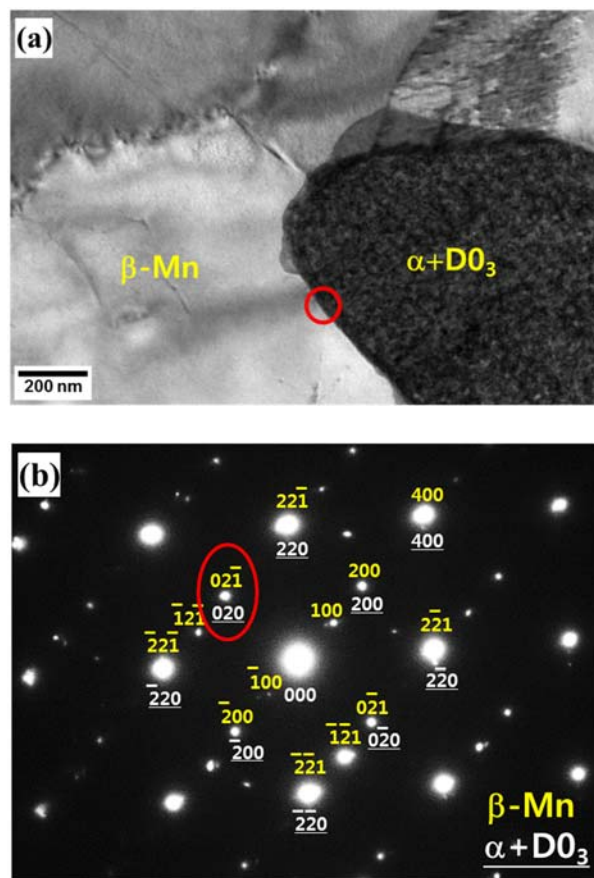


Figure 4.14 TEM micrographs and diffraction patterns at the β -Mn/ α -precipitate interphase boundaries after aging at 550 °C for 30,000 mins. (a) Bright-field image and (b) selected area diffraction pattern showing [012] zone of the β -Mn phase and [001] zone of the α -precipitate phase including partial $D0_3$ order, showing overlapped 021 β -Mn and 221 $\alpha+D0_3$ poles.

4.6 Interface character distribution of γ -matrix/ α -precipitate phase boundaries

During the aging treatment, the precipitation sequence in the investigated alloy is summarized as follows: the lath-shaped β -Mn grains are firstly formed inside the γ -matrix, and then the α -precipitate is subsequently precipitated in the interior or at the grain/phase boundaries of β -Mn phase (γ -matrix \rightarrow β -Mn \rightarrow α -precipitate) after further aging. In fact, this precipitation process is similar to multiple martensitic transformations (γ -matrix \rightarrow ε -martensite \rightarrow α' -martensite) in TRIP-aided steels [38, 39]. During these martensitic phase transformations, the Shoji–Nishiyama(S–N) orientation relationship between γ -matrix and ε -martensite ($\{111\}_{\gamma} // \{0001\}_{\varepsilon}$, $\langle 110 \rangle_{\gamma} // \langle 1120 \rangle_{\varepsilon}$) [40] and the Burgers relationship between ε -martensite and α' -martensite ($\{0001\}_{\varepsilon} // \{110\}_{\alpha'}$, $\langle 1120 \rangle_{\varepsilon} // \langle 111 \rangle_{\alpha'}$) [41] were observed. The fcc γ -matrix and bcc α' -martensite were found to follow the KS orientation relationship [1]. Also, besides the KS relationship, there were several orientation relationships found between fcc and bcc structure, such as the Bain [42], NW [2], and Pitsch [7] relationships. In light of those, the interface character between γ -matrix and α -precipitate in the investigated alloy is examined and compared to the well-known fcc/bcc orientation relationships as mentioned above.

Based on two ideal orientation relationships for γ -matrix/ β -Mn and β -

Mn/ α -precipitate interfaces obtained by the OR stereograms, respectively, the misorientation matrix between γ -matrix and α -precipitate is calculated. This idealized misorientation matrix is illustrated in Fig. 4.15, indicated by red stars around one Bain variant among three possible variants on a $\{100\}_{\alpha\text{-BCC}}$ pole figure. For comparison, all other variants of the KS, NW, and Pitsch relationships are represented together using different symbols and colors. Four variants of the ideal γ -matrix/ α -precipitate misorientation matrix surround one Bain variant in common with the NW and Pitsch, while eight KS variants are located between the NW and Pitsch variants, respectively. The crystallographic misorientation angles between each variant, including γ -matrix/ α -precipitate relationship, are also addressed on the pole figure. Notably, the γ -matrix/ α -precipitate variant has lower misorientation angle with the NW variant (3.19°), compared to the Bain (6.55°), KS (6.16°), and Pitsch (6.89°) variants. This means that the idealized γ -matrix/ α -precipitate interface character developed through β -Mn transformation is closer to the NW relationship than other conventional fcc/bcc relationships.

As shown in the EBSD phase map (Fig. 4.11(a)), γ -matrix/ α -precipitate interphase boundaries were also formed in the A30K specimen. To investigate the interface character from actual experimental results, the γ -matrix/ α -precipitate interphase boundaries were segmented and extracted from the measured EBSD map. Figure 4.16(a) presents the misorientation-angle

distribution of the γ -matrix/ α -precipitate interphase boundaries with the Mackenzie distribution. The interphase boundaries are clearly concentrated in the range between 42° and 46° misorientation angles. The Rodrigues–Frank vector space $\mathbf{R}(R_1, R_2, R_3)$ for the γ -matrix/ α -precipitate interphase boundaries are shown in Fig. 4.16(b). The γ -matrix/ α -precipitate interphase boundaries have strong peaks at around $\mathbf{R} = (0.414, 0, 0)$ and $\mathbf{R} = (0, 0.414, 0)$, as indicated by white arrows in Fig. 16(b), which is equivalent to a $\langle 1\ 0\ 0 \rangle / 45^\circ$ in the axis–angle pair convention. This signifies that most of the γ -matrix/ α -precipitate interfaces in the A30K specimen have the specific fcc/bcc interface character including the Bain, KS, NW, and Pitsch relationships.

In order to distinguish more clearly, which relationship is closest to the measured γ -matrix/ α -precipitate interfaces, the distributions of deviation angle from each ideal fcc/bcc orientation relationship were calculated with the distributions for randomly oriented pairs, respectively, and they are shown in Fig. 4.17. Compared to the deviation angle distributions of the Bain and Pitsch relations (Fig. 4.17(a,d)), the majority of the interface segments have a relatively low deviation angle below 5° with the KS and NW relations (Fig. 4.17(b,c)). In particular, the fraction of the deviation angles below 2.5° in the NW (32.8%) is relatively higher than that in the KS (25.7%). Consequently, considering the aspects of not only the misorientation obtained from two ideal orientation relationships (γ -matrix/ β -Mn and β -Mn/ α -precipitate) but also the

measured EBSD results, the γ -matrix/ α -precipitate interface character through β -Mn transformation is more like the NW relationship among the possible fcc/bcc relationships.

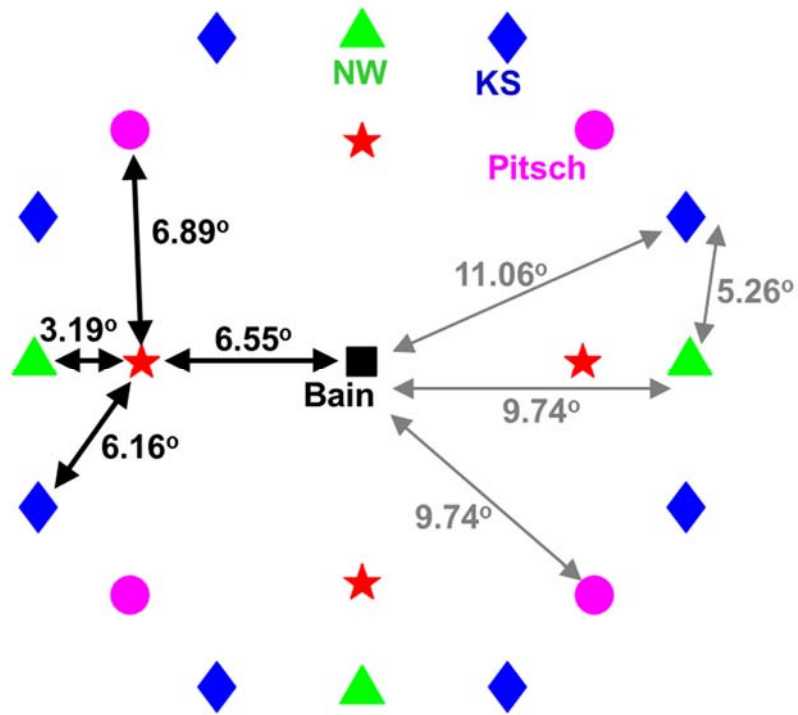


Figure 4.15 Schematic diagram of all the variants of γ -matrix/ α -precipitate relationship through β -Mn transformation in the investigated alloy around one Bain variant on a $\{100\}_{\text{BCC}}$ pole figure, indicated by red stars. The KS, NW and Pitsch relationships are shown together with the different symbols and colors.

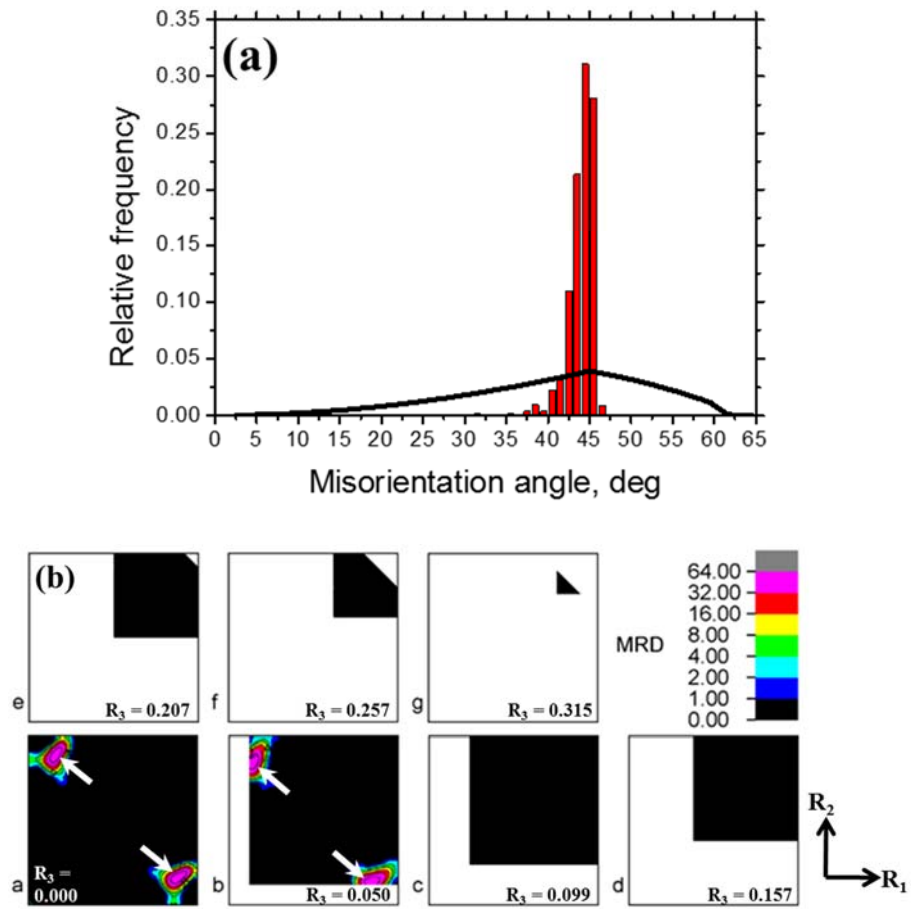


Figure 4.16 (a) Misorientation-angle distribution and (b) Rodrigues–Frank vector space $\mathbf{R}(R_1, R_2, R_3)$ for γ -matrix/ α -precipitate interphase boundaries from EBSD measurements in Fig. 4.11. The black curve in (a) indicates the MacKenzie distribution.

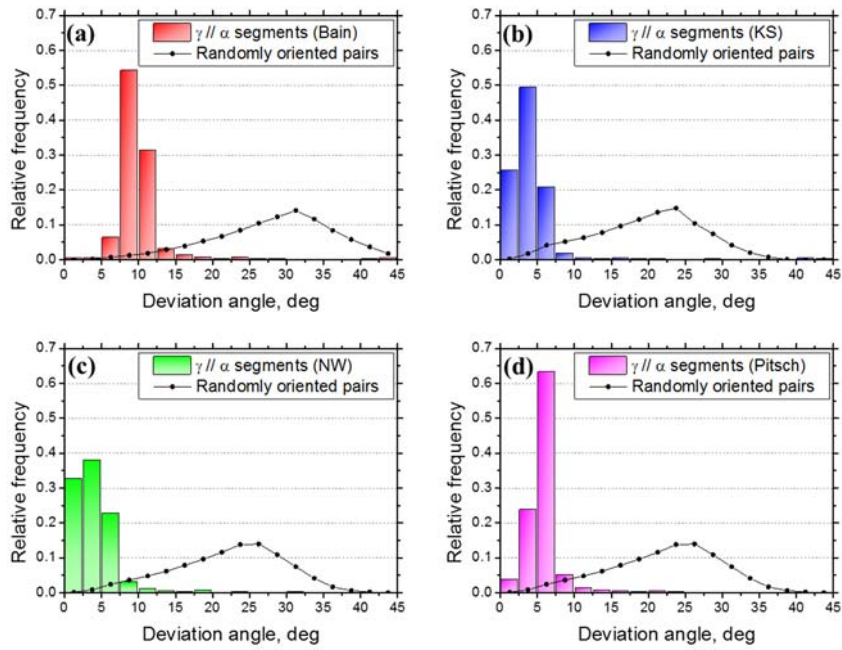


Figure 4.17 Distributions of deviation angle of γ -matrix/ α -precipitate phase boundary segments from ideal (a) Bain, (b) KS, (c) NW, and (d) Pitsch relationships. The black curves indicate the distribution of deviation angles based on randomly oriented pairs of points in γ -matrix and α -precipitate.

4.7 Conclusion: Investigation of the aging behavior and orientation relationships

This research investigated the aging behavior and orientation relationships in Fe–31.4Mn–11.4Al–0.89C low-density steel with respect to constituent phases and precipitates, including γ -austenite matrix, β -Mn, and α -precipitate. From the microstructural changes and corresponding mechanical response during aging at 550 °C, the primary age hardening at the incipient stage of aging below 300 min was induced by nano-sized κ -carbide precipitation within the γ -matrix. After aging for 300 min, a dramatic secondary hardening response was found, which was attributed to formation of the lath-type β -Mn phase. The α -precipitates with partial $D0_3$ order were subsequently formed inside and at grain/phase boundaries of the β -Mn phase by further aging treatment.

The misorientation-angle distribution and Rodrigues–Frank vector space for both γ -matrix/ β -Mn and β -Mn/ α -precipitate interphase boundaries calculated from EBSD measurements indicated that the preferred orientation relationships obviously existed for both interphase boundaries, respectively. From the OR stereograms for the γ -matrix/ β -Mn interphase boundaries, the preferred orientation relationship was represented as $(111)_\gamma // (221)_{\beta\text{-Mn}}$, $(01\bar{1})_\gamma // (01\bar{2})_{\beta\text{-Mn}}$, $(\bar{2}11)_\gamma // (\bar{5}42)_{\beta\text{-Mn}}$, and the axis-angle description of the

disorientation is $\langle 3.1 \ 2.2 \ 10.6 \rangle / 19.6^\circ$. Also, the OR stereograms revealed that the orientation relationship between β -Mn phase and α -precipitate showed up as $(012)_{\beta\text{-Mn}} // (001)_{\alpha}$, $(02\bar{1})_{\beta\text{-Mn}} // (010)_{\alpha}$, $(100)_{\beta\text{-Mn}} // (100)_{\alpha}$, which is in excellent agreement with the previous TEM studies. Both orientation relationships obtained from the OR stereograms were clarified by checking the deviation angle distributions of interface segments from the ideal orientation relationships, as well as the TEM diffraction patterns at the interface boundaries.

Based on the γ -matrix/ β -Mn and β -Mn/ α -precipitate orientation relationships, the interface character between the γ -matrix and α -precipitate was examined and compared to conventional fcc/bcc orientation relationships. A majority of the interphase boundaries followed the specific fcc/bcc orientation relationships including the Bain, KS, NW, and Pitsch relationships. The deviations from misorientations associated with idealized orientation relationships, as well as measured EBSD results indicated that the γ -matrix/ α -precipitate interface character through β -Mn transformation was closer to the NW relationship among the possible fcc/bcc relationships.

4.8 References

- [1] G. Kurdjumow, G. Sachs, *Z. Phys.*, 64 (1930) 325-343.
- [2] Z. Nishiyama, *Sci. Rep. Inst.*, 23 (1934/1935) 638.
- [3] H.N. Han, C.G. Lee, C.S. Oh, T.H. Lee, S.J. Kim, *Acta Mater.*, 52 (2004) 5203-5214.
- [4] K. Verbeken, L. Barbe, D. Raabe, *ISIJ Int.*, 49 (2009) 1601-1609.
- [5] S.B. Lee, J.E. LeDonne, S.C.V. Lim, I.J. Beyerlein, A.D. Rollett, *Acta Mater.*, 60 (2012) 1747-1761.
- [6] V. Tari, A.D. Rollett, H. Beladi, *J. Appl. Crystallogr.*, 46 (2013) 210-215.
- [7] W. Pitsch, *Acta Metall.*, 10 (1962) 897.
- [8] H.K.D.H. Bhadeshia, R.W.K. Honeycombe, *Steels : microstructure and properties*, 3rd ed., Elsevier, Butterworth-Heinemann, Amsterdam and Boston, 2006.
- [9] D.J. Dyson, S.R. Keown, D. Raynor, J.A. Whiteman, *Acta Metall.*, 14 (1966) 867.
- [10] A. Zargaran, H.S. Kim, J.H. Kwak, N.J. Kim, *Met. Mater. Int.*, 21 (2015) 79-84.
- [11] S.J. Park, B. Hwang, K.H. Lee, T.H. Lee, D.W. Suh, H.N. Han, *Scr. Mater.*, 68 (2013) 365-369.
- [12] K. Lee, S.J. Park, Y.S. Choi, S.J. Kim, T.H. Lee, K.H. Oh, H.N. Han, *Scr. Mater.*, 69 (2013) 618-621.

- [13] R. Rana, C. Liu, R.K. Ray, *Acta Mater.*, 75 (2014) 227-245.
- [14] G. Frommeyer, U. Brux, *Steel Res. Int.*, 77 (2006) 627-633.
- [15] R.A. Howell, D.C. Van Aken, *Iron Steel Technol.*, 6 (2009) 193-212.
- [16] L. Bartlett, D. Van Aken, *JOM*, 66 (2014) 1770-1784.
- [17] K. Lee, S.J. Park, J. Lee, J. Moon, J.Y. Kang, D.I. Kim, J.Y. Suh, H.N. Han, *J. Alloy. Compd.*, 656 (2016) 805-811.
- [18] K. Lee, S.J. Park, J. Moon, J.Y. Kang, T.H. Lee, H.N. Han, *Scr. Mater.*, 124 (2016) 193-197.
- [19] S.H. Kim, H. Kim, N.J. Kim, *Nature*, 518 (2015) 77-79.
- [20] S.C. Tjong, *Mater. Charact.*, 24 (1990) 275-292.
- [21] K.H. Han, W.K. Choo, *Metall. Trans. A*, 20 (1989) 205-214.
- [22] K. Sato, K. Tagawa, Y. Inoue, *Metall. Trans. A*, 21 (1990) 5-11.
- [23] A. Mohamadizadeh, A. Zarei-Hanzaki, H.R. Abedi, S. Mehtonen, D. Porter, *Mater. Charact.*, 107 (2015) 293-301.
- [24] D.G. Morris, S. Gunther, *Acta Mater.*, 44 (1996) 2847-2859.
- [25] T.F. Liu, C.C. Wu, *Scr. Metall.*, 23 (1989) 1243-1248.
- [26] B.L. Adams, S.I. Wright, K. Kunze, *Metall. Trans. A*, 24 (1993) 819-831.
- [27] X. Liu, N.T. Nuhfer, A.D. Rollett, S. Sinha, S.B. Lee, J.S. Carpenter, J.E. LeDonne, A. Darbal, K. Barmak, *Acta Mater.*, 64 (2014) 333-344.
- [28] F.C. Frank, *Metall. Trans. A*, 19 (1988) 403-408.
- [29] A. Morawiec, *Orientations and rotations : computations in crystallographic textures*, Springer, Berlin and New York, 2004.

- [30] H.J. Bunge, Texture analysis in materials science : mathematical methods, English ed., Butterworths, London ; Boston, 1982.
- [31] A.J. Schwartz, Electron backscatter diffraction in materials science, 2nd ed., Springer, New York, 2009.
- [32] B. Sundman, B. Jansson, J.O. Andersson, Calphad, 9 (1985) 153-190.
- [33] M.S. Kim, Y.B. Kang, Calphad, 51 (2015) 89-103.
- [34] M.A. Groeber, M.A. Jackson, Integrating Materials and Manufacturing Innovation, 3 (2014) 5.
- [35] J.K. Mackenzie, Biometrika, 45 (1958) 229-240.
- [36] D.A. Porter, K.E. Easterling, M.Y. Sherif, Phase transformations in metals and alloys, 3rd ed., CRC Press, Boca Raton, FL, 2009.
- [37] I. Baker, R.K. Zheng, D.W. Saxey, S. Kuwano, M.W. Wittmann, J.A. Loudis, K.S. Prasad, Z.W. Liu, R. Marceau, P.R. Munroe, S.P. Ringer, Intermetallics, 17 (2009) 886-893.
- [38] G. Frommeyer, U. Brux, P. Neumann, ISIJ Int., 43 (2003) 438-446.
- [39] T.H. Ahn, S.B. Lee, K.T. Park, K.H. Oh, H.N. Han, Mat. Sci. Eng. A, 598 (2014) 56-61.
- [40] Z. Nishiyama, M.E. Fine, M. Meshii, C.M. Wayman, Martensitic transformation, Academic Press, New York, 1978.
- [41] W.G. Burgers, Physica, 1 (1934) 561-586.
- [42] E.C. Bain, Trans. Ame. Ins. Min. Met. Eng., 70 (1924) 25-46.

Chapter 5

Dual-scale correlation of mechanical behavior in duplex low-density steel

5.1 Introduction

Recently, decreasing carbon dioxide emissions and improving fuel efficiency have been global issues in the automotive industry. Accordingly, much research has been performed to develop many kinds of advanced high-strength steels (AHSSs), such as dual-phase (DP) and transformation-induced plasticity (TRIP) steels, in order to reduce the weight of automotive parts [1-4]. Interest in low-density steels with high strength and toughness is emerging in automotive applications, and many kinds of low-density steel have been developed [2, 5-8]. Among the low-density AHSSs, duplex low-density steels containing light substitutional elements have drawn attention to obtain a balance between strength and ductility [2, 5-7]. These duplex steels, which are composed of ferrite and retained austenite, show complex deformation behavior, which arises from the interactions among the different microstructural constituents. To ensure reliable alloy and processing designs of the duplex low-density steels, it is necessary to understand the influence of the intrinsic behavior of their microstructural constituents on the macro-scale deformation

behavior, including the plastic yielding and deformation-induced martensitic transformation (DIMT) of retained austenite [5, 9].

In this study, a dramatic difference in the macroscopic tensile behavior regarding yield strength, yield point, and strain hardening was introduced to two specimens of duplex low-density steel with the same nominal chemical composition, obtained under specific heat-treatment conditions. In order to understand the difference in the macro-scale mechanical behavior despite the similar microstructures, the intrinsic mechanical properties of each phase were measured by nano-indentation and analyzed by a combination with Hall-Petch relationship. In addition, the mechanical stability of retained austenite was investigated by in-situ electron backscattered diffraction (EBSD) and energy-dispersive X-ray spectroscopy (EDX) in transmission electron microscopy (TEM).

5.2 Experimental procedure

An alloy with a chemical composition of Fe–0.23C–8.1Mn–5.3Al–0.01Si (wt.%) was prepared by vacuum induction melting. The specific process conditions of the alloy have been presented in our previous work [6]. Two low-density steel specimens were prepared for experiments by cold-rolling and annealing at 800 °C (T800) and 900 °C (T900) for 2 minutes in an infrared heating furnace. Macroscopic tensile behaviors of both steels were measured with sub-sized specimens according to ASTM-E8M at a crosshead speed of 2 mm/min with a gauge length of 25 mm. For statistically reliable analysis of microstructure, the phase fractions and grain size distributions were measured at three different regions in both specimens using EBSD. Misorientation angle of 5° was taken as a threshold value for grain definition.

Nano-indentation tests were performed using a Hysitron Tribolab nano-indentation system in load control at a constant loading rate of 200 μNs^{-1} . A Berkovich-type indenter with a half angle of 65.3° was used. To investigate the intrinsic mechanical properties of each phase in T800 and T900 without the grain boundary effect, two different indentation methods were applied for each phase in two specimens. For α -ferrite, which has a large grain size compared to the size of indenter tip, a total of 100 indentations were performed in a 10×10 rectangular array with a spacing of 5 μm between each indentation. To exclude the grain boundary effect, only the indentation marks located inside the α -

ferrite grains with sufficient distance from the grain boundaries were selected for the analysis, based on the EBSD band contrast map of nano-indentation regions [10]. In the case of α -ferrite and austenite grains with smaller grain size, a scanning probe microscope (SPM) was used in the nano-indentation system, which made it possible to evaluate the grain morphologies and to precisely identify the areas that had been previously analyzed by EBSD [11]. Guided by the EBSD and SPM images, individual α -ferrite and austenite grains were selected for nano-indentation.

The stability of the retained austenite grains in both specimens during tensile deformation was analyzed using in-situ EBSD. The microstructure change along with DIMT phenomena was measured during tensile deformation inside a scanning electron microscope (SEM) chamber [12]. The chemical composition in the retained austenite phase was measured by EDX in TEM from 10 to 20 austenite grains, and average values were selected.

5.3 Macroscopic tensile behavior and initial microstructure

Engineering stress-strain curves and true stress-strain curves with corresponding strain hardening rate of T800 and T900 are shown in Figure 5.1. Although both alloys have the same nominal chemical composition, dramatically different macro-scale tensile behavior was shown in both steels. The yield strength of T800 is 718 MPa, which is quite higher than the 561 MPa obtained for T900. While T800 shows a distinct yield point phenomenon, there is no yield point phenomenon in the stress-strain curve of T900. A point of inflection indicated by red arrow is observed in the strain-hardening rate curve of T900, which might have been caused by the DIMT of the metastable austenite. In addition, the elongation of T900 is much higher than that of T800.

Figure 5.2 shows one of EBSD phase maps of T800 and T900, respectively. Both steels contain δ -ferrite with layered structure along the rolling direction, small sized α -ferrite, and metastable austenite (γ). The bimodal size distribution in ferrite grains is caused by aluminum which stabilizes ferrite to remain stable even at high temperature where hot-rolling was performed. The remaining elongated coarse one is δ -ferrite, while small α -ferrite forms by annealing after cold-rolling. The grain size of each phase and the volume fraction of austenite in specimens obtained from the EBSD measurements are listed in Table 5.1. The grain size of δ -ferrite is about 10 μm , and the grain sizes of α -ferrite and

austenite are less than 1 μm in both specimens. T900 has larger grain sizes of α -ferrite and austenite, a smaller grain size of δ -ferrite, and a larger austenite fraction compared to T800.

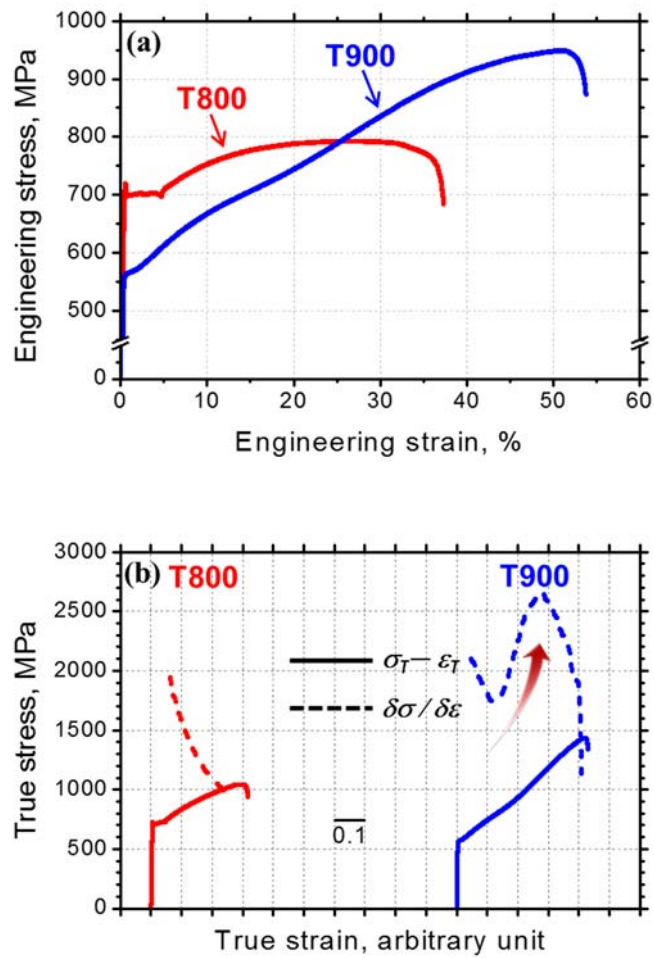


Figure 5.1 (a) Engineering stress-strain curves and (b) true stress-strain curves with corresponding strain hardening rate as a function of true strain for T800 and T900 specimens.

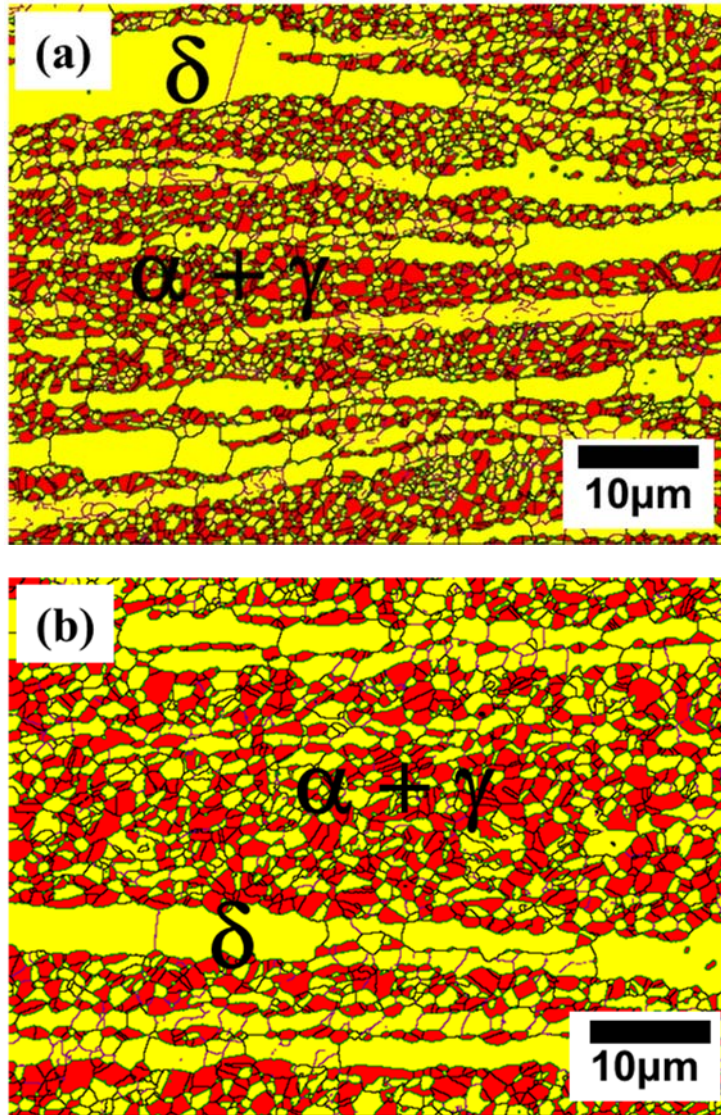


Figure 5.2 EBSD phase map of cold-rolled and annealed specimens: (a) T800; (b) T900 (■ FCC; ■ BCC).

Table 5.1 Grain size of each phase and austenite fraction of the alloys obtained from EBSD.

Sample	δ -ferrite	α -ferrite	Austenite	f_{γ} (%)
	Grain size (μm)			
T800	10.90	0.68	0.54	36.7
T900	8.62	0.79	0.70	41.4

5.4 Correlation between macro-scale uniaxial tension and nano-scale indentation

Figure 5.3 shows the load-displacement curves obtained from the nano-indentation of each phase in the specimens. The dashed lines on the curves are the theoretical Hertzian elastic solution, assuming that the indenter tip is spherical at shallow depths [13]:

$$P = \frac{4}{3} E_r \sqrt{R} \delta^3 \quad (1)$$

where P is the load applied by indenter, δ is the corresponding indentation depth, R is the radius of indenter tip, and E_r is the effective modulus. R was determined to be 200 nm from a calibration using standard fused quartz. E_r can be obtained from the unloading curve in the load-displacement curve fitted to the power law [14]. In the loading curves of δ - and α -ferrites of both specimens, sudden displacement excursions called “pop-in” are observed for most indentations. Before the pop-ins, the experimental loading curves match the theoretical curve well, indicating an elastic response before pop-in. Clear pop-in is not detected in the loading curve of the austenite phase in both specimens. It is known that this pop-in phenomenon is closely related to the dislocation nucleation at the elasto-plastic transition, and the difference in pop-in phenomenon between ferrite and austenite arises from the different mechanism of dislocation

nucleation in BCC and FCC structure [15, 16].

With regard to the initial yield strength of each phase, the maximum shear stress underneath the indenter, τ_m^0 , at the elasto-plastic transition might become a parameter to compare the macro-scale mechanical behavior with the nano-scale indentation. It can be calculated from Hertzian analysis [13]:

$$\tau_m^0 = 0.31 \left(\frac{6P_m E_r^2}{\pi^3 R^2} \right)^{1/3} \quad (2)$$

where P_m is the first load beyond which Hertzian elastic behavior is not observed. The τ_m^0 values of all phase in the specimens were determined to be in the range of 4.9 to 8.3GPa, which corresponds to $G/10$ to $G/16$, where G , the shear modulus of steel at room temperature, is about 80 GPa [17]. These values of τ_m^0 are within the range of values for the theoretical strength of a crystalline material [18], indicating that the elasto-plastic transition in the specimens are likely not the result of movement of the existing dislocations, but of dislocation nucleation. T800.

Since τ_m^0 was determined from measurements inside of each grain, the effect of grain size on the yielding should be considered to evaluate the substantial initial yield stress of each phase from the viewpoint of nano-indentation scale. The well-known Hall-Petch relationship was combined with

the intrinsic τ_m^0 at the elasto-plastic transition measured by nano-indentation as follows:

$$\tau_m = \tau_m^0 + 0.5bk_y / \sqrt{d} \quad (3)$$

where τ_m , d , and k_y are the maximum shear stress reflecting the grain size effect, the mean grain size, and Hall-Petch constant, respectively. Since the Hall-Petch constant is normally obtained under uniaxial stress state, a conversion factor of 0.5 was applied to the shear stress state based on Tresca yield criterion. The constant b reflects the almost tenfold difference between the maximum shear stress for a single grain (4.9-8.3 GPa) and the yield stress of polycrystalline material (561 MPa and 718 MPa in Figure 5.1). Actually, the value of b should depend on indenter radius due to size-dependent pop-in stresses [19]. Here, b is assumed to be 10. It is generally known that austenite has a little higher k_y values than ferrite in steel [20, 21]. k_y values reported for duplex stainless steels of 0.21 MPa m^{0.5} for ferrite and 0.32 MPa m^{0.5} for austenite were used [20]. The above equation is valid under the assumption that the plastic yielding is mostly controlled by dislocation nucleation rather than movement of existing dislocations. Since the specimens are well-annealed, Eq. (3) is expected to work effectively.

Figures 5.4 shows the maximum shear stresses underneath the indenter

upon initial yielding for each phase in T800 and T900, respectively. The solid and hatched marks indicate τ_m^0 and τ_m , respectively, for each phase. All values of τ_m^0 for all phases in T800 are higher than those in T900. From the viewpoint of τ_m^0 values without consideration of the grain size effect, α -ferrite is the stiffest phase, and austenite is the weakest phase in both T800 and T900. However, when the effect of grain size on the initial yielding for each phase is considered using τ_m , while δ -ferrite is the softest phase in T800, austenite is still the softest phase in T900. As listed in Table 5.1, δ -ferrite has a relatively large grain size compared with other phases, and the grain size of austenite is the smallest in both T800 and T900. However in comparison with austenite in both specimens, the different annealing temperature causes that the grain size of austenite in T900 is much larger than that in T800. Therefore, in the macro-scale tensile test, it can be said that the initial yielding arises at δ -ferrite in T800 and at austenite in T900, respectively, from the dual-scale correlation between macro-scale tensile behavior and nano-indentation results.

It is well known that the yield point phenomenon is normally observed in tensile tests of ferritic steels, but not of austenitic steels. In addition, since the large pop-ins in the nano-indentation load-displacement curves of δ -ferrite in Figures 5.3(a,b) could be closely correlated with yield drops in the macro-scale tensile stress-strain curves [10], the distinct yield point phenomenon in only

T800 shown in Figure 1 (a) also demonstrates that δ -ferrite is the dominant phase in the initial yielding of T800. In contrast, T900 has lower yield strength than T800, and does not show the yield point phenomenon. This implies that the initial yielding in T900 is controlled by the austenite phase. These results are in full accord with the analysis of τ_m based on nano-scale indentation measurement, that τ_m of the δ -ferrite in T800 is larger than that of austenite in T900.

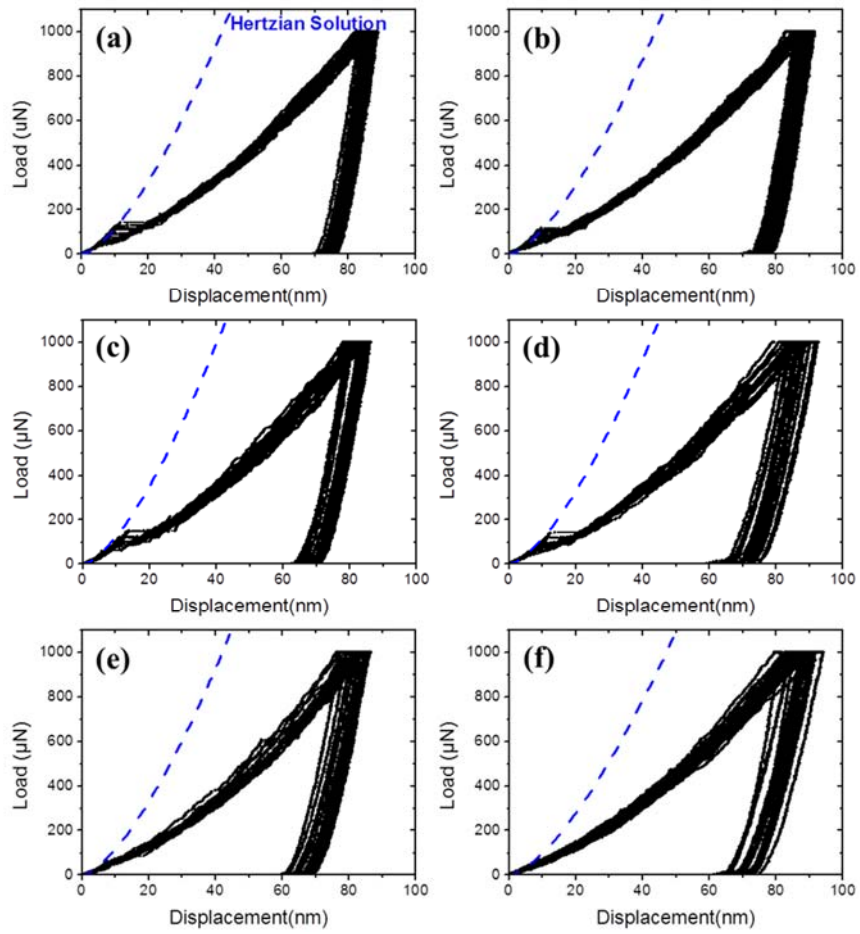


Figure 5.3 Nano-indentation load-displacement curves of T800 (a) δ -ferrite, (c) α -ferrite, (e) austenite and T900 (b) δ -ferrite, (d) α -ferrite, (f) austenite. Blue dashed lines indicate the theoretical Hertzian elastic solution.

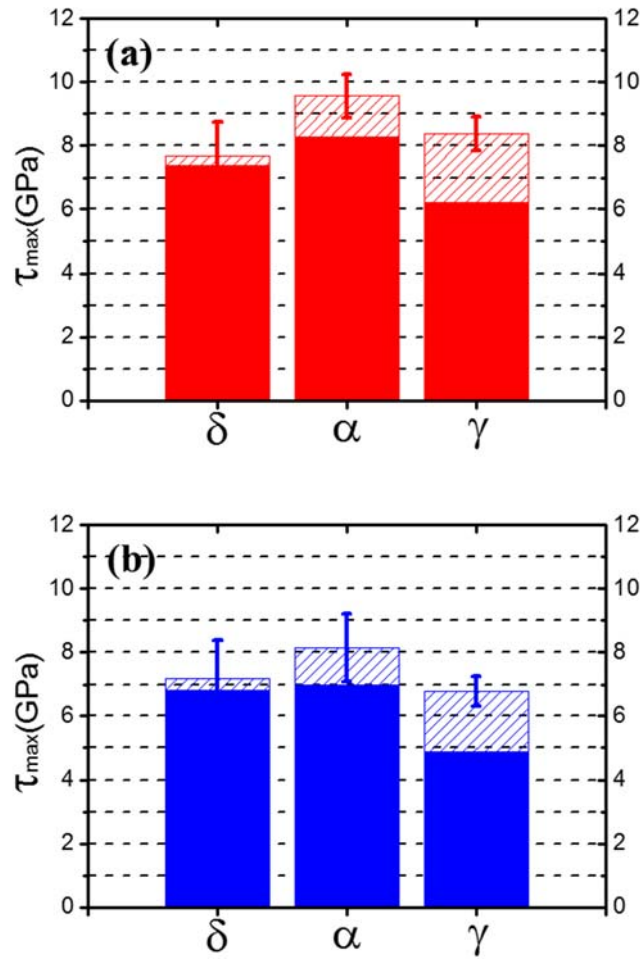


Figure 5.4 Maximum shear stress underneath indenter for each phase: (a) T800; (b) T900 (■ the intrinsic value; ▨ the value considered grain size effect).

5.5 Deformation-induced martensitic transformation

As mentioned in the description of Figure 5.1(b), the inflection point in the strain-hardening rate curve in T900 might be related to the DIMT of metastable austenite in the T900 specimen. In order to directly observe DIMT in both specimens, EBSD phase maps at the same locations of specimens during stepwise uniaxial tension were obtained, as shown in Figure 5.5. To trace the microstructure of the same area on the specimen during deformation, four rectangular micro-indentation marks were placed on the specimen surface before loading. A sub-grain boundary, defined by misorientation angle from 2° to 5° , is exclusively observed in a small number of δ -ferrite in T800. This comes from the slightly insufficient recovery of T800 during the annealing process in comparison with T900.

Figure 5.5(e) shows that DIMT is detected in T900 at only 3.9% strain, and increased as the macroscopic strain is increased, whereas DIMT could not be observed in T800 at up to 12.4%. The differences in microstructural changes during the deformation of two specimens can be explained by the mechanical stability of retained austenite in both specimens. The mechanical stability of retained austenite is usually ascribed to its size and shape [22], chemical composition [23], partitioning of strain [24, 25] and crystallographic orientation [7, 26]. Among these, the crystallographic orientation could be a minor factor in this research, because the austenite phases in both specimens have similar

texture distributions. The grain size of the retained austenite in T800 is smaller than that in T900, so T800 has higher mechanical stability of the austenite phase with respect to grain size. In addition, since the initial yielding in T900 is controlled by the retained austenite phase according to the analysis of τ_m , the strain might concentrate in the retained austenite phase in T900 during tensile tests, resulting in the DIMT at an early stage of the deformation of T900. However, since the weakest phase in T800 is δ -ferrite, the strain of austenite in T800 is smaller than that of δ -ferrite. Therefore, T800 could have more advantages in protecting austenite grains by strain partitioning than T900.

The difference in austenite stability between T800 and T900 can also be understood in terms of the difference in chemical composition. TEM/EDS and XRD analyses resulted in 0.551 wt.%C–9.18 wt.%Mn and 0.451wt.%C–8.99 wt.%Mn in T800 and T900, respectively. It is confirmed that the austenite phase in T900 has a lower content of C and Mn compared to T800, which are well-known austenite stabilizers [27]. It indicates that intrinsic mechanical property of austenite in T900, which is relatively dilute, are softer than that in T800 as shown in Fig. 5.4. In addition, the lower C and Mn content of the austenite in T900 makes the austenite less stable than that in T800.

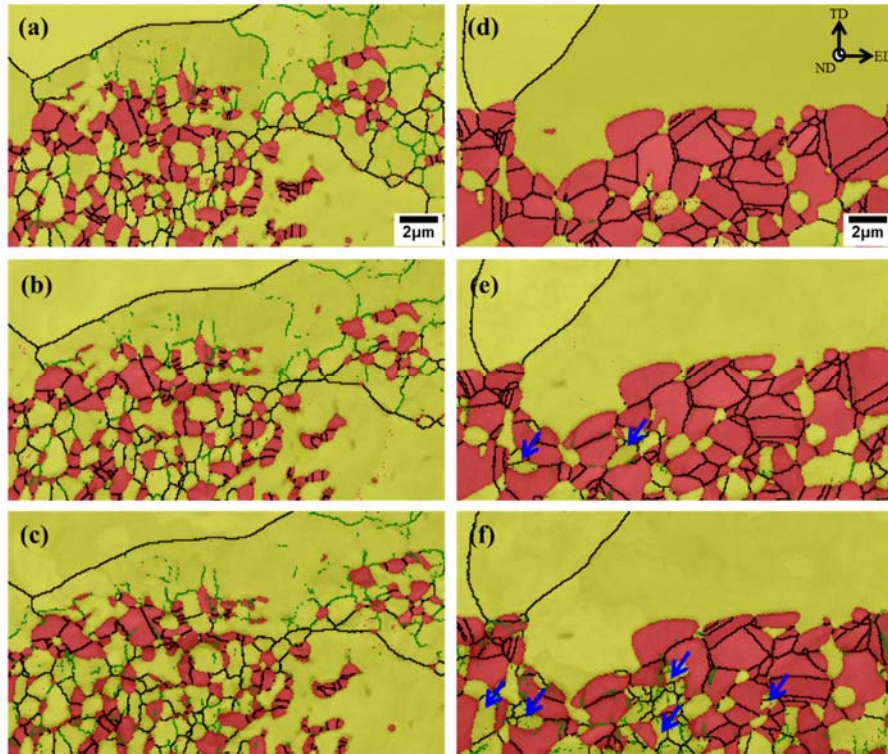


Figure 5.5 EBSD phase maps of T800 at true strains of (a) 0%, (b) 5.5%, (c) 12.4% and T900 at true strains of (d) 0%, (e) 3.9% and (f) 10.5%. (■ FCC; ■ BCC; — misorientation angle $> 5^\circ$; — misorientation angle $2\sim 5^\circ$) Blue arrows indicate martensite transformed from retained austenite.

5.6 Conclusion: Dual-scale correlation of mechanical behavior

In this study, the dual-scale correlation between macro-scale tensile test and nano-scale indentation of a duplex low-density steel was carried out, in order to explain the dramatic differences in macro-scale tensile behavior in two specimens obtained under specific heat-treatment conditions, despite the same nominal chemical composition and similar microstructures. From nano-indentation, first, the maximum shear stress at the elasto-plastic transition for each phase in both specimens was determined. The effect of grain size on the yielding was considered to evaluate the substantial initial yield stress of each phase from the viewpoint of nano-indentation scale using Hall-Petch relationship. In addition, DIMT was observed by in-situ EBSD in order to compare the mechanical stability of retained austenite in two specimens. Based on these approaches, the dramatic differences of the macroscopic tensile behavior regarding the yield strength, yield point phenomenon, and strain hardening in the two specimens was successfully explained.

5.7 References

- [1] T. Senuma, *ISIJ Int*, 41 (2001) 520-532.
- [2] G. Frommeyer, U. Brux, P. Neumann, *ISIJ Int*, 43 (2003) 438-446.
- [3] H.N. Han, C.G. Lee, D.W. Suh, S.J. Kim, *Mat Sci Eng A*, 485 (2008) 224-233.
- [4] N. Lim, H. Park, S. Kim, C. Park, *Met Mater Int*, 18 (2012) 647-654.
- [5] D.W. Suh, S.J. Park, T.H. Lee, C.S. Oh, S.J. Kim, *Metall Mater Trans A*, 41A (2010) 397-408.
- [6] S.J. Park, B. Hwang, K.H. Lee, T.H. Lee, D.W. Suh, H.N. Han, *Scripta Mater*, 68 (2013) 365-369.
- [7] C.H. Seo, K.H. Kwon, K. Choi, K.H. Kim, J.H. Kwak, S. Lee, N.J. Kim, *Scripta Mater*, 66 (2012) 519-522.
- [8] D.W. Suh, N.J. Kim, *Scripta Mater*, 68 (2013) 337-338.
- [9] H.N. Han, C.G. Lee, C.S. Oh, T.H. Lee, S.J. Kim, *Acta Mater*, 52 (2004) 5203-5214.
- [10] T.H. Ahn, C.S. Oh, K. Lee, E.P. George, H.N. Han, *J Mater Res*, 27 (2012) 39-44.
- [11] T.H. Ahn, C.S. Oh, D.H. Kim, K.H. Oh, H. Bei, E.P. George, H.N. Han, *Scripta Mater*, 63 (2010) 540-543.
- [12] D.H. Kim, S.J. Kim, S.H. Kim, A.D. Rollett, K.H. Oh, H.N. Han, *Acta Mater*, 59 (2011) 5462-5471.

- [13] K.L. Johnson, *Contact Mechanics*, Cambridge University Press, Cambridge, 1985.
- [14] W.C. Oliver, G.M. Pharr, *J Mater Res*, 7 (1992) 1564-1583.
- [15] H. Bei, E.P. George, J.L. Hay, G.M. Pharr, *Phys Rev Lett*, 95 (2005) 045501.
- [16] T. Ohmura, K. Tsuzaki, *J Mater Sci*, 42 (2007) 1728-1732.
- [17] D.N. Lee, *Texture and Related Phenomena*, The Korean Institute of Metals and Materials, 2006.
- [18] R.W.K. Honeycombe, *The plastic deformation of metals*, 2nd ed., E. Arnold, London ; Baltimore, Md., U.S.A., 1984.
- [19] J.R. Morris, H. Bei, E.P. George, G.M. Pharr, *Phys Rev Lett*, 106 (2011) 165502.
- [20] S. Floreen, H.W. Hayden, *Asm Trans Q*, 61 (1968) 489-499.
- [21] D.J. Abson, J.J. Jonas, *Met Sci*, 4 (1970) 24-28.
- [22] H.K.D.H. Bhadeshia, D.V. Edmonds, *Met Sci*, 17 (1983) 411-419.
- [23] C.K. Syn, B. Fultz, J.W. Morris, *Metall Trans A*, 9 (1978) 1635-1640.
- [24] Q. Furnemont, G. Lacroix, S. Godet, K.T. Conlon, P.J. Jacques, *Can Metall Quart*, 43 (2004) 35-42.
- [25] J.H. Ryu, D.I. Kim, H.S. Kim, H.K.D.H. Bhadeshia, D.W. Suh, *Scripta Mater*, 63 (2010) 297-299.
- [26] O. Muransky, P. Sittner, J. Zrnik, E.C. Oliver, *Acta Mater*, 56 (2008) 3367-3379.

- [27] A.N. Vasilakos, K. Papamantellos, G.N. Haidemenopoulos, W. Bleck,
Steel Res, 70 (1999) 466-471.

Chapter 6

Total conclusions

Low-density steels with outstanding specific strength and ductility while reducing the density have newly been developed based on novel alloy systems containing aluminum or silicon as a substitutional light element. Among the low-density steels, austenite-based high-Mn steels based on the Fe-Al-Mn-C system have attracted increasing attention as these offer excellent mechanical properties and density reduction rates. After aging treatment at appropriate temperature and time, these steels can form micro/nano-scale precipitates, such as κ -carbide, β -Mn, and bcc ordered phases (B2 or D03), inside austenite or ferrite matrix. Since these precipitates have far-reaching effects on the mechanical behavior of the low-density steels, many studies have devoted much effort to investigate their precipitation behavior and correlate with the mechanical properties.

Especially, the β -Mn phase is known for causing severe ductility loss of the high-Mn low-density steels, leading to brittle fractures and decrease of impact energy. However, there is still a paucity of characterization research on the β -Mn phase in terms of the formation behavior, microstructural evolution, and its effects on mechanical and fracture properties of austenite-based high-Mn low-density steels. Therefore, in this research, the microstructure and

mechanical behavior of low-density steels were investigated by means of complementary microstructural and mechanical characterization.

Firstly, the change of the microstructure and intrinsic mechanical properties of Fe–31.4Mn–11.4Al–0.89C low-density steel under aging heat treatment was studied by nanoindentation combined with complementary microstructural characterization. From the microstructural evolution, the β -Mn phase nucleated at both ferrite/austenite phase boundaries and austenite/austenite grain boundaries after aging for 300 minutes at 550 °C, and grew deeply into the austenite matrix by further aging treatment. The XRD analysis indicated the lattice expansion of austenite and κ -carbide from the peak shift. This result was instantiated with carbon diffusion to the austenite matrix due to β -Mn precipitation, which was examined by EPMA analysis. The Vickers hardness increased dramatically, to more than 700 HV after an aging time of 1,000 minutes. The secondary aging behavior originated from the precipitation of the β -Mn phase whose nano-hardness was measured as 13.28 ± 0.16 GPa. The average value and standard deviation of the nano-hardness of the austenite phase increased after 1,000 minutes of aging from the solution-treated state. It arose from the increase and inhomogeneous distribution of carbon content caused by β -Mn precipitation.

Secondly, the formation behavior of the β -Mn phase in high-Mn low-density steels was investigated with different chemical compositions. From the

Vickers hardness change and microstructure evolution, the Si and Al additions accelerated the primary hardening induced by κ -carbide precipitation. For 9Al-base alloys, colonies composed of α -ferrite and β -Mn phases were formed along the austenite grain boundaries after aging for 10000 min, and their size and number were greater in the 9Al-1Si alloy than those in the 9Al alloy. For 11Al alloy, the β -Mn phase, which led to the dramatic secondary hardening, was seen to have a lath-shaped morphology without the co-precipitation of α -ferrite after 1000 min of aging. These morphological and kinetic differences of the β -Mn formation were attributed to the higher Al content, which increased the driving force for β -Mn transformation. In addition, the effects of the aging process on the tensile and fracture behavior were analyzed in the 11Al alloy. A loss of elongation was observed in the specimens aged for 100 min; moreover, they ruptured before the yield point after aging for more than 300 min. The fractography analysis revealed that the β -Mn formation was the main cause of severe ductility loss of the low-density steel. In addition, the ordering of ferrite into the $D0_3$ phase acted as additional factor of ductility loss especially before the β -Mn formation.

Thirdly, the aging behavior and orientation relationships in Fe-31.4Mn-11.4Al-0.89C low-density steel were investigated with respect to constituent phases and precipitates, including γ -austenite matrix, β -Mn, and α -precipitate. The misorientation-angle distribution, Rodrigues-Frank vector space, and OR

stereogram from EBSD measurements were employed for analyzing γ -matrix/ β -Mn and β -Mn/ α -precipitate interphase boundaries, respectively. The OR stereograms showed that the preferred orientation relationships were represented as $(111)_\gamma // (221)_{\beta\text{-Mn}}$, $(01\bar{1})_\gamma // (01\bar{2})_{\beta\text{-Mn}}$, $(\bar{2}11)_\gamma // (\bar{5}42)_{\beta\text{-Mn}}$ for γ -matrix/ β -Mn interface, and $(012)_{\beta\text{-Mn}} // (001)_\alpha$, $(02\bar{1})_{\beta\text{-Mn}} // (010)_\alpha$, $(100)_{\beta\text{-Mn}} // (100)_\alpha$ for β -Mn/ α -precipitate interface, respectively. In addition, from orientation relationships of both γ -matrix/ β -Mn and β -Mn/ α -precipitate interfaces, the interface character between γ -matrix and α -precipitate was examined and compared to conventional fcc/bcc orientation relationships.

Lastly, the dual-scale correlation between macro-scale tensile test and nano-scale indentation of a duplex low-density steel was carried out, in order to explain the dramatic differences in macro-scale tensile behavior in two specimens obtained under specific heat-treatment conditions, despite the same nominal chemical composition and similar microstructures. From nano-indentation, the maximum shear stress at the elasto-plastic transition for each phase in both specimens was determined. The effect of grain size on the yielding was considered to evaluate the substantial initial yield stress of each phase from the viewpoint of nano-indentation scale using Hall-Petch relationship. In addition, DIMT was observed by *in-situ* EBSD in order to compare the mechanical stability of retained austenite in two specimens.

From this research, the β -Mn phase in austenite-based high-Mn low-density steels was described well, in terms of the formation behavior, microstructural evolution, orientation relationships, and its effects on mechanical and fracture properties. In addition, the dramatic differences of the macroscopic tensile behavior regarding the yield strength, yield point phenomenon, and strain hardening in the two duplex low-density steels was successfully explained.

국문 초록

최근 온실가스 배출 저감 및 연료 효율 증대가 자동차 업계 및 방산 소재 분야에서 주요 이슈로 대두하고 있다. 이러한 흐름에 맞춰 DP강이나 TRIP강과 같은 초고장력강판 연구 개발이 오랫동안 진행되어왔다. 그러나 철강소재의 강도가 증가할수록 강성 및 충격 특성이 저하되어, 강재와 부품의 두께 감소를 통한 경량화는 점차 한계에 이르고 있다. 이에 대응하여 일반적인 철강 소재보다 밀도를 낮춘 새로운 개념의 “경량철강” 소재가 제안되었다. 경량철강은 Fe 원자보다 원자량이 작은 치환형 원소인 Al 또는 Si를 첨가하여 밀도를 낮춘 저비중 고강도 강 소재이다.

경량철강 소재는 구성상에 따라 페라이트계, 오스테나이트계 (다상계 포함)로 나눌 수 있다. 그중에서 오스테나이트계 경량철강은 페라이트계보다 우수한 기계적 물성과 밀도 감소 효과를 보인다. 이들 강재를 적정한 온도 및 시간에서 시효처리 하였을 때, κ -carbide, ordered bcc phases, and β -Mn과 같은 다양한 석출상들이 형성되는데, 이들은 경량철강 소재의 기계적 물성에 매우 큰 영향을 끼친다. 하지만 그 중 β -Mn 상과 관련된 생성 거동, 미세조직적 특징, 기계적 물성 및 파괴 거동에 미치는

영향 등에 대한 연구는 미흡한 실정이다. 따라서 본 연구에서는 여러 분석 장비를 활용하여 시효처리 시 나타나는 고망간 경량철강 소재의 미세조직과 기계적 거동 변화에 대한 연구를 수행하였다.

먼저, Al 함량이 11.4 wt.%인 오스테나이트계 고망간 경량철강의 시효 열처리에 따른 미세조직 및 각 상의 기계적 물성 변화를 분석하였다. β -Mn 상 생성에 의한 오스테나이트 모상과 κ -carbide 상의 격자팽창을 XRD와 EPMA으로 확인하였고, Vickers 경도시험을 통해 β -Mn 상에 의한 강화효과가 뚜렷이 나타나는 것을 알 수 있었다. 나노압입시험 결과 시효열처리에 의해 오스테나이트 모상의 평균 나노 경도가 증가하고 편차가 커지는 것을 확인하였는데, 이에 대한 원인이 열처리 과정에서 일어나는 β -Mn에서 오스테나이트로의 탄소 확산으로 보고 분석해보았다.

다음으로, β -Mn 상의 생성 거동을 형상학적 특징과 화학 조성 분포 관점에서 분석하였다. 고망간 경량철강 내 Al 및 Si 함량에 따라 β -Mn 상의 생성 속도와 형상에서 큰 차이가 나타났는데, 특히 Al의 경우 열역학/석출 속도론 기반 해석 결과 Al 함량이 증가할수록 β -Mn의 생성 구동력을 높이는 것으로 확인되었다. 또한, 시효처리 공정이 고망간 경량철강 소재의 파괴 거동에 미치는 영향을 알아보기 위해 일축 인장시험을 시행해보았다. 그 결과, β -

Mn 상 생성과 함께 페라이트 결정립 내 DO_3 상 규칙화로 인하여 강재의 연신율이 급격히 감소하는 것을 알 수 있었다.

다음으로, Fe-31.4Mn-11.4Al-0.89C 경량철강 소재의 시효 거동과 구성상 및 석출상 간의 방위관계에 대해 분석해보았다. Misorientation-angle 분포, Rodrigues-Frank vector space, OR stereogram을 통하여 γ -matrix/ β -Mn과 β -Mn/ α -precipitate 상경계의 방위관계를 각각 도출하였다. 도출된 방위관계를 검증하기 위하여 이론 방위관계와 실제 계면 간의 deviation angle 분포 분석 및 TEM 회절패턴 분석을 실시하였다. γ -matrix/ β -Mn과 β -Mn/ α -precipitate 두 방위관계를 토대로 하여 최종적으로 γ -matrix와 α -precipitate 간의 계면 특성 또한 조사하였고, 기존에 알려진 fcc/bcc 방위관계와도 비교해보았다.

마지막으로, 5wt%의 Al이 첨가된 이상 조직 경량철강 소재의 기계적 성질을 거시스케일과 미시스케일에서 분석하고 그 연관성을 도출해보았다. 분석에 사용된 이상 조직 경량철강 소재는 전체 화학적 조성비가 같더라도 냉간 압연 후 열처리 온도에 따라 항복점 현상(yield drop) 및 항복강도 그리고 가공경화 거동에서 매우 큰 차이를 보였다. 이러한 거시스케일에서의 인장 거동 차이를 설명하기 위해 나노압입시험을 이용하여 이상 조직 경량철강 각

상의 기계적 물성을 측정하였고, 이를 Hall-Petch relationship 기반 결정립 크기 효과를 적용하여 거시스케일에서의 항복 거동과 연관시켜 보았다. 그리고 *in-situ* EBSD 일축 인장시험을 통하여 각 장재 내 오스테나이트 상의 기계적 안정도를 평가해보았다.

본 연구를 통해, 아직 명확하지 밝혀지지 않았던 오스테나이트계 고망간 경량철강 소재의 β -Mn 석출상과 관련된 생성 거동, 미세조직적 특징, 방위관계, 그리고 기계적 물성 및 파괴 거동에 미치는 영향에 근본적으로 이해할 수 있었다. 또한, 열처리 온도에 따른 이상조직 경량철강 소재의 거시 인장 거동 차이(항복점 현상, 항복강도, 가공경화 거동)도 성공적으로 설명할 수 있었다.

핵심어: 금속 및 합금소재, 경량철강, 시효 열처리, β -Mn, 비커스 경도, X선 회절분석, EPMA, EBSD, TEM, 형상학적 특징, 일축 인장시험, 파괴 거동, 방위관계, OR stereogram, 나노압입시험, Hall-Petch relationship, 오스테나이트

Student number: 2011-20655

Curriculum Vitae

Keunho Lee

Ph.D. student

Department of Materials Science & Engineering, College of Engineering,
Seoul National University, 151-742, Korea
TEL: 82-2-880-1489, FAX: 82-2-872-8305
e-mail: top8772@snu.ac.kr

Personal

Full name : Keunho Lee

Sex : Male

Date of birth : Sep 07, 1986

Nationality : Republic of Korea

Education

Mar. 2011 ~ Ph.D. candidate (M.S/ Ph.D. integrated course) in
present Department of Materials Science & Engineering, Seoul
National University, Seoul, Korea (Advisor: Prof. Heung
Nam Han)

Mar. 2005 ~ B.S. in Department of Materials Science &
Feb. 2011 Engineering, Seoul National University, Seoul, Korea

Experience

Mar. 2011 ~ Researcher
present Department of Materials Science & Engineering

College of Engineering, Seoul National University, Korea

< Main research projects >

1. Development of high specific strength light-weight steel for military vehicle
2. Multi-phase material design based on Integrated Computational Materials Engineering (ICME) approach
3. Investigation of nitrogen effect in deformation behavior of TRIP-aided lean duplex stainless steel
4. Development of properties analysis and optimized design technologies for high-functional 3D nano/micro structure system
5. Analysis of recrystallization and deformation textures in Magnesium alloys

Mar. 2016 ~ Visiting researcher

Sep. 2016 Department of Materials Science & Engineering,
Carnegie Mellon University, Pittsburgh, USA

<Main research project>

Analysis of orientation relationship and growth direction of β -Mn phase in high Mn low-density steel based on 2D/3D EBSD characterization (Advisor: Prof. Anthony D. Rollett)

Research Interests

1. Coupled analysis of microstructure and mechanical behavior of multi-phase low-density steels

2. Grain/boundary/interface characteristic & texture analysis of crystalline materials using Electron Back-Scattered Diffraction (EBSD)
3. Reconstruction and representation of 3-dimensional (3D) nano/micro structure with the use of Focused Ion Beam (FIB)/Scanning electron microscope (SEM) or nano/micro computed tomography (CT)
4. Nano-scale mechanical characterization of structural and functional materials using nanoindentation
5. Calculation of phase equilibrium and precipitation behavior based on the thermodynamic database
6. 3D observation and analysis of deformation twinning in Magnesium alloys

Awards

- Best paper award by 2012 6th Steel Science Forum of Korean Institute of Metals and Materials
- Best paper award by 2013 44th Spring Conference of Korean Society of Microscopy
- Best graduate student's presentation of Department of Materials Science and Engineering in Seoul National University by 2015 Materials Fair
- Best graduation award by Department of Materials Science and Engineering in Seoul National University

Journal Publications

1. Seong-Jun Park, B. Hwang, **Keunho Lee**, Tae-Ho Lee, Dong-Woo Suh, and Heung Nam Han; Microstructure and tensile behavior of duplex

low-density steel containing 5 mass% aluminum, *Scripta Materialia* 68(6), pp. 365-369, 2013

2. **Keunho Lee**, Seong-Jun Park, Yong Seok Choi, Se-Jong Kim, Tae-Ho Lee, Kyu Hwan Oh, and Heung Nam Han; Dual-scale correlation of mechanical behavior in duplex low-density steel, *Scripta Materialia* 69(8), pp. 618-621, 2013
3. Moon-Jo Kim, **Keunho Lee**, Kyu Hwan Oh, In-Suk Choi, Hyeong-Ho Yu, Sung-Tae Hong, and Heung Nam Han; Electric current-induced annealing during uniaxial tension of aluminum alloy, *Scripta Materialia* 75, pp. 58-61, 2014
4. Seong-Jun Park, Yoon Uk Heo, Yong Hoon Choi, **Keunho Lee**, Heung Nam Han, and Dong-Woo Suh; Effect of second phase on the deformation and fracture behavior of multiphase low-density steels, *JOM* 66(9), pp. 1837-1844, 2014
5. **Keunho Lee**, Kyung Il Kim, Se-Jong Kim, Dong-Woo Suh, Kyu Hwan Oh, and Heung Nam Han; Observation of micro-scale surface morphology with microtexture development during plane strain tensile deformation in AZ31 magnesium alloy, *Metallurgical and Materials Transactions A* 46A(1), pp. 12-17, 2015
6. Hae Lin Jang, **Keunho Lee**, Chan Soon Kang, Hye Kyoung Lee, Hyo-Yong Ahn, Hui-Yun Jeong, Sunghak Park, Seul Cham Kim, Kyoungsuk Jin, Jimin Park, Tae-Youl Yang, Jinhong Kim, Seon Ae Shin, Heung Nam Han, Kyu Hwan Oh, Ho-Young Lee, Jun Lim, Kug Sun Hong, Malcolm Snead, Jimmy Xu, Ki Tae Nam; Biofunctionalized Ceramic with Self-Assembled Networks of Nanochannels, *ACS Nano* 9(4)A, pp. 4447-4457, 2015
7. Se-Jong Kim, Daeyong Kim, Young-Seon Lee, Chang-Seok Oh, **Keunho Lee**, and Heung Nam Han; Influence of Constraint Condition

- on Rolling Behavior of Magnesium Alloy at Low Temperatures, *Metals and Materials International* 21(4), pp. 719-725, 2015
8. Se-Jong Kim, Daeyong Kim, **Keunho Lee**, Hoon-Hwe Cho, Heung Nam Han; Residual-stress-induced grain growth of twinned grains and its effect on formability of magnesium alloy sheet at room temperature, *Materials Characterization* 109, pp. 88-94, 2015
 9. Hoon-Hwe Cho, Dong-Wan Kim, Sung-Tae Hong, Yong-Ha Jeong, **Keunho Lee**, Yi-Gil Cho, Suk Hoon Kang, and Heung Nam Han; Three-Dimensional Numerical Model Considering Phase Transformation in Friction Stir Welding of Steel, *Metallurgical and Materials Transactions A* 46A(12), pp. 6040-6051, 2015
 10. Hae Lin Jang, Guang Bin Zheng, Jungha Park, Hwan D. Kim, Hae-Ri Baek, Hye Kyoung Lee, **Keunho Lee**, Heung Nam Han, Choon-Ki Lee, Nathaniel S. Hwang, Jae Hyup Lee and Ki Tae Nam; In vitro and in vivo evaluation of whitlockite biocompatibility: comparative study with hydroxyapatite and β -tricalcium phosphate, *Advanced Healthcare Materials* 5(1), pp. 128–136, 2016
 11. **Keunho Lee**, Seong-Jun Park, Jaeun Lee, Joonoh Moon, Jun-Yun Kang, Dong-Ik Kim, Jin-Yoo Suh, and Heung Nam Han; Effect of aging treatment on microstructure and intrinsic mechanical behavior of Fe–31.4Mn–11.4Al–0.89C lightweight steel, *Journal of Alloys and Compounds* 656, pp. 805-811, 2016
 12. Jeom Yong Choi, Jaeun Lee, **Keunho Lee**, Ji-Yeon Koh, Jae-Hyung Cho, Heung Nam Han, Kyung-Tae Park; Effects of the strain rate on the tensile properties of a TRIP-aided duplex stainless steel, *Materials Science & Engineering A* 666, pp. 280–287, 2016
 13. You Jung Lee, Hyun-Min Sung, Younggil Jin, **Keunho Lee**, Chong Rae Park, Gon-Ho Kim and Heung Nam Han; Improvement of

Mechanical Property of Air Plasma Sprayed Tungsten Film Using Pulsed Electric Current Treatment, *International Journal of Refractory Metals and Hard Materials* 60, pp. 99-103, 2016

14. **Keunho Lee**, Seong-Jun Park, Joonoh Moon, Jun-Yun Kang, Tae-Ho Lee, and Heung Nam Han; β -Mn formation and aging effect on the fracture behavior of high-Mn low-density steels, *Scripta Materialia* 124, pp. 193-197, 2016
15. **Keunho Lee**, Seong-Jun Park, Jun-Yun Kang, Siwook Park, Sang Sub Han, Jun Young Park, Kyu Hwan Oh, Sukbin Lee, Anthony D. Rollett, and Heung Nam Han; Investigation of the aging behavior and orientation relationships in Fe-31.4Mn-11.4Al-0.89C low-density steel, *in preparation*, 2016

Presentations

1. **Keunho Lee**, Tae-Hong Ahn, Yong-Min Kim, Yong Seok Choi, Seong-Jun Park, Kyu Hwan Oh and Heung Nam Han; Dual-scale mechanical behavior of dual phase low-density steels by nano-indentation and in-situ EBSD, *The 7th GIFT-KIMS-SNU-Kyushu University Symp. on Steel Research*, Fukuoka, Japan, June 6-9 (2012)
2. **Keunho Lee**, Jun-Ho Park, Yong-Min Kim, Kyung Il Kim, Dong-Ik Kim, Kyu Hwan Oh and Heung Nam Han; Observation of Texture evolution in AZ31 magnesium alloy during plane strain deformation and static recrystallization, *TMS 2013*, San Antonio, Texas, USA, March 3-7 (2013)
3. **Keunho Lee**, Seong-Jun Park, Yong Seok Choi, Se-Jong Kim, Tae-Ho Lee, Kyu Hwan Oh and Heung Nam Han; Dual-scale Correlation of Mechanical Behavior in Dual phase Low-density Steel, *The 8th GIFT-*

KIMS-SNU-Kyushu University Symp. on Steel Research, Pohang, Korea, June 20-22 (2013)

4. **Keunho Lee**, Hyun-Sik Choi, Kyung Il Kim, Kyu Hwan Oh and Heung Nam Han; Surface height variation due to microtexture development under plane strain deformation of AZ31 magnesium alloy, *International Conference on Textures of Materials*, Dresden, Germany, Aug. 24-29 (2014)
5. **Keunho Lee**, Seong-Jun Park, Jaeun Lee, Ji-Yeon Koh, Joonoh Moon, Dong-Ik Kim, and Heung Nam Han; Microstructure and mechanical behavior of austenite-based lightweight steel, *Gordon Research Conference- Physical Metallurgy*, Biddeford, Maine, USA, July 19-24 (2015)
6. **Keunho Lee**, Jaeun Lee, Seong-Jun Park, Joonoh Moon, and Heung Nam Han; Analysis of aging effect on microstructure and mechanical behavior in austenite-based lightweight steel, *IUMRS-ICAM 2015*, Jeju, Korea, Oct. 25-29 (2015)
7. **Keunho Lee**, Siwook Park, Sang Sub Han, Seong-Jun Park, Kyu Hwan Oh, Heung Nam Han; Investigation of orientation relationship and growth direction of beta-Mn phase in austenite-based lightweight steels using 3D microstructure, *The 3rd International Congress on 3D Materials Science 2016*, St. Charles, Illinois, USA, July 10-13 (2016)

References

Prof. Heung Nam Han (Thesis Supervisor)
Department of Materials Science & Engineering, College of Engineering,
Seoul National University, Seoul 151-741, Korea
(TEL: 82-2-880-9240, FAX: 82-2-885-9671, hnhan@snu.ac.kr)

Prof. Anthony D. Rollett (Advisor during visiting periods)
Department of Materials Science and Engineering, Carnegie Mellon
University,
5000 Forbes Avenue Pittsburgh, PA 15213-3890, USA
(TEL: 1-412-268-3177, FAX: 1-412-268-3113, rollett@andrew.cmu.edu)